Vera C. Rubin Observatory
Systems Engineering

An Interim Report on the ComCam On-Sky Campaign

On behalf of Rubin Observatory Project

SITCOMTN-149

Latest Revision: 2024-12-18

DRAFT

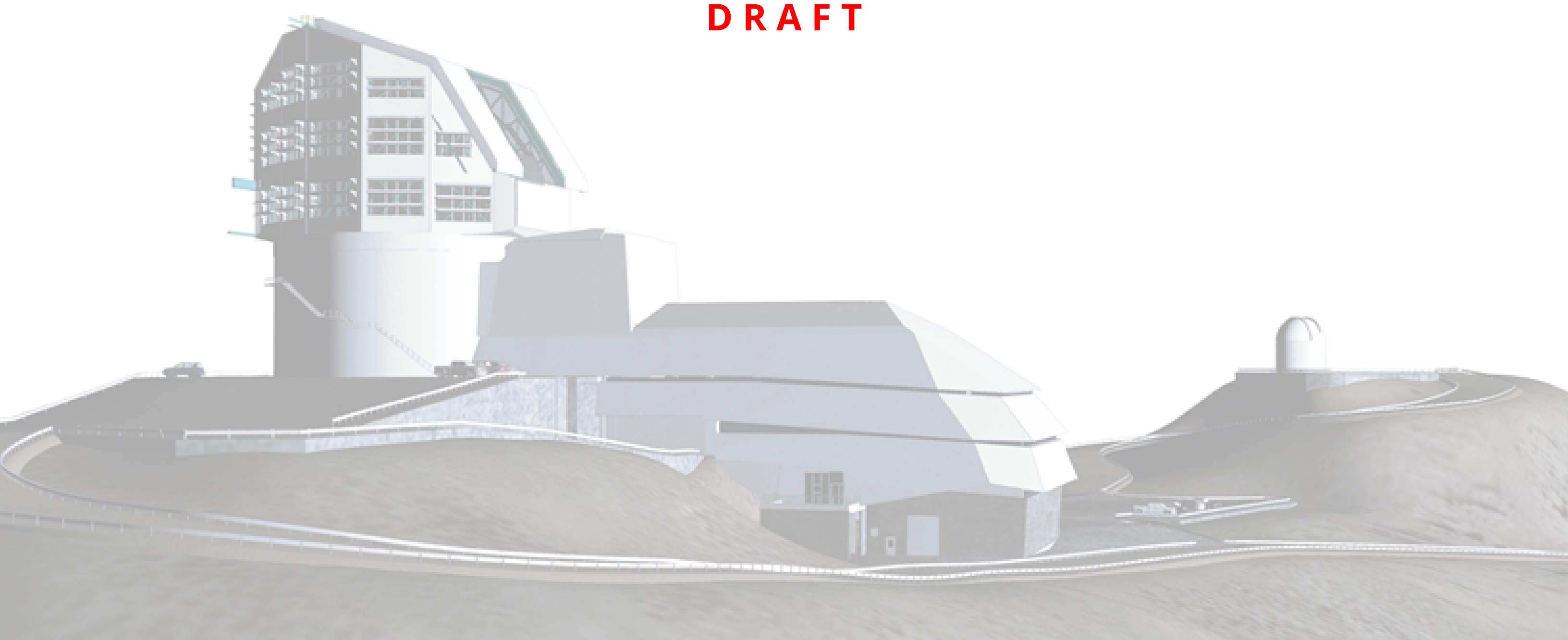

Abstract

A summary of what we have learned from the initial period of ComCam observing

Change Record

Version	Date	Description	Owner name
1	YYYY-MM-DD	Unreleased.	Robert Lupton

Document source location: `https://github.com/lsst-sitcom/sitcomtn-149`

Contents

An Interim Report on the ComCam On-Sky Campaign

1 Introduction

The Vera C. Rubin Observatory on-sky commissioning campaign using the Commissioning Camera (ComCam) began on 24 October 2024 and is forecasted to continue through mid-December 2024. This interim report provides a concise summary of our understanding of the integrated system performance based tests and analyses conducted during the first weeks of the ComCam on-sky campaign. The emphasis is distilling and communicating what we have learned about the system. The report is organized into sections to describe major activities during the campaign, as well as multiple aspects of the demonstrated system and science performance.

Warning: Preliminary Results

All of the results presented here are to be understood as work in progress using engineering data. It is expected at this stage, in the middle of on-sky commissioning, that much of the discussion will concern open questions, issues, and anomalies that are actively being worked by the team. Additional documentation will be provided as our understanding of the demonstrated performance of the as-built system progresses.

1.1 Charge

We identify the following high-level goals for the interim report:

- **Rehearse workflows for collaboratively developing documentation** to describe our current understanding of the integrated system performance, e.g., to support the development of planned Construction Papers and release documentation to support the Early Science Program [RTN-011]. This report represents an opportunity to collectively exercise the practical aspects of developing documentation in compliance with the policies and guidelines for information sharing during commissioning [SITCOMTN-076].
- **Synthesize the new knowledge** gained from the ComCam on-sky commissioning cam-

paign to inform the optimization of activities between the conclusion of the ComCam campaign and the start of the on-sky campaign with the LSST Camera (LSSTCam).

- **Inform the Rubin Science Community** on the progress of the on-sky commissioning campaign using ComCam.

Other planned systems engineering activities will specifically address system-level verification ([LSE-29] and [LSE-30]) using tests and analysis from the ComCam campaign. While the analyses in this report will likely overlap with the generation of verification artifacts for systems engineering, and system-level requirement specifications will serve as key performance benchmarks for interpreting the progress to date, formal acceptance testing is not an explicit goal of this report.

The groups within the Rubin Observatory project working on each of the activities and performance analyses are charged with contributing to the relevant sections of the report. The anticipated level of detail for the sections ranges from a paragraph up to a page or two of text, depending on the current state of understanding, with **quantitative performance** expressed as summary statistics, tables, and/or figures. The objective for this document is to **summarize the state of knowledge of the system**, rather than how we got there or "lessons learned". The sections refer to additional supporting documentation, e.g., analysis notebooks, other technotes with further detail, as needed. Given the timelines for commissioning various aspects of the system, it is natural that some sections will have more detail than others.

The anticipated milestones for developing this interim report are as follows:

- 18 Nov 2024: Define charge
- 4 Dec 2024: First drafts of report sections made available for internal review
- 11 Dec 2024: Revised drafts of report sections made available for internal review; editing for consistency and coherency throughout the report
- 18 Dec 2024: Initial version of report is released

Warning: On-sky Pixel Image Embargo

All pixel images and representations of pixel images of any size field of view, including individual visit images, coadd images, and difference images based on ComCam commissioning on-sky observations must be kept internal to the Rubin Observatory Project team, and in particular, cannot be included in this report. Embargoed pixel images can only be referenced as authenticated links. See [SITCOMTN-076] for details.

2 System Performance Analysis

Topics to convert into text

- M1M3 and M2 glass installed on the Simonyi Survey Telescope.
- Since then, we have been operating the telescope with limited velocity, acceleration, and jerk limits following the performances defined in TMA Motion Settings.
- For each configuration, defined in terms of a percentage of the maximum velocity, acceleration, and jerk, we ran multiple gateway tests.
- The gateway tests are described in the subsection 2.1 below.

2.1 Gateway Tests

We started the ComCam on Sky test campaign using Simonyi Telescope with limited performance, described as a percentage of the maximum velocity, acceleration, and jerk limits. The performance is defined in TMA Motion SettingsConcluence page.

Before we can increase the telescope performance, we need to perform a set of tests that ensure that the system will respond safely to the new velocity, acceleration, and jerk. These tests are called gateway tests. Here is the list of all the tests.

- BLOCK-T227 Dynamic Tests at El = 34° short and long slews

- BLOCK-T294 Dynamic Tests at El = 70° short and long slews
- BLOCK-T231 TMA Azimuth Brake Test
- BLOCK-T240 TMA Elevation Brake Distance
- BLOCK-T241 M2 closed-loop break-out brake test during TMA slew

2.1.1 Long and short slews at different elevations

These tests ensure that the force balance systems on M1M3 and on M2 can protect the mirrors on different telescope positions and while slewing. As we increase velocity, acceleration, and jerk limits, both mirrors suffer higher inertial forces and the force actuators must counteract them.

The last set of data was collected on 2024-11-28. The two figures below show the slews performed when collecting this data starting at higher elevations (70^o) and then moving to lower elevations (34^o).

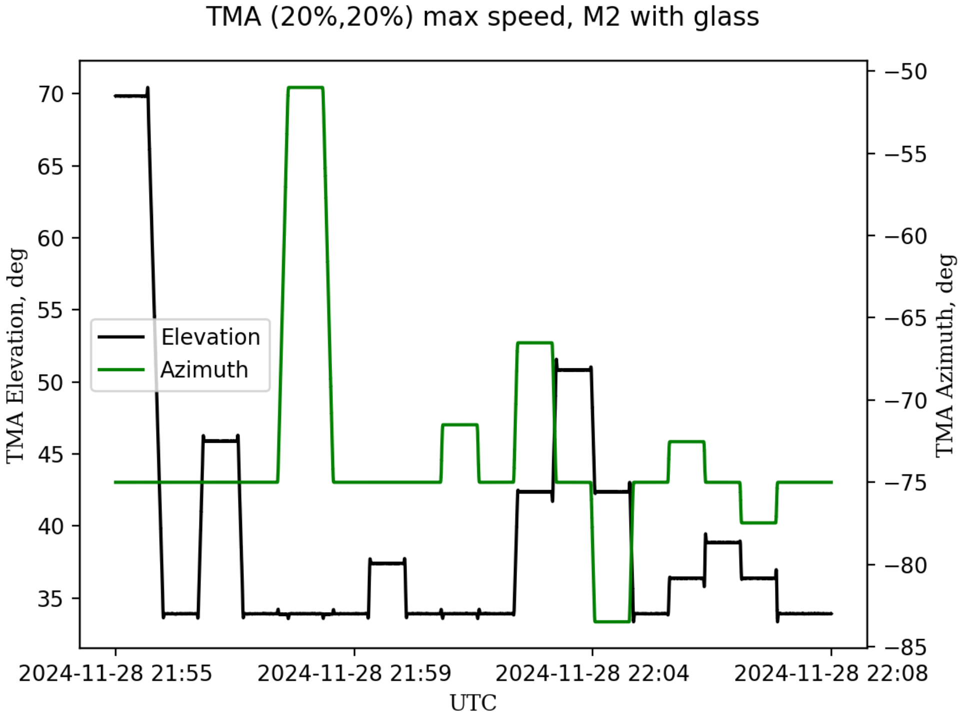

Figure 1: TMA Short and Long slews at El = 34^o.

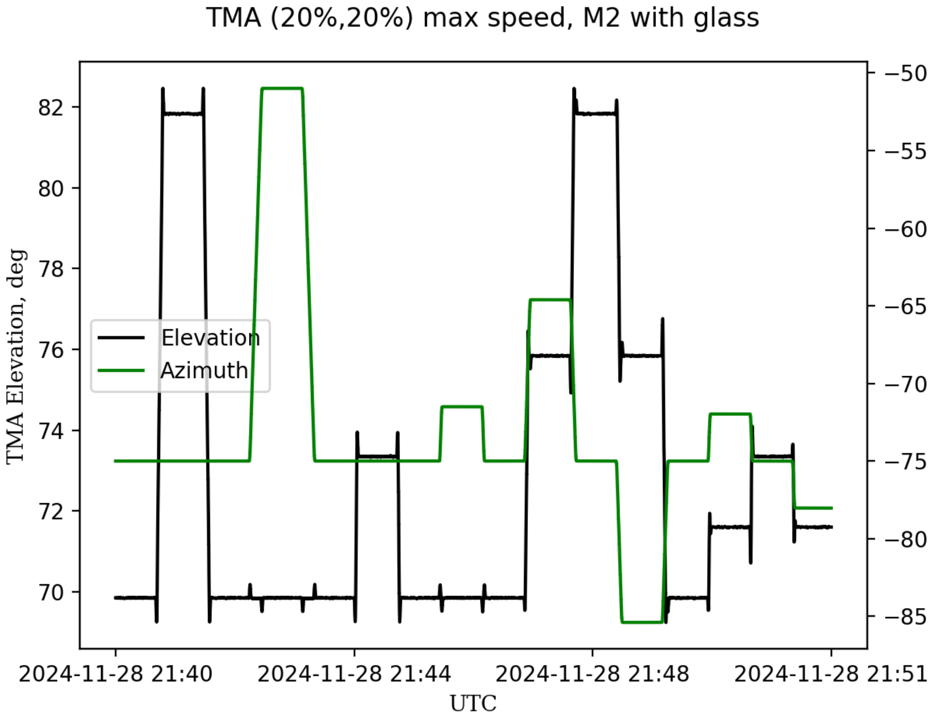

Figure 2: TMA Short and Long slews at El = 70^o.

For each of these slews, the force balance system on M1M3 should keep the forces measured on the hardpoints below an operational limit (15% of the breakaway limit, nominally 450 N). The figures below show histograms with the number of slews that hit certain minima and maxima values for the hardpoint forces. The left histogram shows the minima reached on each slew. The right histogram shows the maxima reached on each slew. The red dashed lines show the fatigue limit (30% of the breakaway limit, nominally 900 N).

You can see a few slews with min/max reaching 800 N at low elevations. This is quite close to fatigue limits (900 N). However, these slews were performed without booster valves enabled. In addition, the big majority of the slews have measured forces below the operational limit. This gave us confidence that, from M1M3's perpective, we can use the 20% velocity, acceleration, and jerk for the rest of the campaign. Note that we ran a few test slews with booster valves enabled and loads were significantly reduced (<200N per HP) before we got faults in some of the actuators with bad valves (need data analysis).

Similarly, M2 has limits of the measured forces associated with its closed loop and its open loop. The three figures below show the axial forces, the tangent forces, and the tangent force

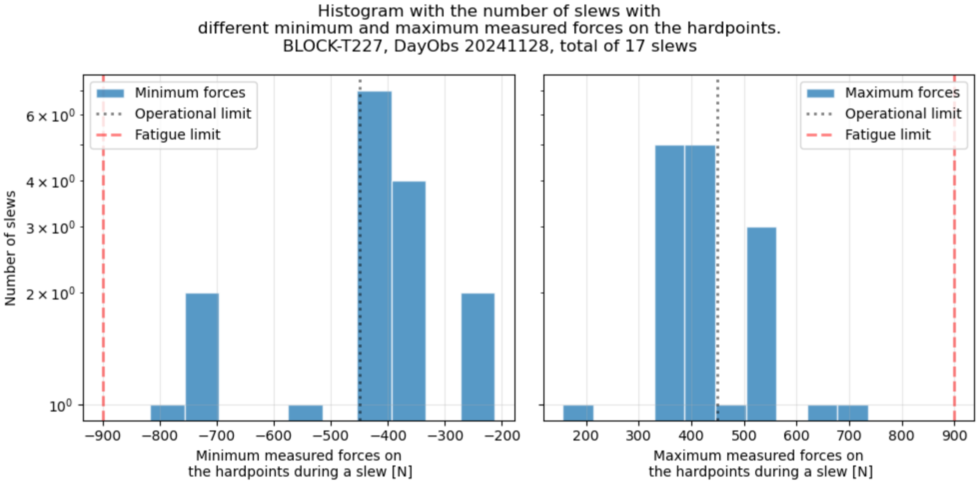

Figure 3: M1M3 hardpoint histograms min/max HP forces at low elevation.

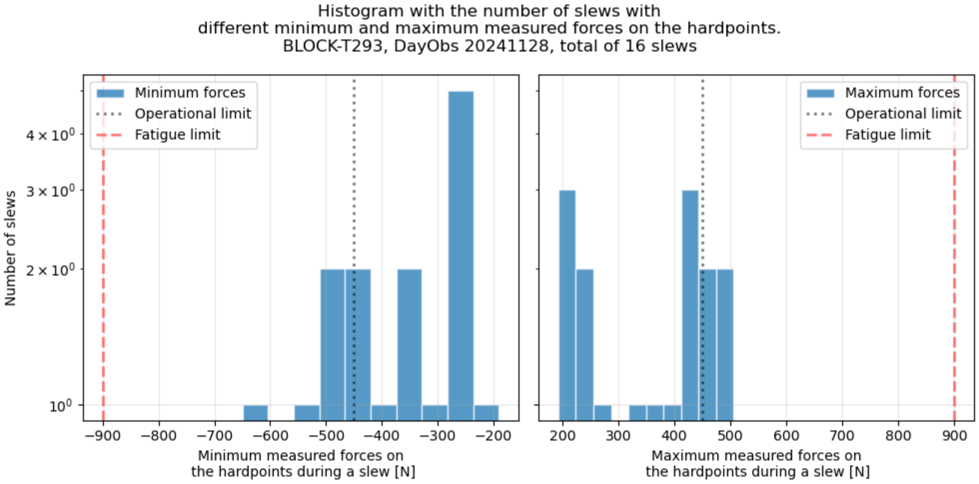

Figure 4: M1M3 hardpoint histograms min/max HP forces at high elevation.

errors for the slews performed at different elevations. We can see that, for every slew, all the forces are within the closed loop maximum forces limit. This means that, from M2's perpective, we are safe to operate the telescope with 20% velocity, acceleration, and jerk.

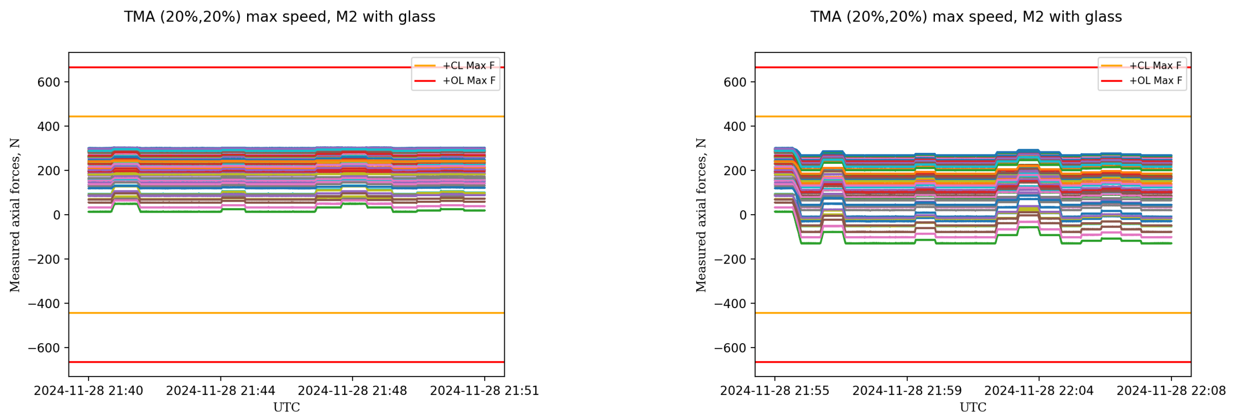

(a) M2 axial measured forces at low elevation.

(b) M2 axial measured forces at high elevation.

Figure 5: M2 axial measured forces during the slews at different elevations.

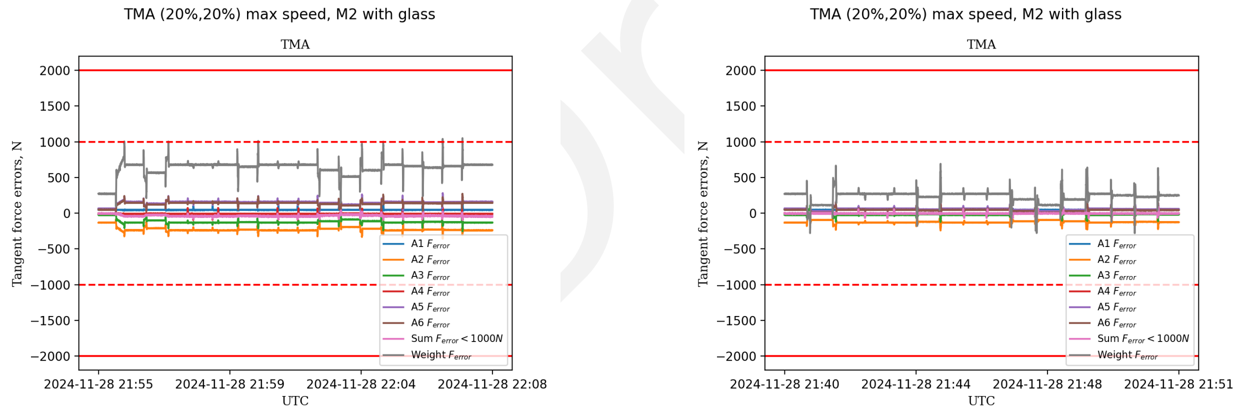

(a) M2 tangent force errors at low elevation.

(b) M2 tangent force errors at high elevation.

Figure 6: M2 tangent force errors during the slews at different elevations.

2.1.2 M2 close-loop breakout tests

BLOCK-T241 M2 closed-loop break-out brake test during TMA slew is a test that ensures that M2 can survive an event where the telescope is slewing and, for whatever reason, the closed-loop system is disabled. In this case, the telescope will go to a fault and stop.

The figures below show the axial forces, the tangencial forces, and the tangencial force errors during an event where the closed-loop system is disabled. The plots show that both axial and tangencial forces are within the limits. Considering this tests, we can say that M2 is safe to operate with 20% velocity, acceleration, and jerk.

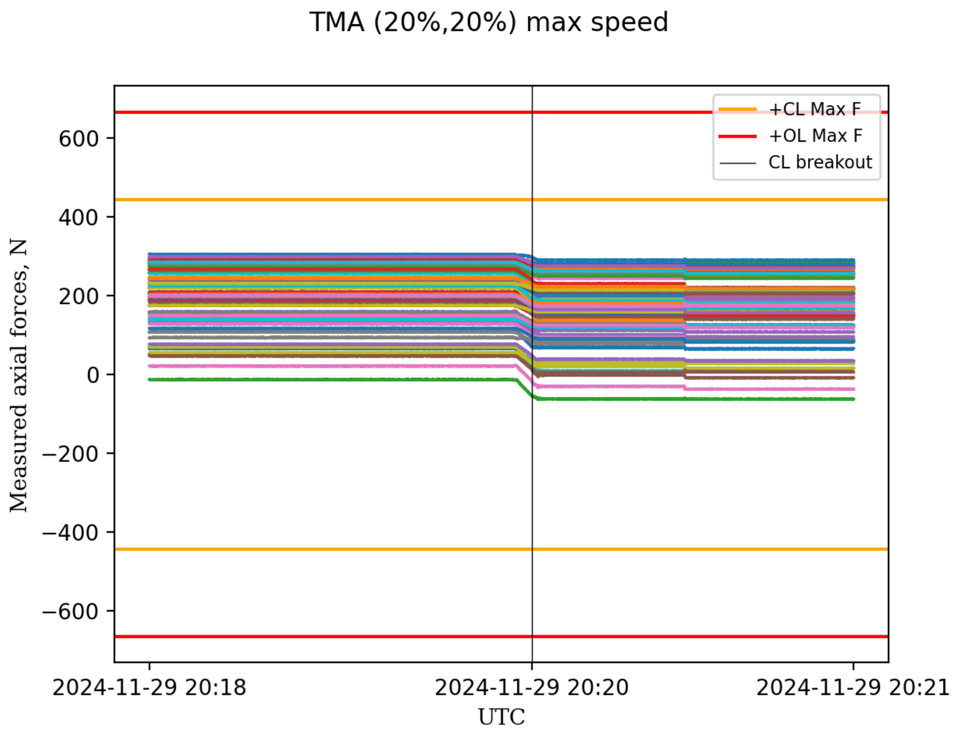

Figure 7: M2 axial measured forces during the closed-loop break-out test.

2.1.3 TMA azimuth and elevation brake tests

The tests BLOCK-T231 TMA Azimuth Brake Test and BLOCK-T240 TMA Elevation Brake Distance are designed to ensure that the telescope will stop in case of an emergency. Accordingly to the two figures below, the telescope travels 1.6 degrees in El (2.2 deg/s^2 peak deceleration) after the hard stop initiated. In Az, it travels 1.9 degrees (3.9 deg/s^2 peak deceleration) after hard stop initiated. Both without any mirror faults. These values seem reasonably low and confirm that the telescope would be safe in case of an emergency.

2.2 Night Performance

Statistical reports/summaries during the night?

- Measured m1m3 hardpoint histograms min/max HP forces.

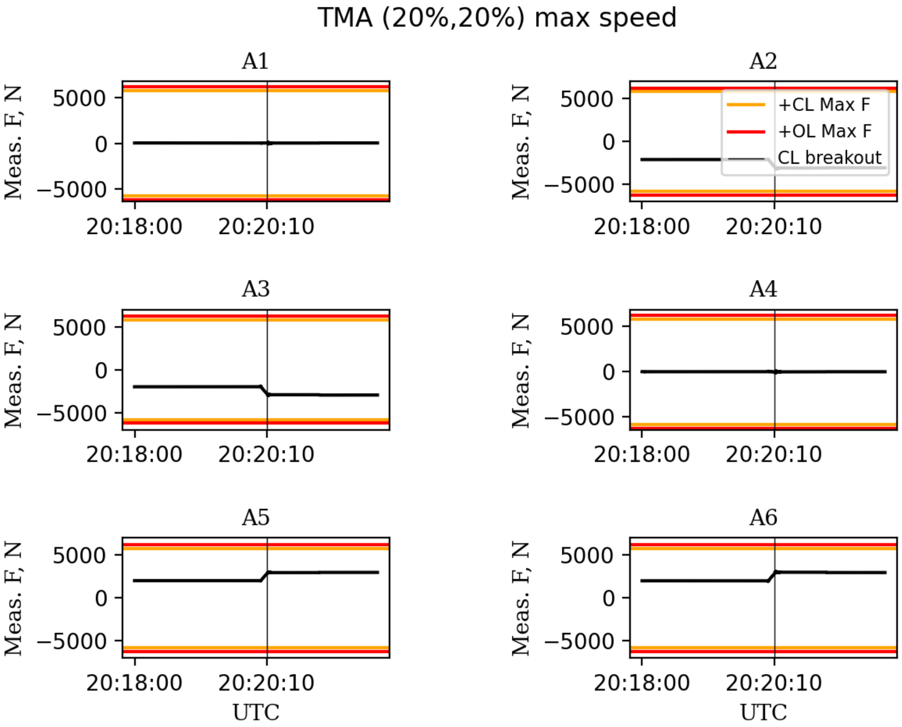

Figure 8: M2 tangencial measured forces during the closed-loop break-out test.

- FRACAS-158 / SITCOMTN-081 / SITCOM-1758 - Oscillations on HP forces and on azimuth torques

3 Active Optics System and Image Quality

3.1 Active Optics System Commissioning

The goals for commissioning of the AOS system with ComCam are to demonstrate that we can align the telescope optics, determine and correct for optical aberrations using the hexapods and bending modes for M2 and M1M3, and apply these corrections as a closed loop system. A stretch goal is to demonstrate that, for the limited field-of-view of ComCam, we can meet the image quality requirements of the LSST system (i.e., with the optical system delivering less than 0.4 arcseconds to the image quality budget) and do so consistently as a function of elevation and temperature. We have achieved many of these goals, but there are still significant challenges in delivering seeing limited images consistently as a function of variable observing conditions.

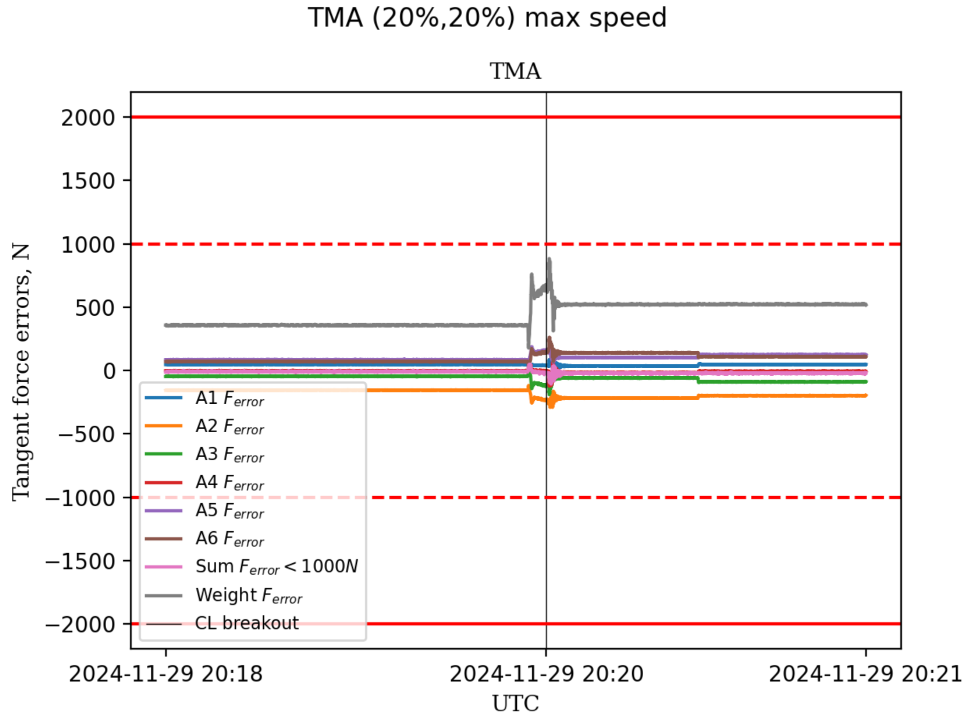

Figure 9: M2 tangencial force errors during the closed-loop break-out test.

AOS commissioning started on 2024-10-24 with the first ComCam images delivering a 1.7 arcsecond full-width half-maximum (FWHM) image quality. This is a testament to the exceptional metrology work of the engineering and optical teams during assembly and to the optimization of the Look-Up Table (LUT) for all the active optics components using the laser tracker data as well as mirror force balance data throughout 2024.

Sub-arcsecond image quality was achieved on the night of 2024-11-06, with a best image quality of 0.66 arcsecond FWHM (with a 0.1 arcsecond variation across the field achieved) on the night of 2024-11-12. Corrections for the optical aberrations have been achieved using two independent approaches; the TIE wavefront estimation algorithm, which is an inversion method, and the Danish wavefront estimation algorithm, which is a forward modeling method. The AOS system was able to achieve closed-loop corrections across varying elevations and stellar densities, with most optical modes utilized (excluding the three highest-order modes on M2). Closed-loop operations have been run autonomously by the observing specialists to show that the scripts and procedures are mature. Preparations are underway to prototype a fully autonomous survey-mode triplet-taking block before the conclusion of ComCam's on-sky operations.

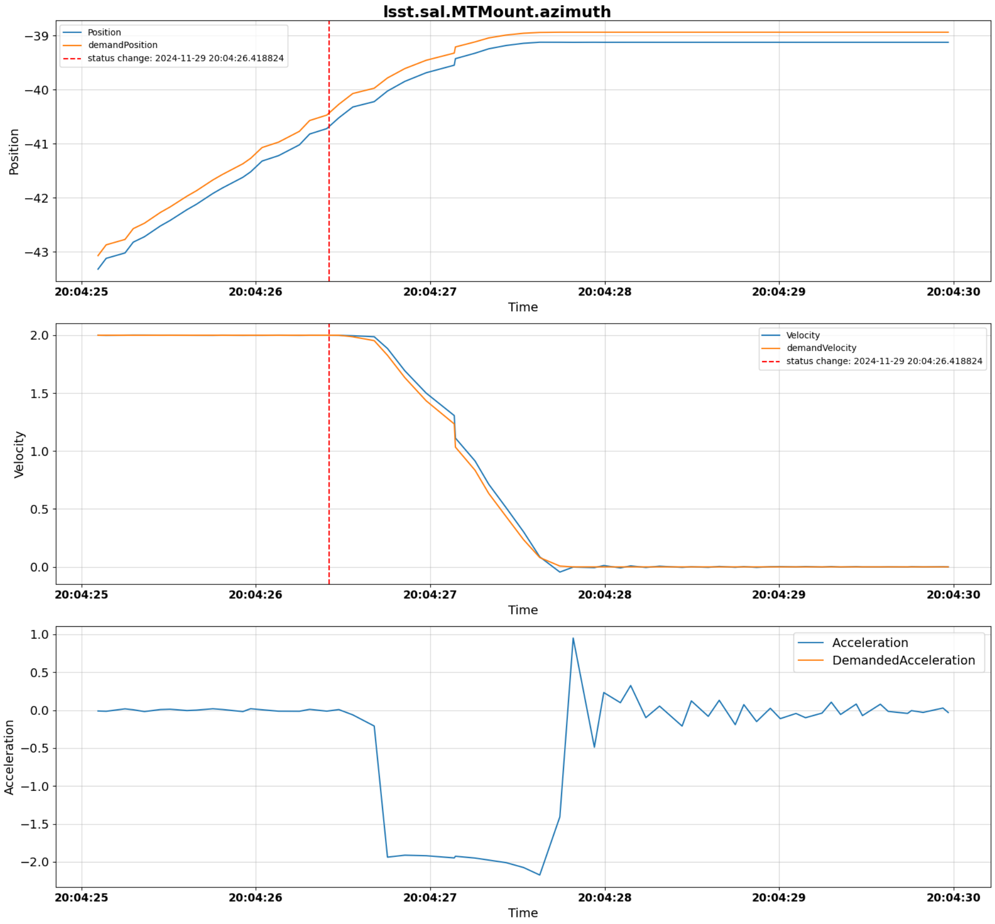

Figure 10: TMA Azimuth Brake Test.

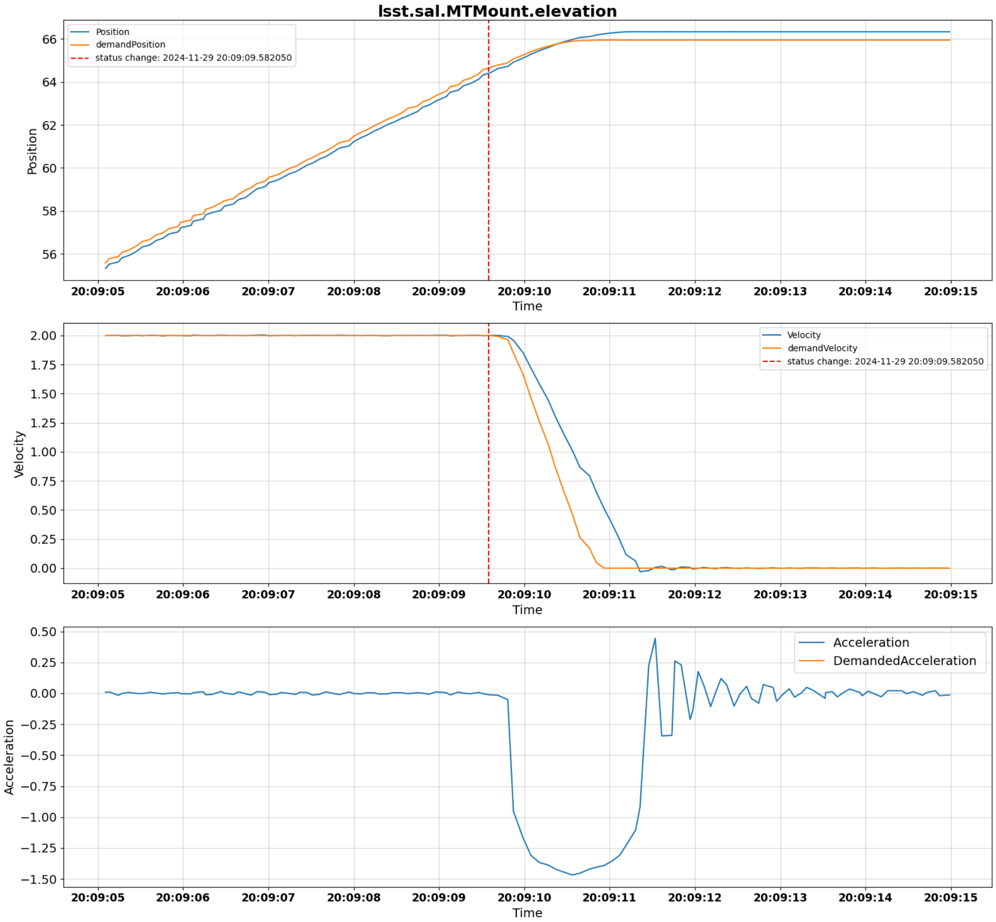

Figure 11: TMA Elevation Brake Distance.

While we have demonstrated that Rubin can achieve the optical performance requirements for the AOS system there are significant challenges in meeting the optical performance requirements consistently as a function of temperature and elevation. It is not currently clear which aspects of the optical system are limiting its performance but the AOS team is working to understand the source of high levels of defocus and some amount of astigmatism that are present in the Zernike measurements. The team is also working to improve the computational efficiency of the system, which currently takes 5 minutes to complete a closed-loop iteration.

After significant development, the AOS algorithms appear robust for a range of source densities and image qualities. A number of failure modes of the AOS software are present and being investigated. These include failures in processing images through Rapid Analysis when donuts cannot be detected on all sensors, and difficulty in measuring the wavefront when the images are significantly defocused (e.g., when the intra or extra focal images appear in focus). The AOS team is working to improve the robustness of the system to monitor these and other failure modes.

Figure 12 shows the FWHM delivered by the optical system (black line) as we correct the alignment and bending modes of the mirrors and camera over the nights 2024-11-25 to 2024-12-01. The FWHM is estimated from the Zernike amplitudes measured from out-of-focus donuts. The grey and blue lines are the 500nm and zenith corrected image qualities measured by SOAR and from the Rubin images respectively. The dashed green line is the 0.25 arcseconds image quality requirement for the telescope optics. From these measurements the AOS system is shown capable of meeting the image quality requirements. Delivering this consistently and without significant fine tuning is the current focus for the AOS team.

3.1.1 Initial Alignment

Initial alignment of the AOS utilizes an updated laser tracker nominal frame based on a Final Element Analysis Model. This ensures that the system is brought into focus prior to the start of observations. Combined with a measurement of the impact of gravity on the telescope, these refinements simplified the alignment process, demonstrating the value of accurate laser tracker data. Once we were able to get on-sky images using curvature wavefront sensing, we finalized the initial state of the hexapods position to ensure a well aligned system at the start of the night. Work is ongoing to understand the stability of the initial hexapod and bending mode positions across nights to determine how well we can predict the configuration of the

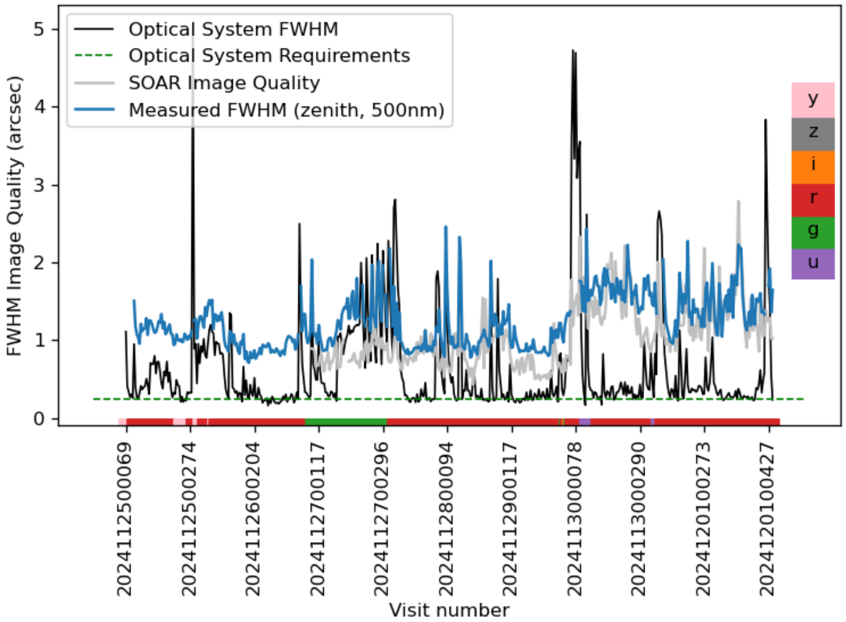

Figure 12: The FWHM delivered by Rubin (blue), the image quality from Rubin's optical system estimated from the AOS (black), and the image quality measured by SOAR (gray). The Rubin and SOAR measured FWHMs are corrected to 500nm and zenith.

AOS system at the start of each night.

3.1.2 Coordinate Systems

During the first few weeks, significant effort was devoted to understanding and refining coordinate systems at different steps of the Active optics closed-loop process (wavefront sensor estimation and correction calculation). We conducted the test by introducing one degree of freedom at a time and correcting for it. We identified a rotation discrepancy in ComCam's installation compared to the expected design, requiring adjustments in our alignment procedures. The coordinate discrepancies were resolved empirically in the early AOS tests. Based on these data the expected as-delivered coordinate system(s) for the mirrors, hexapods, and sensors will need to be derived from first principles and validated prior to AOS observations with LSSTCam.

3.1.3 Wavefront estimation

The wavefront estimator proved robust across diverse observing conditions of seeing, mount elevation and a few filters (r,i and y band) On dense fields such as 47 Tuc or NGC 253, the estimator provided accurate results for all sensors except the central one. Comparison of observed PSFs with simulations confirmed the accuracy of Rubin's ray-tracing software, `Batoid`.

Wavefront estimation and closed-loop convergence has been demonstrated using `TIE` and `Danish`. Other advancements include the implementation of sparse Zernikes, allowing selective inclusion of Zernike polynomial terms while minimizing cross-contamination of modes with identical azimuthal dependencies.

Despite delivering good optical quality, Zernike measurements indicate persistently high levels of defocus and some amount of astigmatism. We are continuing to investigate the source and impact of these measurements.

3.1.4 Closed Loop

Following resolution of initial issues with the AOS pipelines, closed-loop operations were achieved across varying elevations and filters (u, g, r, i, z, and y). Most optical modes were utilized, excluding the three highest-order modes on M2. Consistency in results across nights confirmed the need for further refinement of the LUT. In favorable seeing conditions, the system achieved sub-arcsecond image quality, with FWHM as low as 0.65 arcseconds. Autonomous closed-loop operations were run by observers, demonstrating the maturity of the system.

The closed loop process still takes 5min often requiring 5 or more iterations. The best performance for the closed loop achieved convergence in two iterations but delivering this consistently has not been achieved and tuning the closed-loop gain and making further adjustments to improve computational efficiency remains a priority for the team.

3.1.5 LUT

The LUT underwent initial validation across elevations, azimuths, and rotator angles, leading to incremental improvements. While these updates enhanced performance, further refinements are needed to address second-order dependencies. Insights from ComCam data will inform these efforts, ensuring readiness for LSSTCam, which may present distinct challenges due to its larger focal plane and optical system.

3.1.6 Lessons Learned and Next Steps

Lessons Learned - Coordinate Systems: Precision and methodical testing of coordinate systems are essential. Starting with foundational tests and incrementally increasing complexity ensures reliability. - Observer Training: Comprehensive documentation, including a subsystem overview and closed-loop procedures, significantly enhances observer support capabilities. - Closed-Loop Performance: Iterative testing and tuning of the closed-loop system are essential for delivering a consistently high image quality as a function of temperature, elevation, and other observing conditions. Achieving this performance consistently and without significant fine tuning will be a significant challenge. - Engagement and Morale: Fun and engaging night summaries boost team morale, fostering a collaborative and motivated work environment. - Transferability: Some ComCam lessons learned, particularly LUT and coordinate system adjustments, will not fully transfer to LSSTCam, requiring repeated validation.

Next Steps - Conduct step-by-step closed-loop validations for LSSTCam, validating signs and rotations for intentional perturbations. - Collaborate with the Camera Team to anticipate and mitigate known camera tilts. - Implement and validate tests tailored to LSSTCam's larger focal plane dimensions. - Prepare RubinTV and donutViz for full-array LSSTCam mode and automate its execution for all triplet-taking sequences. - Adapt MTAOS to run as a continuous background task, supporting survey-mode operations. - Optimize the AOS pipeline for speed, including binning and ISR performance improvements.

3.2 Image Quality

The AOS team has delivered very impressive image quality, showing images with 0.68 arcsec FWHM. If we assume that sources of image degradation add in quadrature and we trust our estimates of atmospheric seeing, this is consistent with reaching the image quality error budget allocation of our full system of 0.400 arcsec.

We are in the process of quantifying the different sources of image degradation. The main ones we're focused on measuring are degradation due to the camera/instrument, static optics, dynamic optics, mount motion, and observatory seeing.

3.2.1 Atmospheric Seeing

We do not currently have a working Rubin DIMM, although there repairs are in progress. In the meantime, we have a livestream of data from the SOAR RINGS instrument, which is a next-generation DIMM developed by Andrei Tokovinin and Edison Bustos. We are working on getting direct access to current and historical data for RINGS as well as the Gemini DIMM. This access will make it much easier to quantify the different sources of image degradation.

3.2.2 Static Optics

See Section 3.1 for more details on the performance of the static optics system.

3.2.3 Instrument

We are taking the measured LSSTCam instrument image degradation to be the same as for ComCam, so we will use budget table developed at SLAC.

3.2.4 Dynamic Optics

Dynamic optics contributions are caused by oscillations or motion of the mirrors, causing focus to shift during an exposure. We have accelerometers in the mirror cell and on the top end but have not yet analyzed the data.

3.2.5 Observatory Seeing

The two main contributors to observatory seeing are dome seeing and mirror seeing. We do not have a direct dome seeing monitor but we do have a 3D sonic anemometer located in the dome that is taking data. Larom Segev has looked at the correlation between the standard deviation of the sonic temperature, which should be a proxy for dome seeing due to thermal turbulence, and measured PSF FWHM in the science images (see Fig. 13). There may be some correlation, but we need more and better data, and to remove atmospheric seeing contributions.

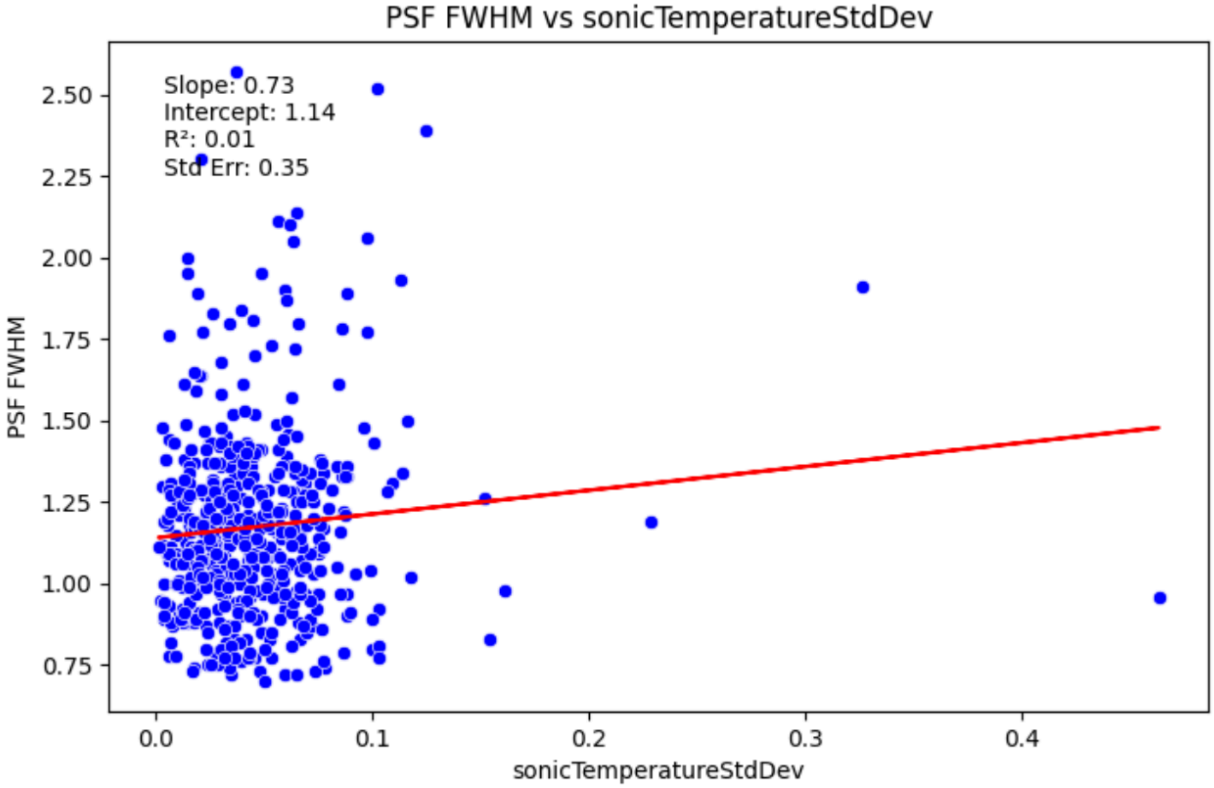

Figure 13: PSF FWHM versus the standard deviation of sonic temperature.

3.2.6 Mount Motion

There are two main components to image degradation due to mount motion. The first component comes from drift due to tracking errors. As we have not yet completed a full pointing model at all azimuths and elevations, we have not quantified this component yet. The second component of mount motion image degradation is due to tracking jitter. We quantify this by computing the rms deviation of the mount position as measured by the encoders from the position sent by MTPtg. Craig Lage computed the tracking jitter for all ComCam exposures through the 20th of November. From a total of 5311 images, the median image quality impact is 0.004 arcseconds, and 0.38% of images have an impact to image quality of above 0.05 arcseconds (see Figs. 14, 15, 16). This is well below the budgeted mount jitter error of 0.069 arcsec.

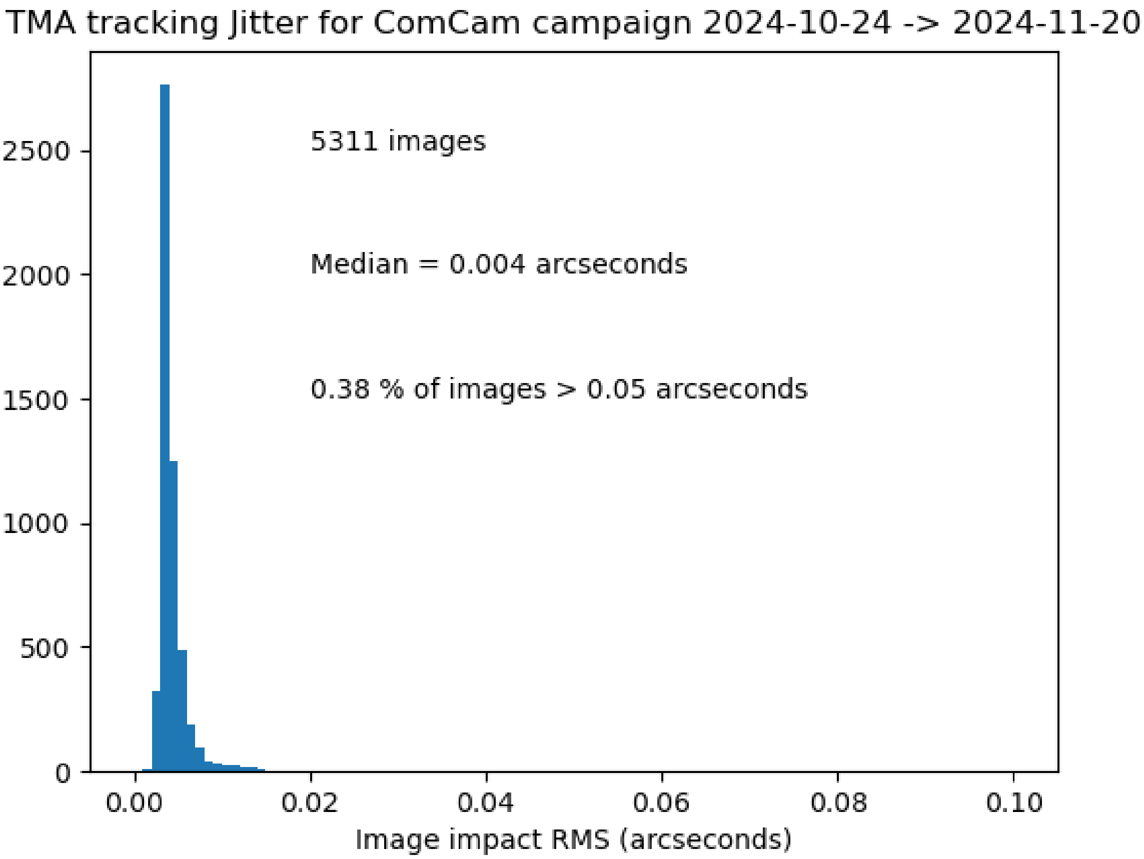

Figure 14: Total TMA tracking jitter for all exposures from October 24 to November 20.

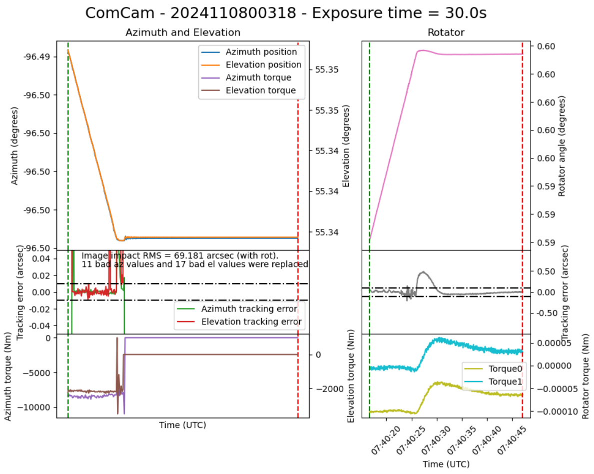

Figure 15: Exposure with an unusually large amount of mount motion image degradation.

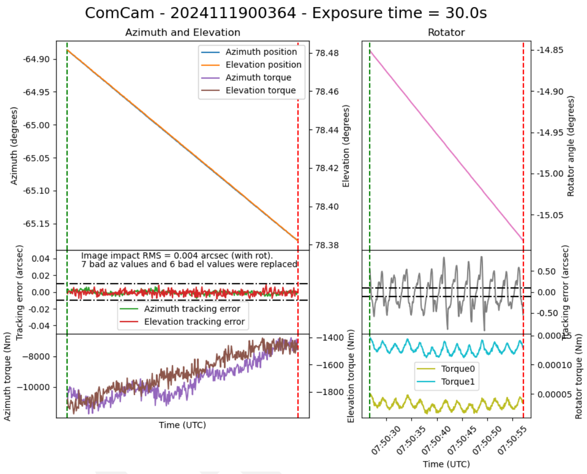

Figure 16: Exposure with a typical amount of mount jitter.

Filter	Number of Visits	Mean PSF FWHM	STD PSF FWHM
All	775	1.12	0.23
u	28	1.49	0.08
g	86	1.07	0.14
r	307	1.18	0.22
i	203	1.09	0.24
z	85	1.01	0.21
y	66	1.04	0.18

Table 1: Summary of PSF FWHM statistics. Data are from DRP from 2024-11-01 to 2024-11-28.

3.3 Delivered Image Quality and PSF

Image quality and PSF modeling are closely tied to the progress of the AOS system, and here is what can be concluded halfway through the data gathering with ComCam.

3.3.1 On Image Quality

The best image quality achieved so far is 0.7 arcsec, with a median of 1.1 arcsec during science visits. As shown in Table 1 and Figure 17, the PSF FWHM as a function of observation dates highlights the progress. It is important to note that all these data were collected during the AOS testing and validation phase. This makes the achieved image quality even more encouraging, demonstrating significant progress.

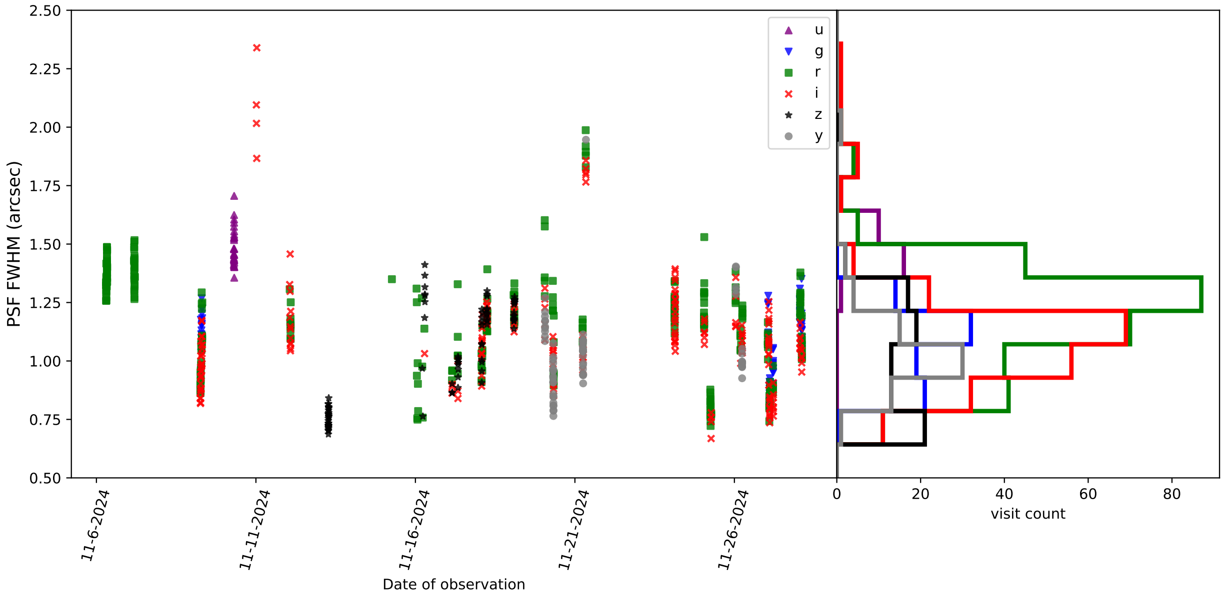

Figure 17: PSF FWHM as a function of the observed date. Data are from DRP from 2024-11-01 to 2024-11-28.

3.3.2 PSF Modeling

Two different PSF models are currently used in the DM pipeline: PSFEx, which provides a fast preliminary PSF estimation, and Piff, used later in the pipeline for more accurate PSF modeling. During the initial data collection with ComCam and AOS testing, most in-focus star shapes exhibited doughnut-like patterns, reflecting residual optical aberrations that had not yet been corrected. This specific form of asymmetry posed challenges for PSF modeling and was not typical. Interestingly, Piff, despite being the more advanced model, struggled to handle the large, non-symmetric PSFs compared to PSFEx. Fig. 18 shows how we were able early in the observation to constrain the PSF.

However, as the AOS system improved image quality and produced more symmetric PSFs, we observed behavior more consistent with expectations for both PSFEx and Piff. Analysis of second-moment reconstructions shows that PSFEx has a systematic offset in size reconstruction compared to Piff, which aligns with observations from DES. Overall, Piff demonstrates better PSF reconstruction, as illustrated in Fig. 19.

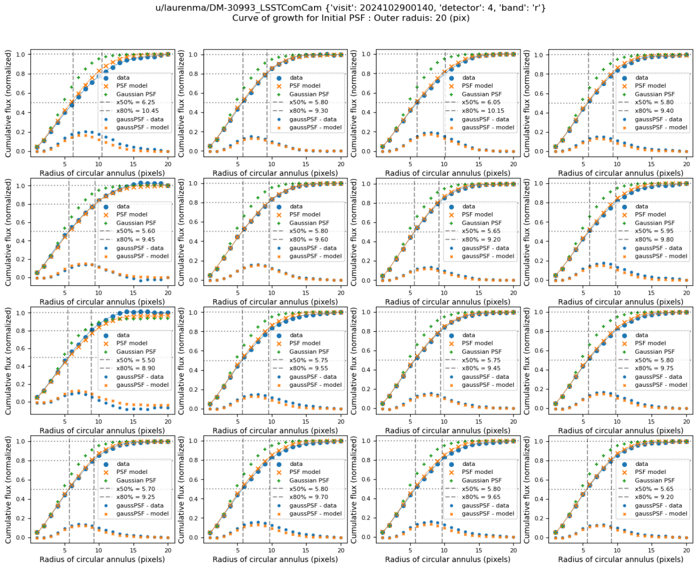

Figure 18: Growth curves of the PSF compared to its model (PSFex here) in the early data taken with ComCam.

3.3.3 Understanding PSF Physics

With LSSTCam, we aim to leverage wavefront sensor data to estimate the optical system's current state and model the optical contribution to the PSF, ultimately building a physical PSF model. During AOS testing with ComCam, the optical state was estimated using out-of-focus images to predict the optical contribution to PSF shape. A ray-tracing analysis showed that the optics fitted from these images could predict the PSF shape, providing strong evidence that a physical PSF model could be developed for LSSTCam (See Fig. 20)

4 Image Inspection

The prospects for human-based inspection of the vast number of images to be produced by the Rubin/LSST are unavoidably going to be limited to a fraction of the dataset produced (even nightly, let alone for the full 10-year survey). Yet, the potential value of getting human eyes on the images (including the raw, minimally processed, and final processed and calibrated stages), is immense, in particular for identifying patterns that are easily spotted by eye, yet tend to evade most modern automated image quality assessment protocols.

Every dataset from any given observation program comes with its own unique set of "fea-

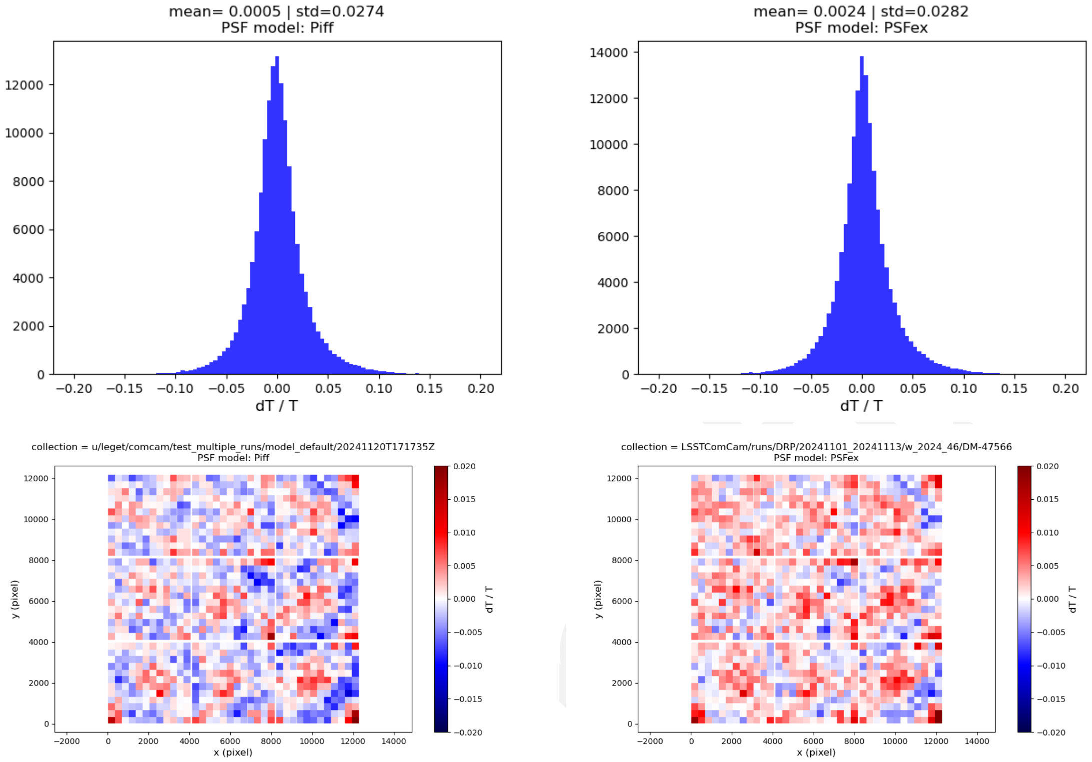

Figure 19: Size residuals for Piff and PSFex (1d distribution and 2d average across visits). Piff has no offset and smaller scatter. Both panels exhibit spatial structure across the focal plane, based on spatial averages across all science visits. The PSF is modeled per CCD in pixel coordinates using a second-order polynomial for interpolation. The observed structure is unlikely to result from atmospheric or dome effects, given that this plot represents an average across visits. Instead, it likely reflects spatial variations not captured by the second-order polynomial interpolation, such as optical aberrations or sensor anomalies.

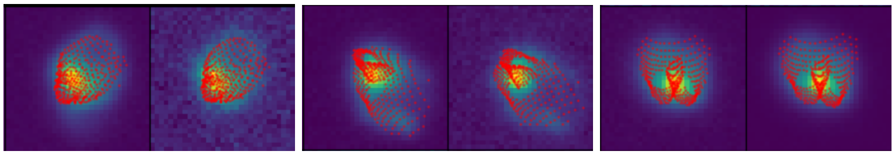

Figure 20: In-focus stars and prediction from the ray tracing on predicting PSF shape (red-dot). Optics parameters on the ray tracing side were derived from out of focus images by measuring optical aberration on ”donuts” (out of focus star).

tures” stemming from the observatory structures, optics, camera, detectors, electronics, observation strategy, the night sky, calibration products, etc. This makes eyeball inspection particularly valuable in the early days of commissioning. Fortuitously, the energy and enthusiasm of internal project members are at extrememly high levels at this stage, so there is no shortage of voluntary effort for human visial inpsection for the commissioning phase of the ComCam. This effort to date has largely proceded via an informal see-something-say-something scheme, with many users posting their latest findings on the internal staff Slack channels (namely the #sciunit-image-inspection channel, but also prominently in other channels, #sciunit-lsb, #validation-team, #embargo-beautiful-images, #ops-satellites, #dm-calibraion-products to name a few).

Anomolies and peculiarities reported to date along with details of and/or pointers to further study and explanation (where applicable) include:

- **ghosts**: most prominent around bright stars (including those falling outside of the FOV) and attributed to multi-bounce reflections off of the focal plane and the ComCam optics. Qualitatively, the presence and appearance of the ghosts are well predicted by Josh Meyers’ “batoid ray tracer”, even in its current unoptimized state. It is noted that the nature of the ghosts will be quite different for the full LSSTCam, but this initial level of understanding of this feature is promising and useful for honing characterization and mitigation strategies.
- **stray/scattered light**: prominent ring-shaped waffle/corduroy-like features seen early on were identified as originating from a blinking light on a crane that was left on. Large irregular ring-shaped “spots” were attributed to the laser tracker (an issue in access to turn it off was noted). ComCam is known to be less well baffled than LSSTCam, so scattered light from off-axis light sources is expected to be worse.
- **satellite streaks**: see Section 9.1
- **kettlebell & trefoil-shaped PSFs**: see Section 3.1. This issue was further investigated in the context of the PSF modelling itself on such irregularly shaped PSFs. It was noted that the preferred “piff” algorigthm (which is used for the final characterization model) was performing worse that the “psfex” algorithm (which, due to its relative speed, is used in the initial characterization). As such, we temporarily switched to using only “psfex” until the image quality was improved. Given the incredible and expeditious work of the AOS team, we are already confident that we can switch back to our preferred configurartion.

(This has also spurred a study into the reason why “piff” seems to struggle with these shapes and will hopefully lead to improvements there, see Section 3.3).

- **background subtraction issues**: see Section 8
- **repeated patchwork gradients**: a small number of images appear to have a bias gradient that appears in several amplifiers of detector 1 (R00_S01). This feature is currently under investigation, but it appears to be most prominent when a bright star resides close to the amplifier (right) edge of this detector. The bias shift appears in the prescan, active area, and overscan regions of the affected amplifiers. It seems likely that this is some type of crosstalk, but the origin and manifestation is unclear. It remains to be seen whether similar features are seen in any other detectors. It is likely that this feature will be further studied in the context of Section 5.2.
- **trailed sources**: due to tracking errors. These are particularly difficult to identify with automated image quality metrics (there are some ideas about using AI to identify tracking error-based image degradation floating around, but we also hope to be able to confidently rely on data from the EDF to indicate tracking issues).

Future Endeavors

A major goal for future image inspction efforts is to develop a more systematic way to identify and report issues and, where possible, alert the relevant stakeholders for further investigations into mitigating problems.

There has been some effort to deploy the “Exposure Checker” that was developed for the Dark Energy Survey (Melchior et al., 2016)[1] and has been previously deployed by LSST DESC for the visual inspection of simulated DC2 data (LSST Dark Energy Science Collaboration (LSST DESC) et al., 2021).

Also recently implemented for visual inspection is a rendering of the 3-color coadd HIPS maps produced regularly during the nightly validation and DRP processing runs. Such images are invaluable for highlighting myriad issues at the coadd level (often indicating a need to drill-down to the visit-level for a full diagnosis, while providing significant clues on where to look first).

---

[1] See demo `https://des-exp-checker.pmelchior.net/`

5 Calibration Data and ISR

5.1 Calibration Data

5.1.1 Twilight Flats

Because the flat field screen and illuminator is not expected to be operational while ComCam is on the telescope, we used dithered, tracked twilight flats to generate the combined flat calibration frames. The exposure time of the twilight flats were dynamically adjusted to hit a target count, generally in the range of 10-20k. The flats taken at a wide range of azimuth angles and rotator angles. See Fig. 21 for the counts per pixel per second as a function of sun elevation angle.

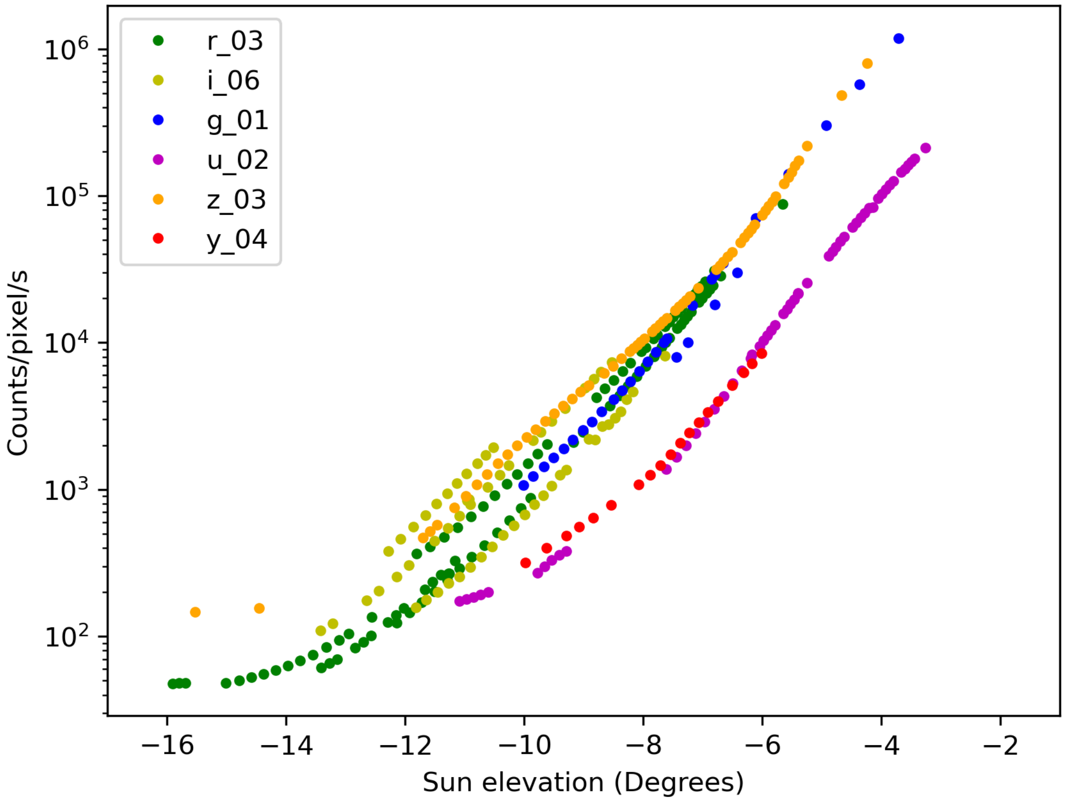

Figure 21: Twilight flat counts per pixel per second for each filter as a function of sun elevation angle.

5.2 Instrument Signature Removal

The quality of the instrument signal removal (ISR) has improved during commissioning, as we create and deploy updated calibration products that better represent the ComCam system. The following discussion summarizes our current understanding of a variety of features, both expected and newly seen on ComCam, and presents our expected prognosis of the behavior of the full LSSTCam.

5.2.1 Phosphorescence

There are regions on some of the detectors (most visible in R22_S01, detector=1) which show bright emission, particularly at bluer wavelengths, as shown in Figure 22. This is believed to be caused by a thin layer of remnant photo-resist from the manufacturing process that remained on the detector surface, and is now permanent due to the subsequent addition of the anti-reflective coating. In addition to the large areas, there are also discrete point-source-like or cosmic-ray-like defects caused by accumulations of this material. Adding to the difficulty of mitigating these defects is that this photo-resist is known to be phosphorescent, explaining why these regions are more noticeable in the bluer filters.

The initial studies of this show that these features can continue to emit light up to several minutes after they've been illuminated. Due to the long duration of these features, we decided to place manual defect masks over the worst regions. The first of these manual masks takes up about 3.5% of that detector, smaller than but consistent with estimates that this would create a pixel loss of approximately one amplifier.

The ITL detectors in LSSTCam are believed to have been cleaned better, so this should be less of an issue on the full camera.

5.2.2 Vampire pixels

There are defects on ComCam that have been classified as "vampire" pixels, as they appear as a bright defect with a (generally) axisymmetric region surrounding the bright core, as if the defect is draining charge from its neighbors. The naming is at least broadly correct, as integrating to large radii shows that these regions do appear to conserve charge. There is an intensity dependence that makes these vampire pixels different than standard hot pixels, as

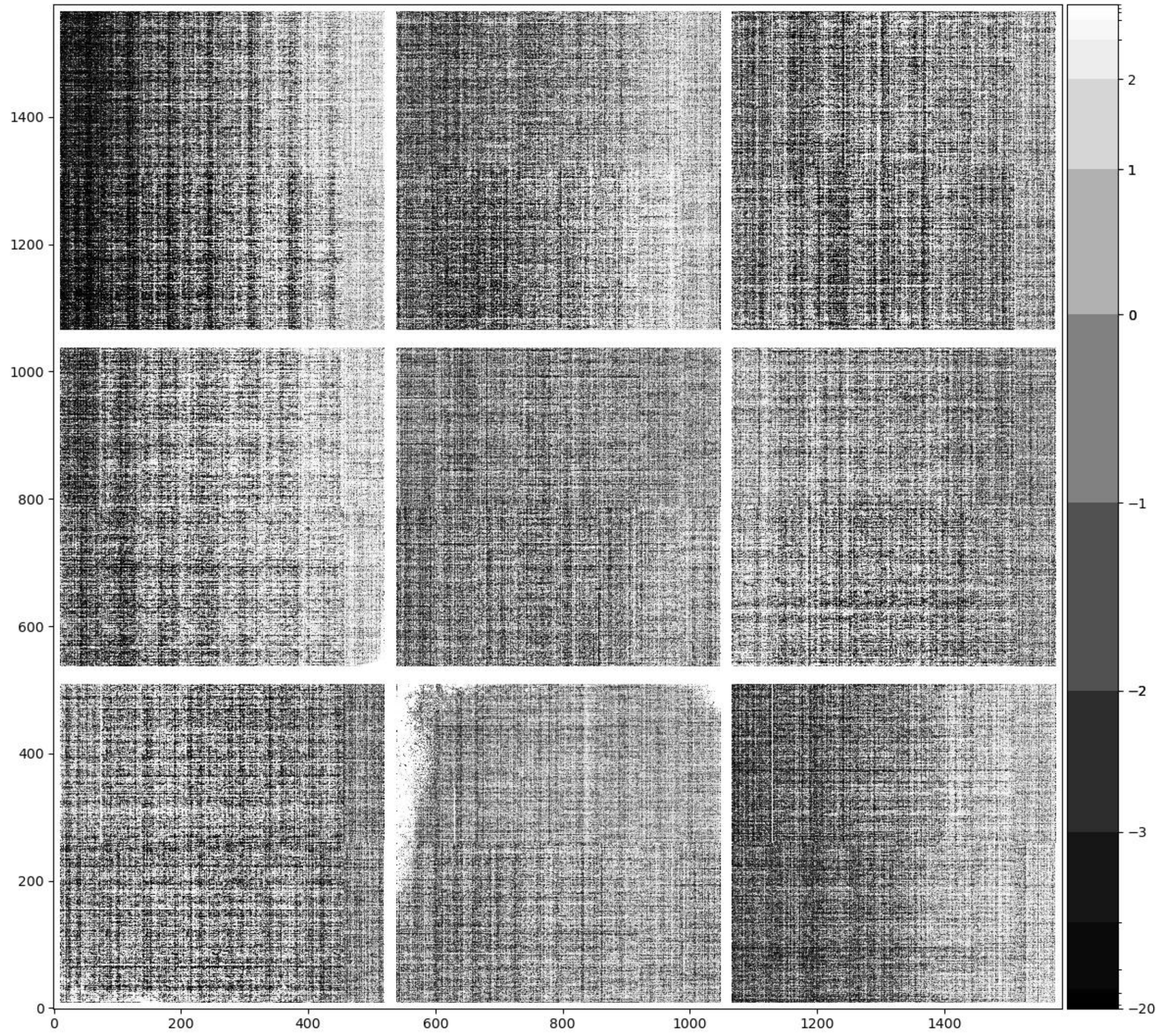

Figure 22: The phosphorescence seen in R22_S01, shown here in a dark exposure taken after a series of twilight flats (exposure=2024112000065). This material absorbs light at bluer wavelengths and re-emits that energy over a wide range of wavelengths.

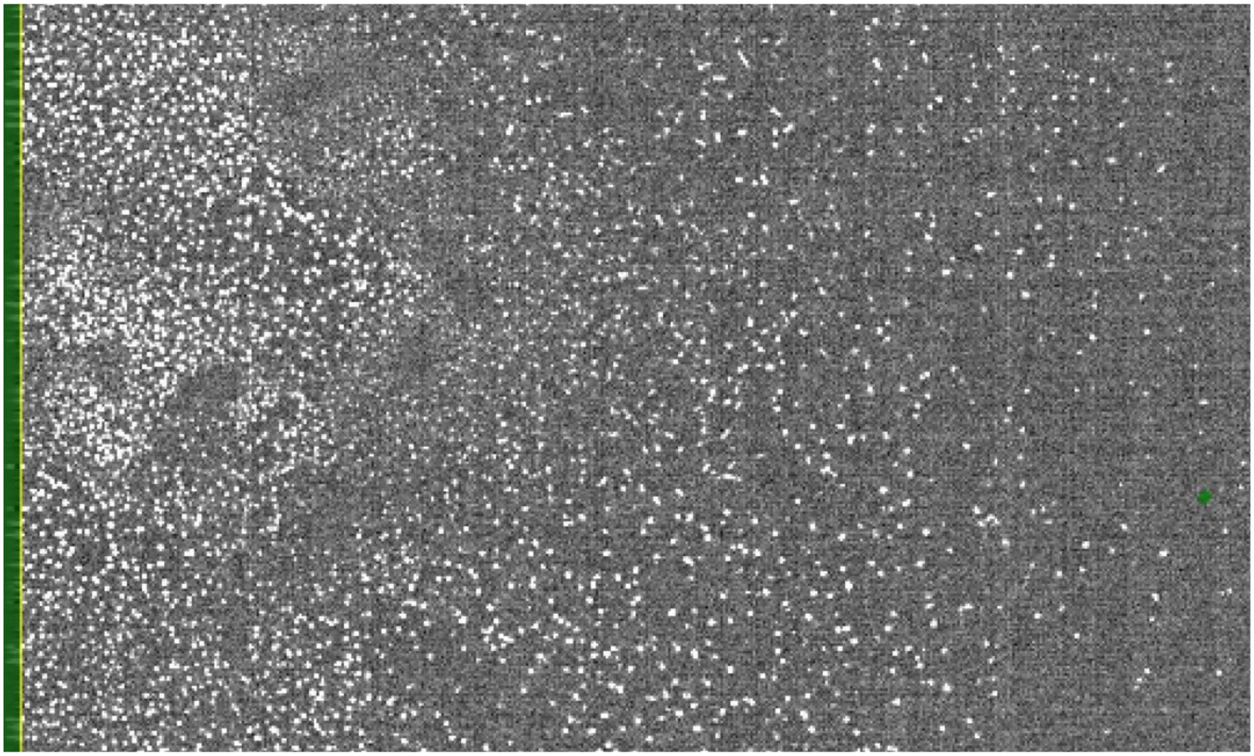

Figure 23: A full-resolution view of the edge of R22_S01. The features shown in this image are point-like sources caused by the trapped phosphorescence photo-resist.

these pixels do not show up on dark frames, only on flats and science exposures, where the detector surface is illuminated. After the initial discovery of the bright obvious vampires, we added new masking code that identifies the bright cores that are above 2.0 on the combined flat (pixels that are greater than 200% of the median flat level), and adds circular masks to the defect list. This appears to find the most problematic examples, but as we have improved flat quality during commissioning, we are finding that there is a sub-population that are not as severe, but likely have a similar physical mechanism. This population is still bright on the flat, with peaks around 1.2 (20% elevated relative to the flat), and may need to be masked as well. From an initial study in the lab, it appears that all ITL detectors on LSSTCam have a few of these kinds of defects, with two detectors approaching similar contamination levels as R22_S10 on ComCam.

5.2.3 Saturated star effects

Although we expected to find saturated star trails coming from bright sources, the observed behavior of these trails is unique. Saturation spikes on most cameras appear as streaks extending from the core of the bright source along the direction of the parallel transfers, and truncate as the charge bleeds run out of charge (and can no longer overcome the potentials defining the pixel) (See Figure 26). The trails seem with ComCam, however, extend the entire height of the detectors, crossing the midline break (as is to be expected in the ITL, but not the E2V, CCDs). These trails are also not at the expected high state, with the centers of these trails having flux levels lower than the average sky levels, creating dark trails. On the worst saturated objects, there is also evidence of charge pile-up near the serial readout, which can then create fan-like bright features at the edge of the detector. Those bright features can also then crosstalk onto other amplifiers.

The underlying physics is not well understood, and further study will be needed to see if we can correct these trails outside of the regions of charge buildup. Until we have a correction, we plan to begin masking both the trail and the fan-spread near the serial register.

Although we haven't seen identical features on LATISS, the presence of these odd trails on all ComCam detectors suggests that this is a property of the ITL devices, and so will likely be seen on LSSTCam as well.

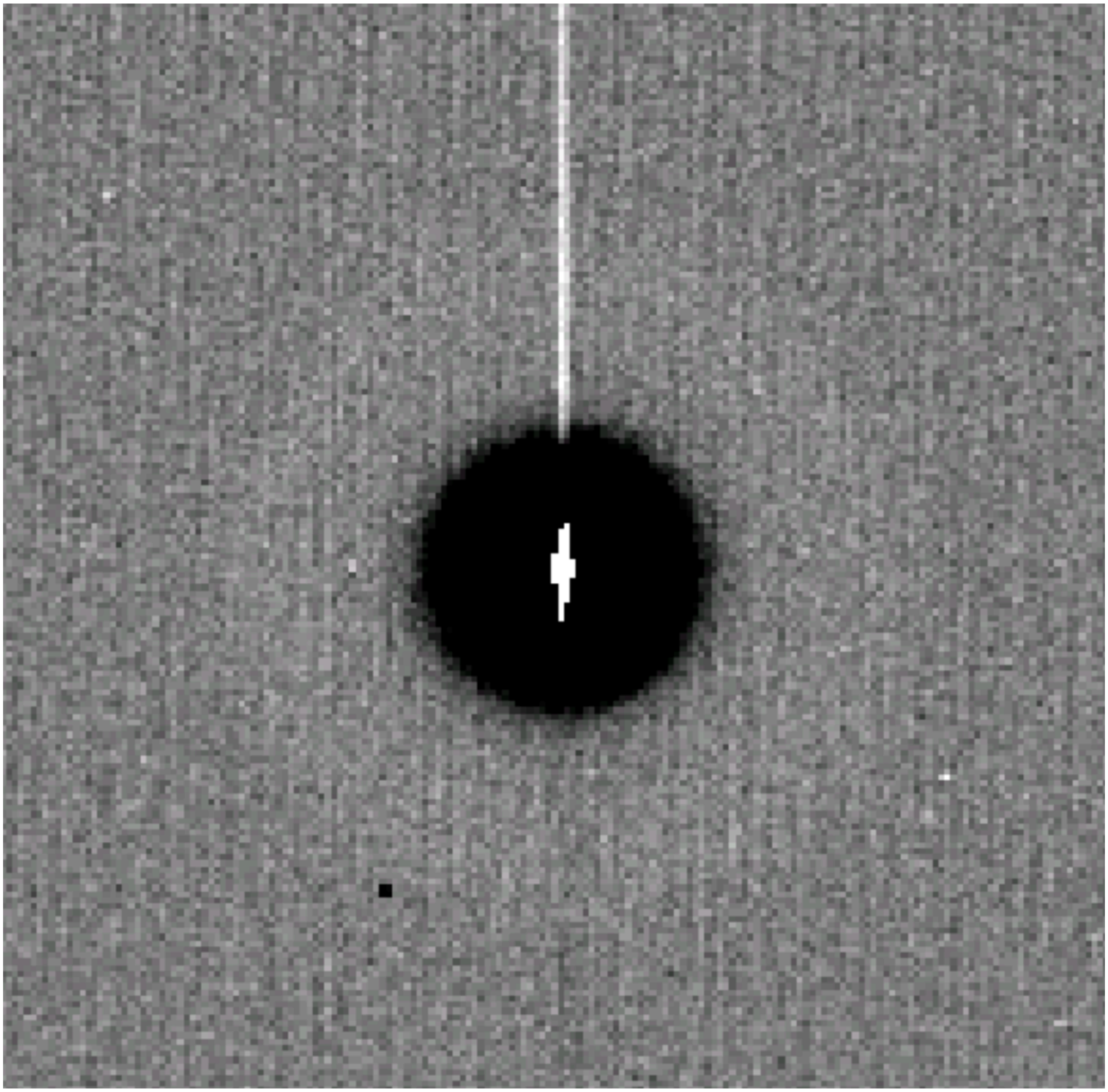

Figure 24: A close up of one of the largest vampire pixels. The bright core and region of depletion are clearly visible. Currently we only mask the core and depleted region, but will be extending this to mask the persistence-like trail that this feature leaves in the next few weeks.

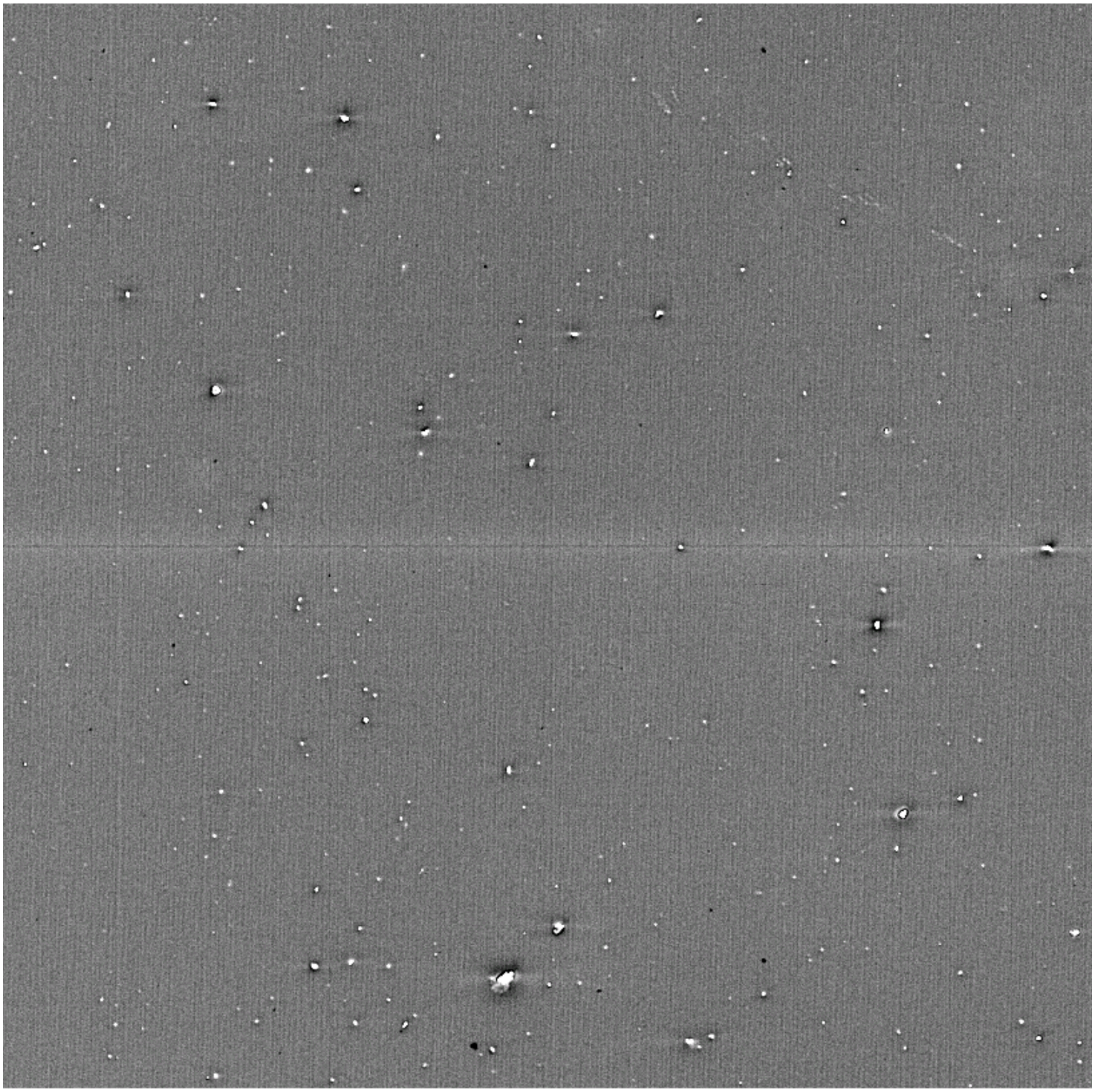

Figure 25: A view of detector R22_S10 in y-band, which has a large number of less significant vampire pixels.

A portion of 20241117 488

Figure 26: A portion of `day_obs 20241127 seq_num 488` showing the vertical bands which are apparently produced by very bright (saturated?) pixels.

5.2.4 Gain ratios

ComCam has been the first large-scale application of the updated “IsrTaskLSST” task, which uses a model of how the various signals combine to form the raw images to inform how we correct those signals during the ISR process. One improvement of this new task is that we now apply per-amplifier gains before flat correction, removing the gain component that was previously included in the flat correction. This results in the flat containing mainly QE and illumination patterns, which is much “flatter” than flats that also include gain terms (which offset the amplifiers relative to each other).

If we have properly diagonalized the flats and the gains, we would expect that applying the gain correction would create images with consistent sky levels across different amplifiers. However, when we look at images taken on-sky, our initial gain values result in some amplifiers being significantly different than their neighbors. The gains that we use are derived from the photon transfer curve (PTC), which uses flat pairs at different flux levels to monitor the properties of the noise. We have two of these sequences taken in the lab, and they disagree at the few percent level. This is similar in scale to the errors necessary to explain the on-sky differences. Further complicating this issue, the offsets seen in twilight data (used for flats) and that seen during the night also seem to differ. These differences so far have not been found to correlate with any device temperature, time, or voltage values. The gain correction fix appears to be stable, as we’ve only needed to generate and apply it once.

5.2.5 Crosstalk

We are currently using crosstalk values that were constructed by averaging the lab-based ITL measurements taken on LSSTCam. These are working better than expected, with residuals post correction being only a few electrons peak to peak. We plan to do a more complete crosstalk study using on-sky data, but the current results suggest that these lab measurements are sufficient for ComCam, and expect the same to be true for LSSTCam.

5.2.6 Twilight flats

There is no flat screen currently available for the main telescope, and so we have constructed twilight flats for all bands using exposures taken to have median counts between 15000-20000 ADU. We have some dithering in the inputs, which have allowed us to reduce the impact of

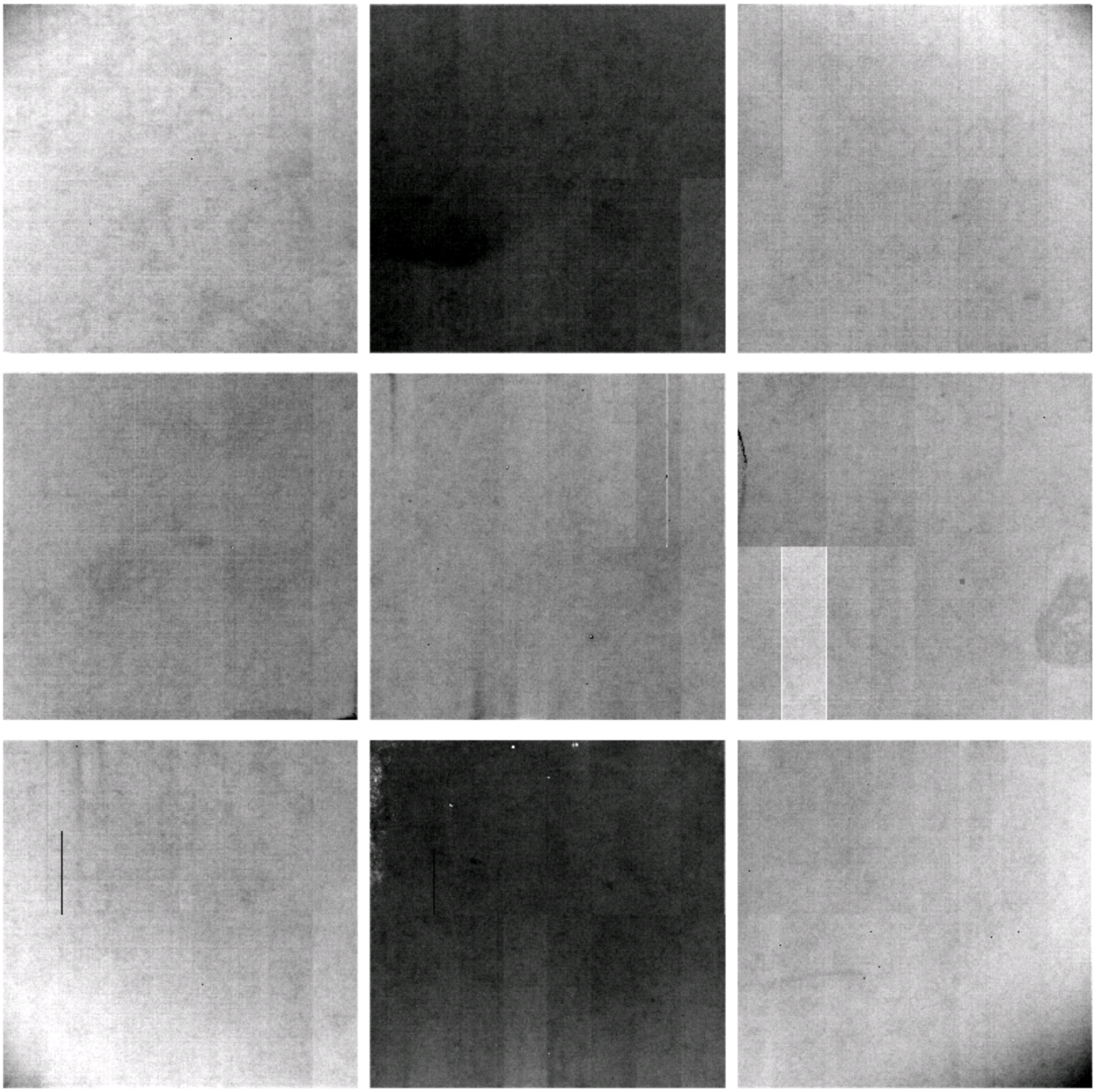

Figure 27: The ratio of the twilight-flat divided by a flat constructed from 94 r-band science frames. The scaling ranges from 0.9905 to 1.007. The visibility of amplifiers is caused by the unknown gain errors. The bottom right corner amplifier (C07) on R22_S21 is one of the indicator amplifiers, as it diverges from its neighbors. Although the C00-C03 amplifiers in R22_S12 also show significant offsets, these amplifiers also have an unrelated CTI issue, making them less reliable indicators.

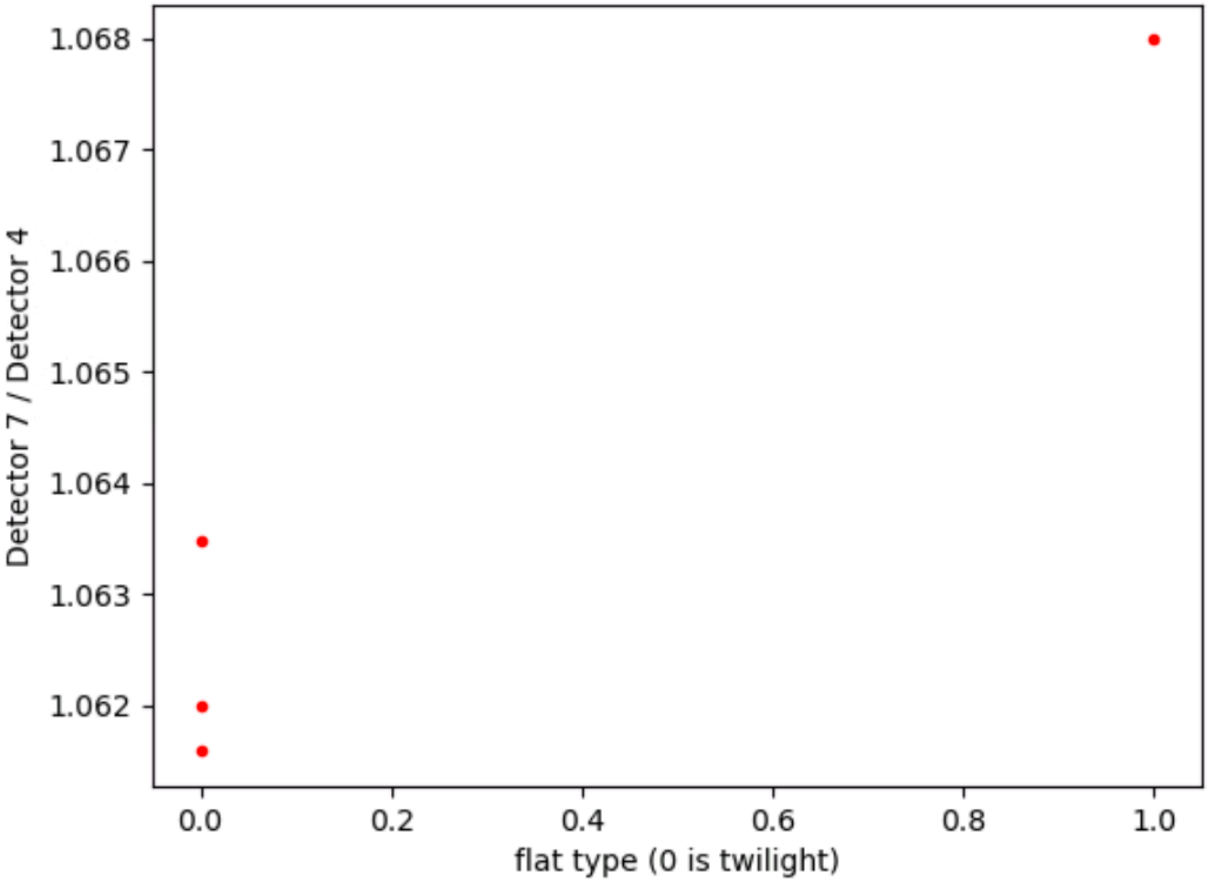

Figure 28: A comparison of the gain ratio between amplifiers in R22_S12. C07 is chosen as the indicator amplifier, and C04 is the reference. We have three twilight flat measurements taken at different rotator angles, and one from the 94 input sky flat.

stars that print through into the flat. This reduction of non-sky signals is imperfect, and an early i-band flat showed a satellite trail as a result; this was remedied with a more recent flat built using a larger number of exposures.

5.2.7 Operations

The Telescope and Auxiliary Instrumentation Calibration Acceptance Board (TAXICAB) has been meeting previously to discuss LATISS calibrations, and has been helping manage calibrations for ComCam. This process has not prevented problematic calibrations from being deployed (like the i-band flat with the satellite trail), but it has ensured that multiple people have checked some set of results. We are generating calibration verification reports regularly as part of this process (available at `https://s3df.slac.stanford.edu/people/czw/cpv_reports/`), and plan to add new metrics and checks to these as we discover more features of these detectors.

5.3 Collimated Beam Projector Status

The Collimated Beam Projector (CBP) and Ekspla tunable laser were both installed on the dome during the week of November 18. See Figs. 29, 30 They will both be connected to ethernet and a laser interlock system will be installed. First photon from the CBP is projected for December 2.

6 Astrometry

This is a quick update on astrometry quality based on data collected halfway through the ComCam observations. It is important to note that so far only single frame astrometric calibration is being done. Doing the additional global astrometric calibration with GBDES will further improve the results presented here.

For now, metrics like AM1 (the RMS of distances between star pairs separated by 5’ across all visits on a tract) appear to be satisfactory. On average, the median value across different filters is around 10 mas, as shown in Figure 31.

When examining the average astrometric residuals projected across the focal plane, some

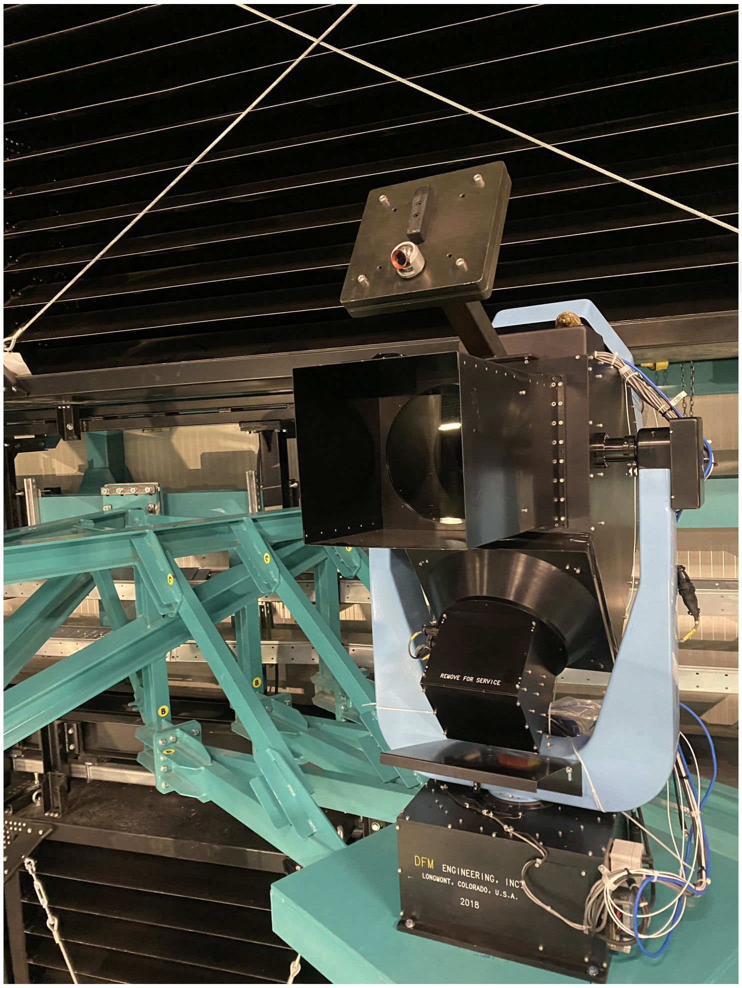

Figure 29: Image of the CBP, which was installed on the dome on November 22.

Figure 30: Image of the laser box, containing the Ekspla tunable laser, which was installed on the dome on November 21.

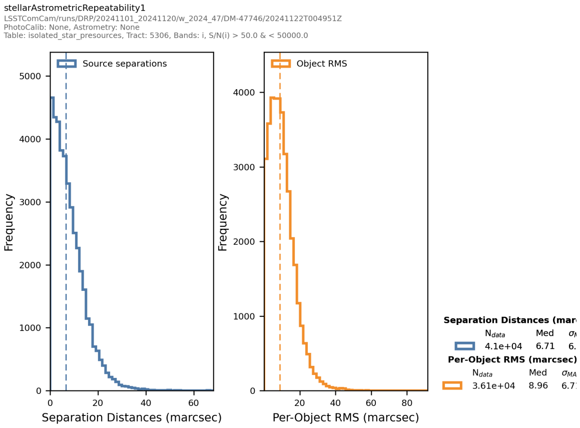

Figure 31: Stellar Astrometric repeatability in filter I in a given tract. AM1, which is the median of the orange histogram, is below 10 mas.

structures appear to be present, as in the example below in Fig 32. However, more data is needed to confirm whether these patterns are noise or systematic effects. It is likely that GBDES will help address these structures once it is activated. Personally, I don't think this could be noise, but it's fine to be noncommittal about causes here.

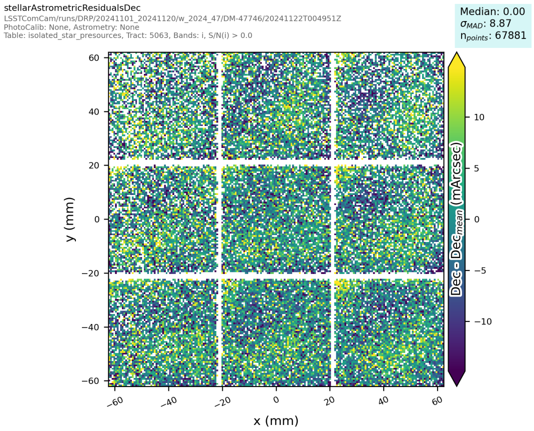

Figure 32: Declination residuals projected in Focal plane coordinate for a given tract. Some structure looks to be present in focal plane coordinates, which will be taken into account with GBDES.

7 Static-Sky Photometry

7.1 Photometric Calibration

We have started commissioning the full photometric calibration pipeline for Rubin Observatory, with great success so far. For testing photometric calibration we have obtained over 150 dithered science observations in ugriz over the Extended Chandra Deep Field-South (ECDFS) (one of the planned LSST deep fields), and tens more in rizy over the Euclid Deep Field South (EDFS). All of the science data has delivered seeing of ~ 0.8 to ~ 1.5 arcsecond seeing. The validation work in this document covers the ECDFS field with more complete filter coverage.

The precision photometric calibration software used for Rubin is the Forward Global Calibration Method (Burke, Rykoff, et al. 2018) which was used successfully to achieve better than 2 mmag uniformity for the Dark Energy Survey. This software has been adapted for the LSST Science Pipelines and has been used on Hyper Suprime Cam Special Survey Program (HSC SSP) for data releases since DR2.

The performance on HSC data has not been as good as that on DES data due to a number of reasons, yielding repeatability and uniformity closer to the 5 mmag level for grizy data. First, we have had a lot of problems with HSC backgrounds and amp-to-amp non-linearities. Second, the HSC survey strategy was not well suited to self calibration due to the slow slewing of the telescope and the long time required to change a filter, leading to lots of isolated single-band single-night surveys. Third, we do not have detailed throughput scans including detector-to-detector QE variations and in-situ scans of the significant filter variations that are required for the full forward modeling in FGCM.

Early calibration of the ComCam data is in many ways easier than that of HSC. First of all, we have a smaller camera (9 detectors) and thus fewer variations to have to cross-calibrate. Second, the camera is situated in the center and easiest to calibrate part of the focal plane. Third, we only have one field to calibrate across a few nights of data so far over a limited range of airmass. Fourth, the survey strategy (multiple bands per night dithered and repeated with overlapping filters from night to night) is well suited to self-calibration. On the other hand, we do not have the CBP set up yet, so we do not have detailed filter or detector scans available for ComCam, and are just using the LSSTCam reference filter throughputs and average detector throughput for the LSSTCam ITL detectors. In addition, we do not have a flat field screen so we have had to rely on twilight flat observations for flat fielding.

7.1.1 Processing Overview

We start with the standard ISR as documented in Section 5.2. While there are a number of challenges that we have discovered with the ITL detectors, these are mostly near the sky level, while the testing of photometric calibration is focused on brighter stars that are less affected by these issues. We then apply twilight flats, which we are investigating how to make better. At the same time, we are going to have the flat field screen and laser and projector installed prior to the commissioning of LSSTCam, so we do not want to spend too much time worrying about specific challenges of twilight flats which are only necessary for ComCam.

After flat fielding we find an initial point-spread function (PSF), do a star selection based on source and psf moments that was developed for HSC single-frame processing, and perform an initial astrometric solution and photometric solution (with a single zero-point per detector). The initial astrometric solution is used to associate star observations together prior to global photometric calibration with FGCM. The initial photometric solution is used for rapid analysis and prompt processing, but is not used at all for FGCM which relies entirely on instrumental fluxes (in units of electrons) with a minor constraint from the reference catalog.

7.1.2 Global Photometric Calibration with FGCM

All associated stars with observations with signal-to-noise greater than 10 are input into the FGCM solution. In addition, reference stars from The Monster reference catalog are associated with the stars . Only a small fraction of the reference stars are used in the FGCM solution, sufficient to estimate an “absolute” calibration (trusting that The Monster is a good absolute reference catalog). There is additional ongoing work with absolute calibration with respect to the CalSpec star C26202 which is not saturated in LSST images and is fortunately contained in ECDFS that is described below.

The FGCM model constrains the atmospheric parameters per night, as well as the absolute throughput relative to the input scans. The standard atmosphere is given by MODTRAN, run at the elevation of Cerro Pachon at airmass 1.2 with an Angstrom aerosol model. The optics and filters are all taken from *lsst/throughputs* version 1.9, and the detector throughput is taken from the ITL average of the lab scans ingested into *obs_lsst_data*. Note that the detector QEs are normalized to 1.0 at 800 nm, which is certainly greater than the true QE at this wavelength.

7.1.3 FGCM Results on the ECDFS Field

The FGCM results presented here are based on the `LSSTComCam/runs/DRP/20241101_20241113/w_2024_46/DM-47566` DRP processing run, specifically the 157 visits overlapping tracts 4847,4848,4849,5062,5063,5064 which are in the ECDFS field. Specifically there are 28, 18, 38, 45, 28 visits in ugriz respectively. All QA plots are available in the plot navigator at https://usdf-rsp.slac.stanford.edu/plot-navigator in the collection `u/erykoff/LSSTComCam/DM-47303/test2/build2/run9`. In this section we focus on some of the highlights.

Note that FGCM defines a “photometric” observation as one that is consistent with the forward model, including normal variations in the atmosphere, airmass, known detector throughputs, filter curves, and additional accomodation for aperture corrections (discussed in Burke, Rykoff et al). With this definition fully 92% of the observations were deemed to be photometric by the code.

7.1.3.1 Illumination Corrections

Part of the FGCM solution is generating illumination correction maps, with a second-order 2D Chebyshev polynomial over each detector. Prior to LSSTCam commissioning this will be turned into a separate calibration product generated from dense dithered star field observations (Y1) or from the CBP (future years). We have not yet done dithered observations with ComCam over a dense field, only high latitude, which limits the precision. Nevertheless we are able to constrain reasonable illumination corrections. The offsets from detector to detector in the illumination correction are due to unexpected offsets in the twilight flats that we are investigating.

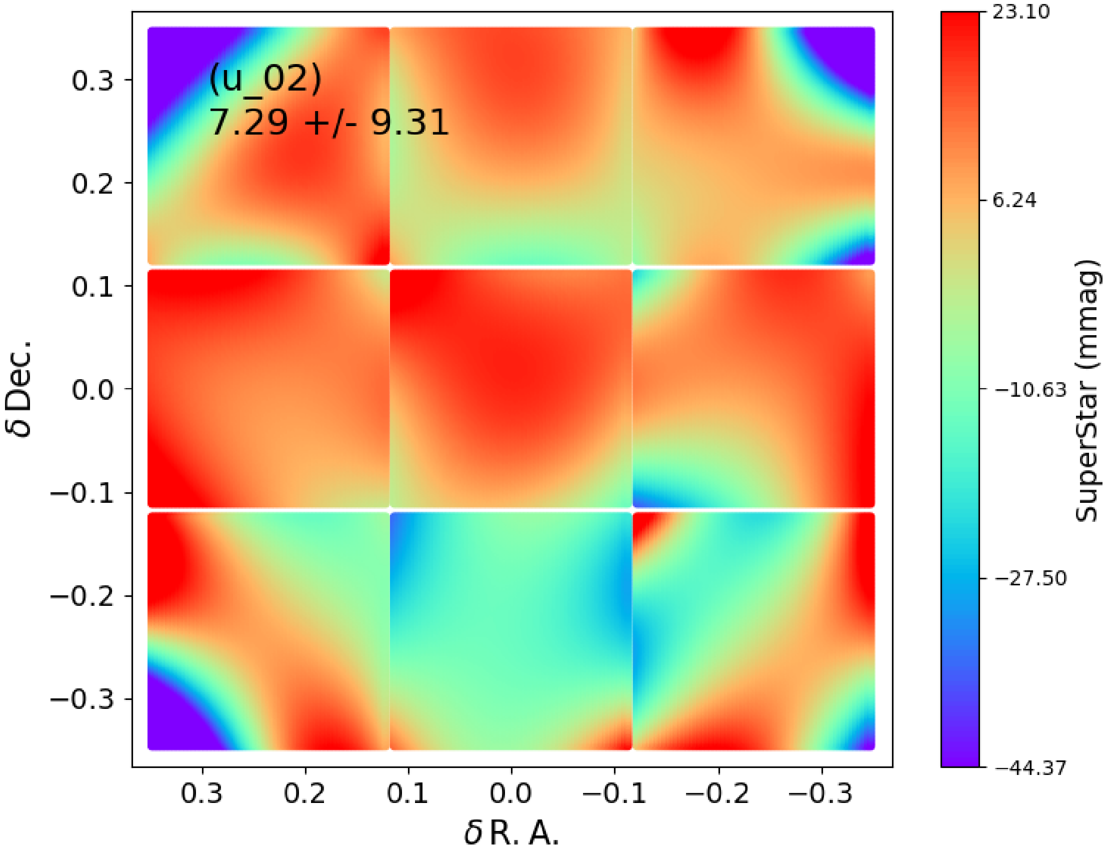

Figure 33: Illumination correction derived from FGCM for the u band.

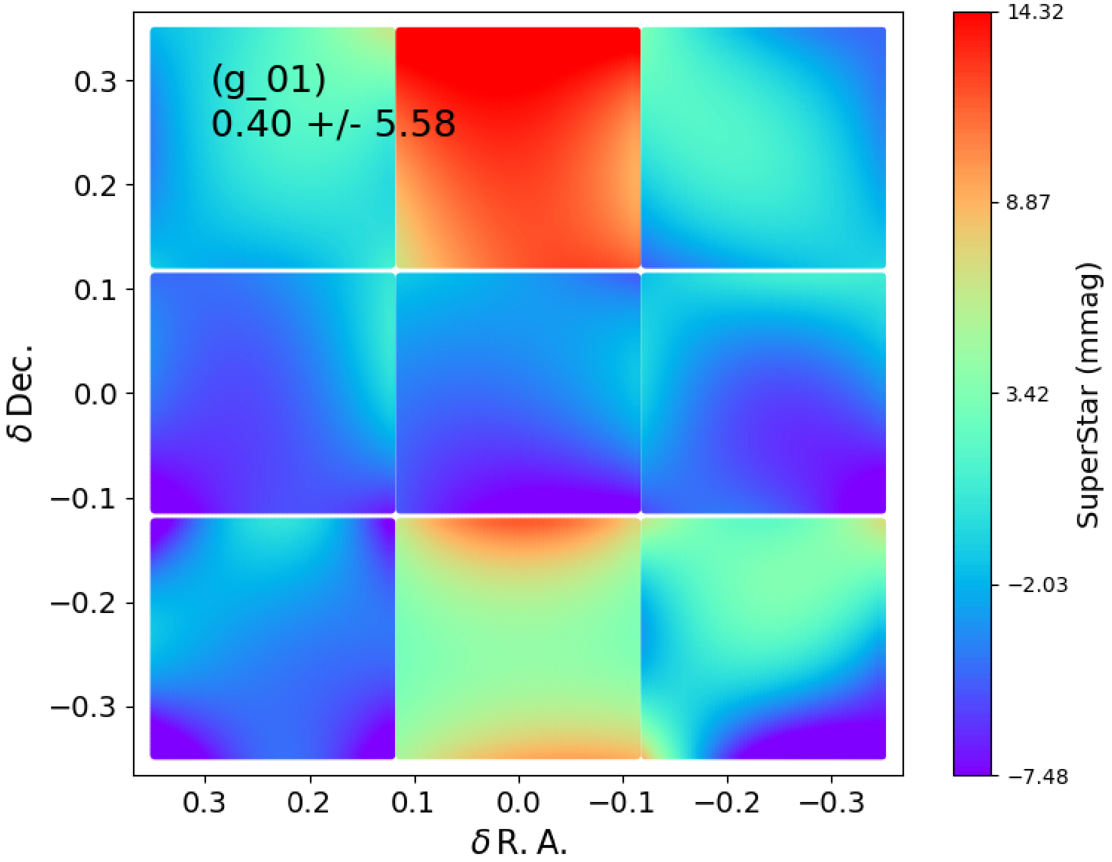

Figure 34: Illumination correction derived from FGCM for the g band.

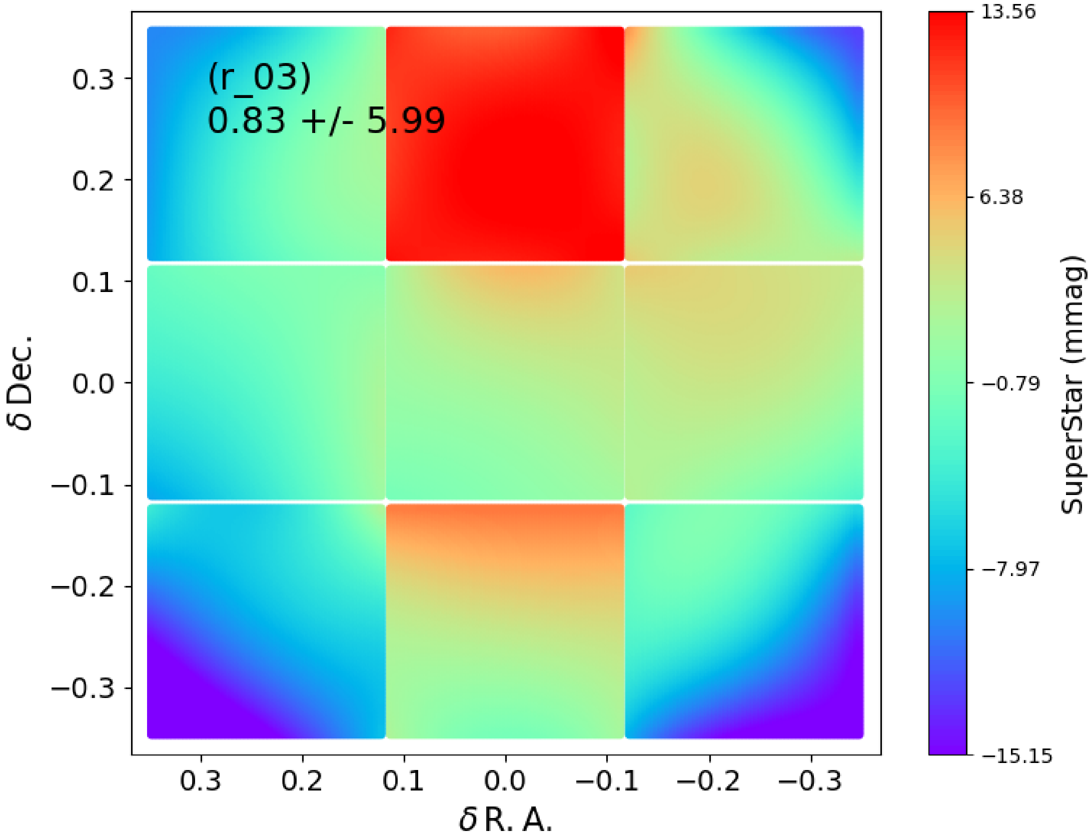

Figure 35: Illumination correction derived from FGCM for the r band.

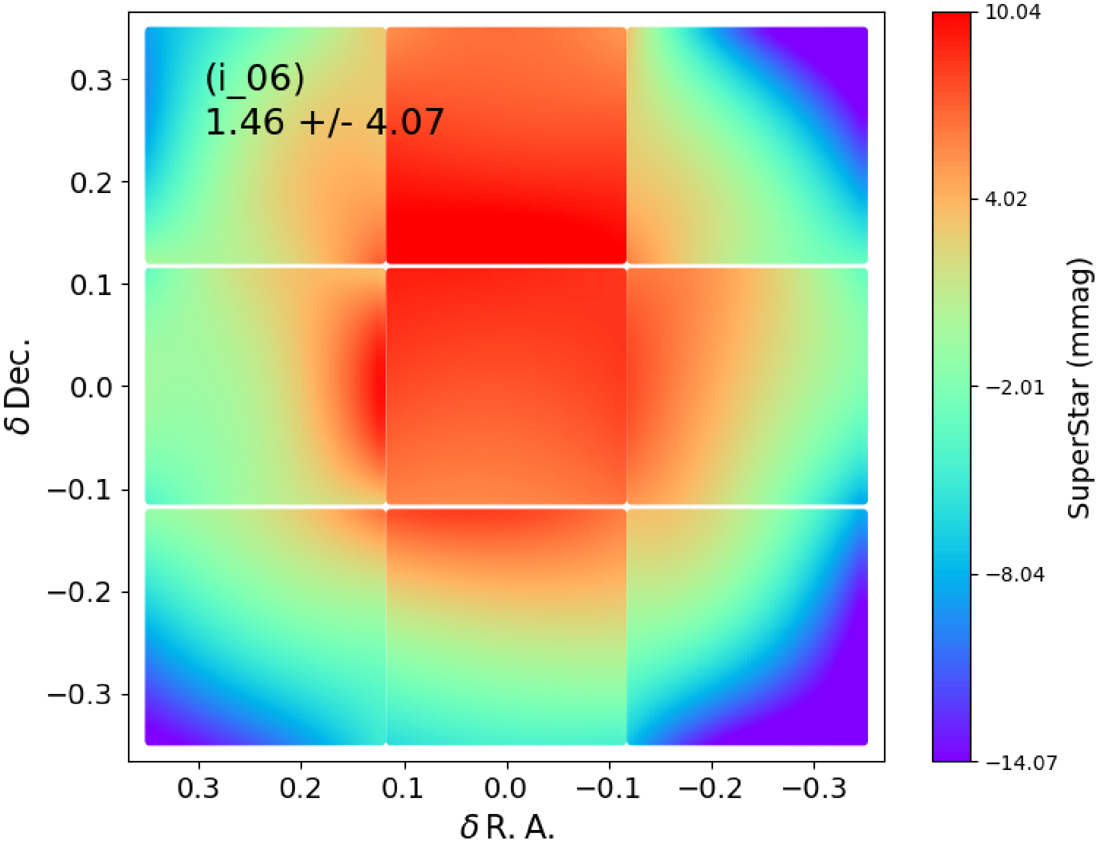

Figure 36: Illumination correction derived from FGCM for the i band.

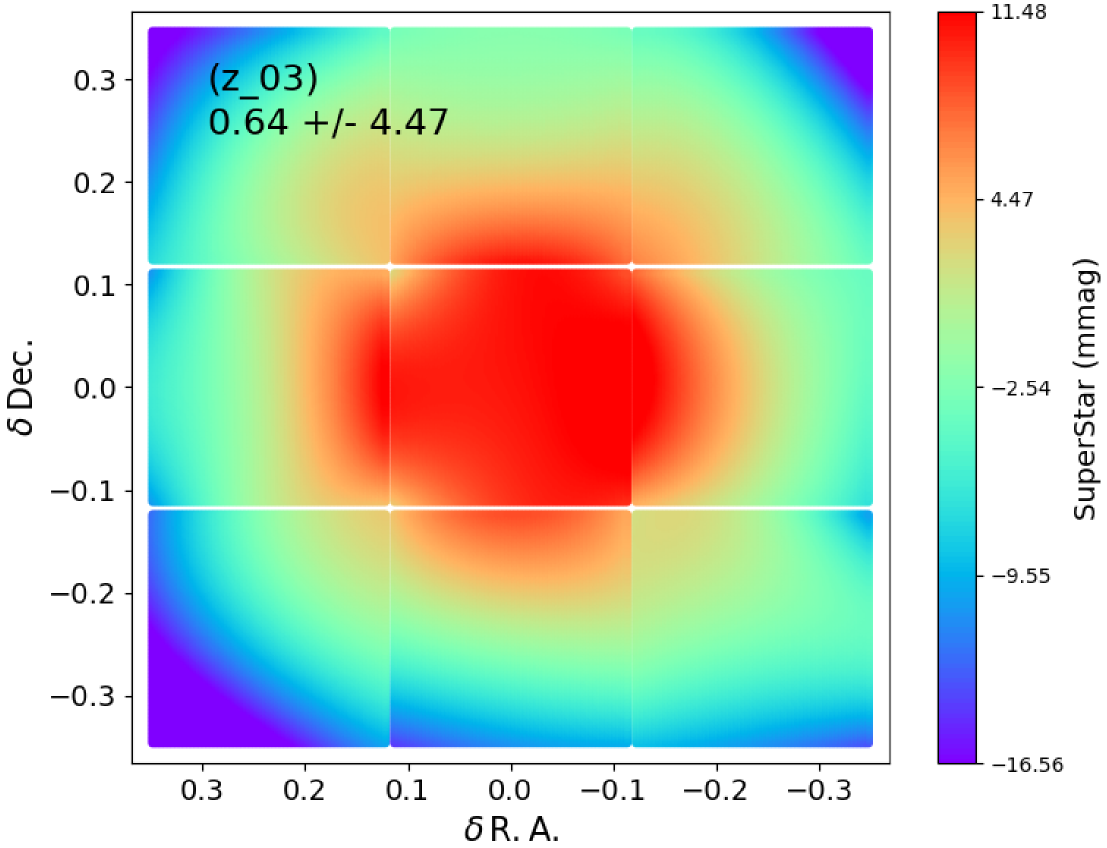

Figure 37: Illumination correction derived from FGCM for the z band.

7.1.3.2 Photometric Repeatability

The photometric repeatability after the FGCM fits was excellent. We show here the repeatability histograms, after all chromatic corrections, for the stars used in the fit ("all stars"). Although 10% of the stars are reserved, the histograms do not yet have good statistics. These plots are all made with signal-to-noise greater than 100 stars (with better than 1% photometric errors). Therefore the scatter is often dominated by photometric error. The label "sigma_fgcm" is meant as an estimate of the intrinsic scatter after subtracting off the photometric error in quadrature. The plots are split into four panels, showing all stars, the 25% bluest (from $g - i$ color), the 50% middle color, and the 25% reddest stars. Note that the reddest stars tend to be fainter and thus have larger photometric error. Furthermore, there are no red stars observed in the u-band. In all cases except the u-band the intrinsic repeatability is 1 mmag or better, and for the u-band it is better than 5 mmag, comfortably exceeding our requirements.

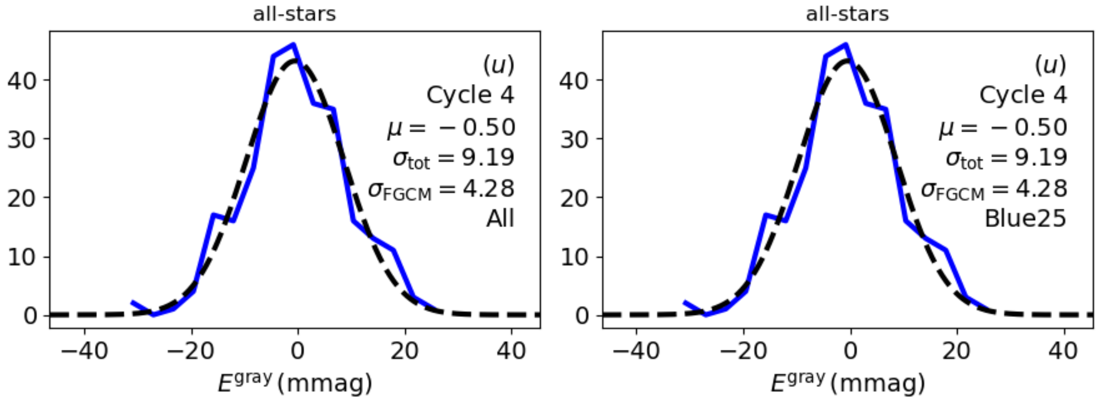

Figure 38: Photometric repeatability for stars in the u band.

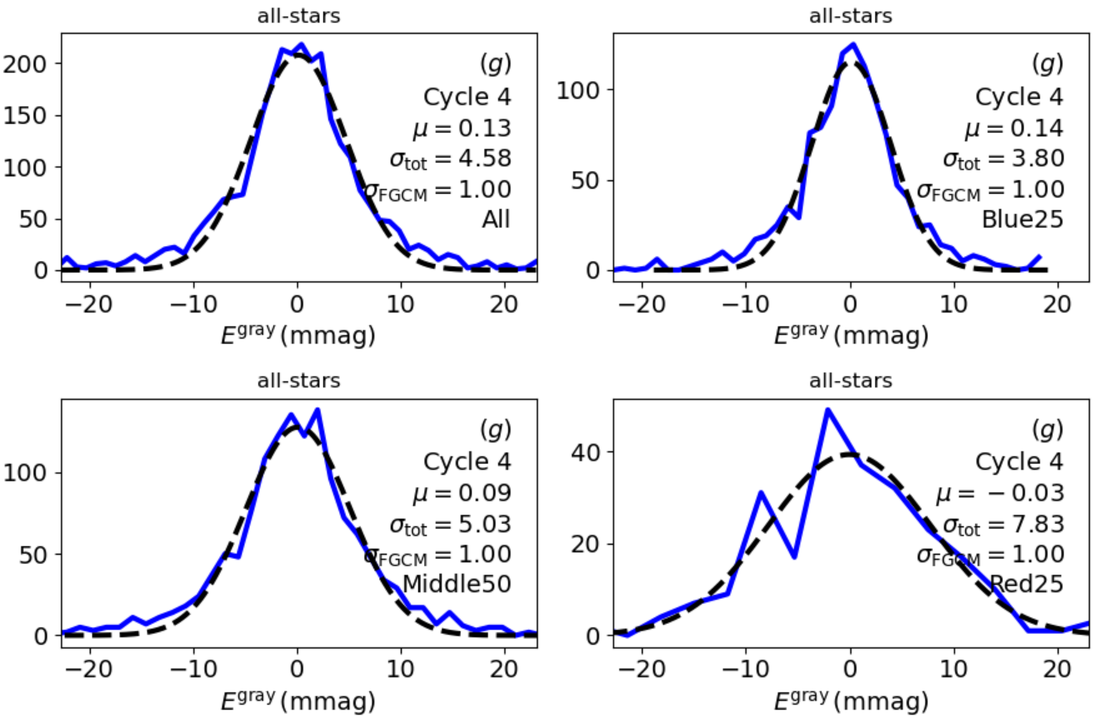

Figure 39: Photometric repeatability for stars in the g band.

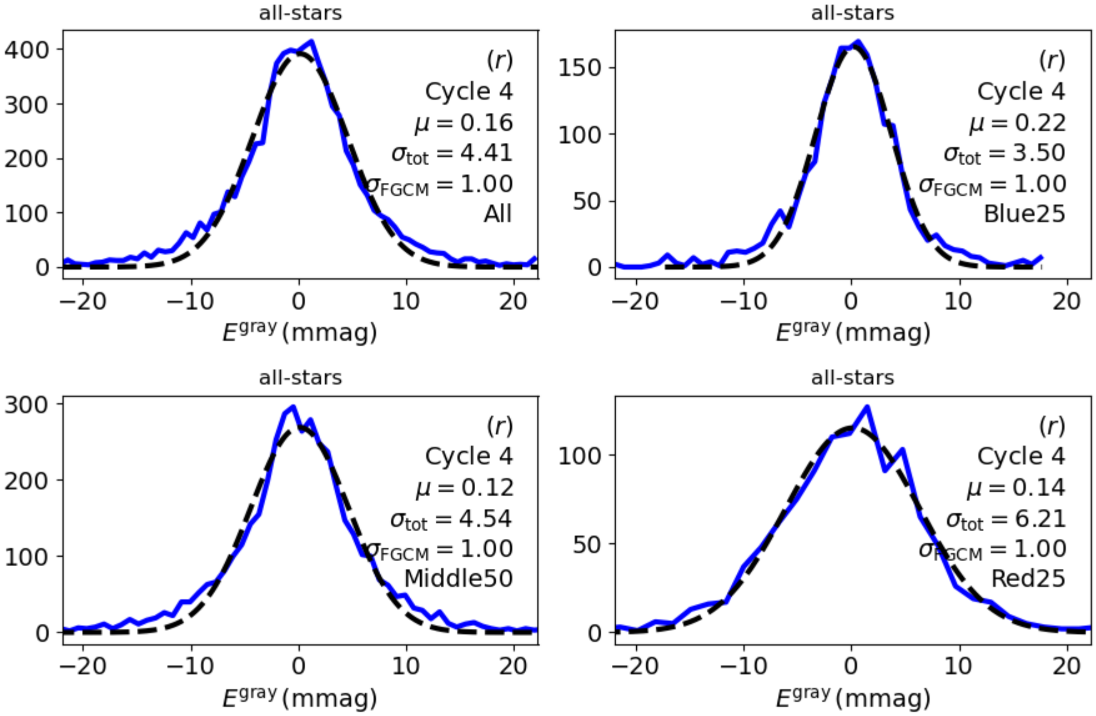

Figure 40: Photometric repeatability for stars in the r band.

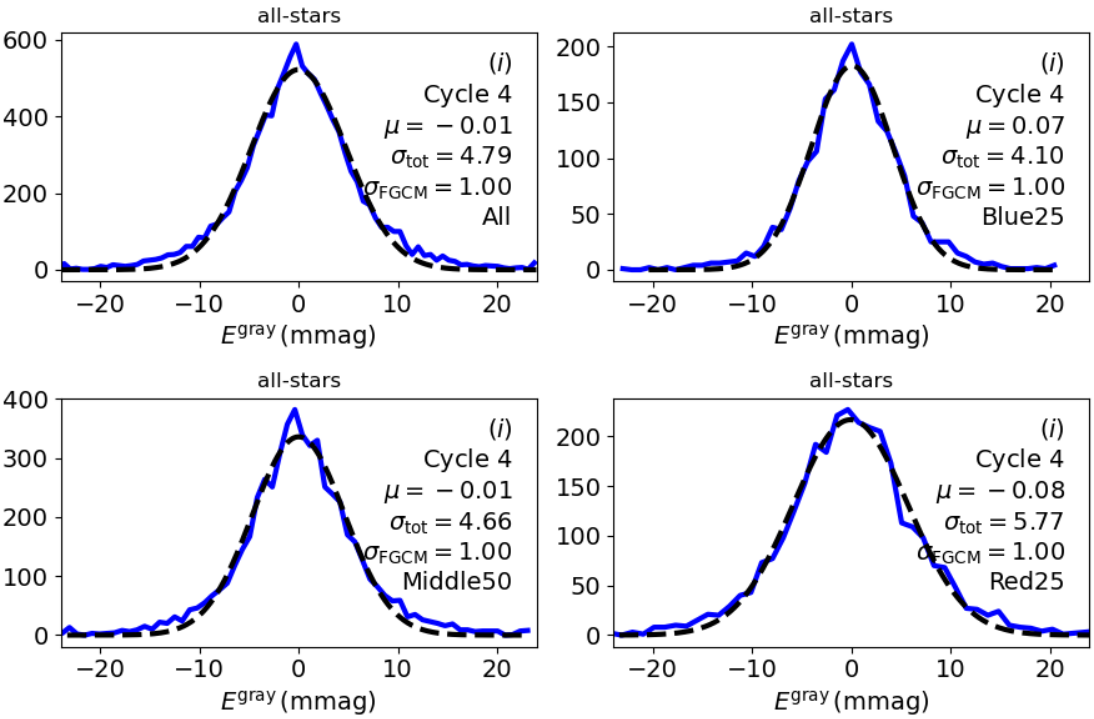

Figure 41: Photometric repeatability for stars in the i band.

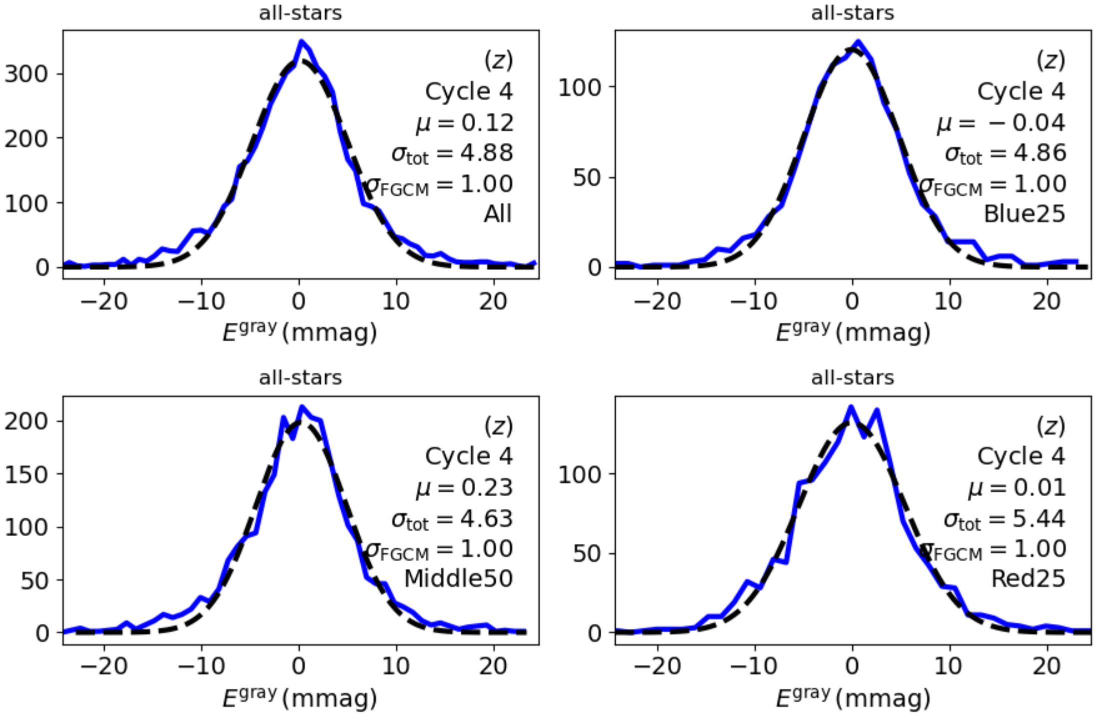

Figure 42: Photometric repeatability for stars in the z band.

7.1.3.3 Detector Chromaticity Fits

In the absence of full in-situ throughput scans, we additionally constrain the “chromaticity” of the detectors, which is a first-order adjustment to the slope of the peak of the throughput curve per-detector. By doing this adjustment in throughput space rather than color space we can preserve the forward model approach, and additionally apply these corrections to any SED. Note that this operation assumes that the filters are perfectly known, and it is only the detector throughput that is varying. This is, in general, a valid assumption in the g band where the AR coating varies from detector to detector causing chromatic differences in this band.

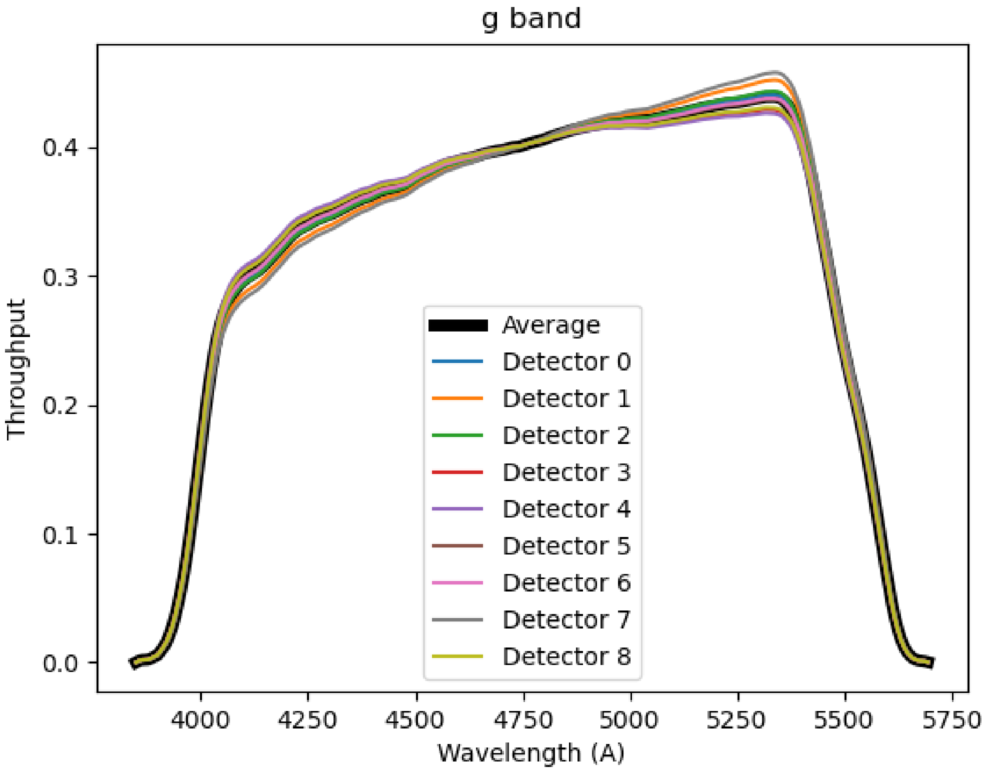

Figure 43: Variation in throughput in the g band for the 9 ComCam detectors as derived from star colors. These are all constrained relative to the average ITL throughput. The CBP will be used for making this measurement “correctly”, but this serves as a prediction of what variations the CBP scans should observe if we have it running on ComCam.

7.1.3.4 Absolute Throughputs

The FGCM fit performs a “dead reckoning” of the expected absolute throughput given the telescope aperture, the effective gain, the standard atmosphere, and the various throughputs input. See above for the throughputs assumed. If we trust The Monster reference catalog for absolute calibration, Figure 44 shows the comparison of the delivered throughput to the predicted throughput. In griz bands it is very close, given that (a) we know that the peak detector QE is not 100%; and (b) the ComCam front lens did not have an AR coat applied, thus reducing its throughput relative to nominal LSSTCam lenses. In u band we are getting more throughput than predicted. This may be an issue with the reference catalog, or our ComCam u-band QE is 20-30% larger than the baseline expectation. Given how fast the detector QE falls off in the u-band, it would not take much to increase the throughput by this factor.

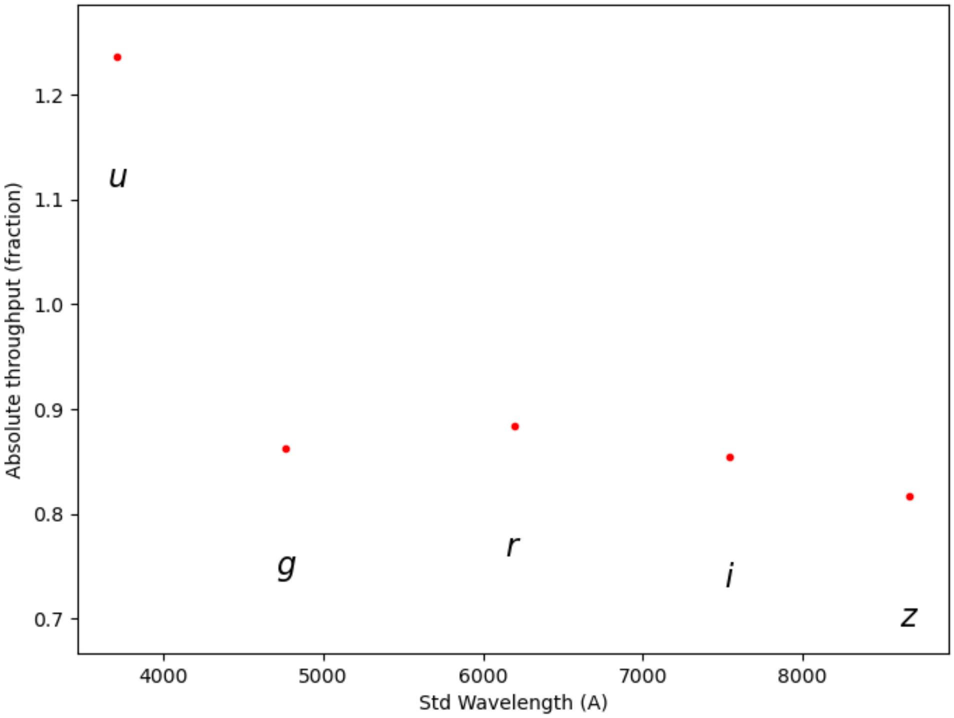

Figure 44: Absolute throughput derived per band, relative to naive expectations.

We have additional ongoing studies of absolute throughputs using the CalSpec standard C26202 directly.

7.1.3.5 Comparison to The Monster

Given our calibrated stars from the FGCM fit we can compare the magnitudes as a function of color against The Monster reference catalog. The “lsst” fluxes in The Monster were derived by using stellar spectra to convert from The Monster native DES system to the standard throughputs in lsst/throughputs v1.9. These do not match ComCam, in particular it used a strange hybrid of ITL/E2V for the detector throughput, which is not correct for ComCam. Therefore, we do expect residual color terms. Studies are ongoing on whether these color terms are expected given the differences between the ComCam throughput and the predicted LSST throughput. Further validation will be possible if we get CBP scans prior to the removal of ComCam.

7.1.3.6 Background Oversubtraction

As a side-effect in the calibration, FGCM tests local background oversubtraction by looking at the statistical difference between two large aperture magnitudes. If the background were perfectly measured then the difference in magnitude will just be a measure of the wings of the PSF (a local portion of the growth curve) which should be self-similar for all star fluxes. Instead, we generally see a downturn consistent with a constant background offset. This background oversubtraction has been seen in DES, HSC, and ComCamSim data at similar levels with different photometric pipelines. It is worse in the redder bands. It seems to be caused by the far wings of stars (in DES all stars and galaxies brighter than 17th magnitude in i contribute), as well as possibly due to faint undetected sources. This same background oversubtraction effect is seen in the ComCam images. Further investigations are being done by the low-surface-brightness science unit.

7.1.4 Next Steps

The following additional data will need be taken to advance from our current knowledge:

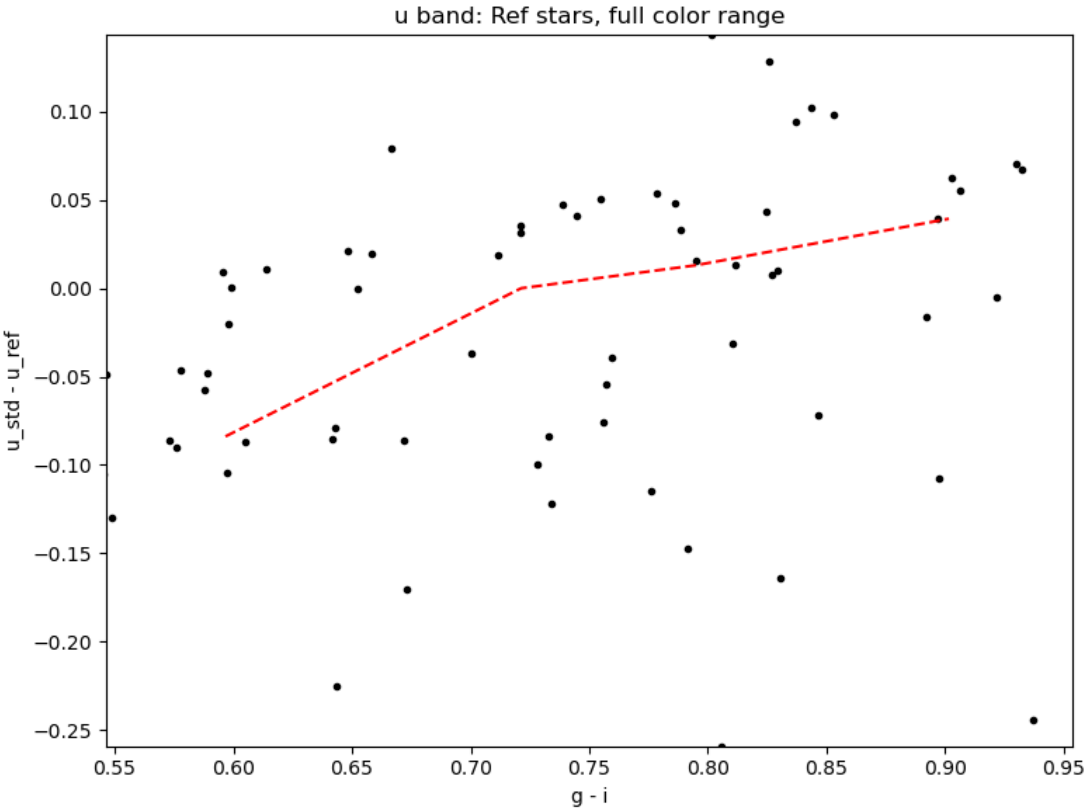

Figure 45: Residuals between FGCM standardized magnitudes and The Monster predicted LSST magnitudes for the u band as a function of $g - i$, assuming The Monster has the correct absolute throughput.

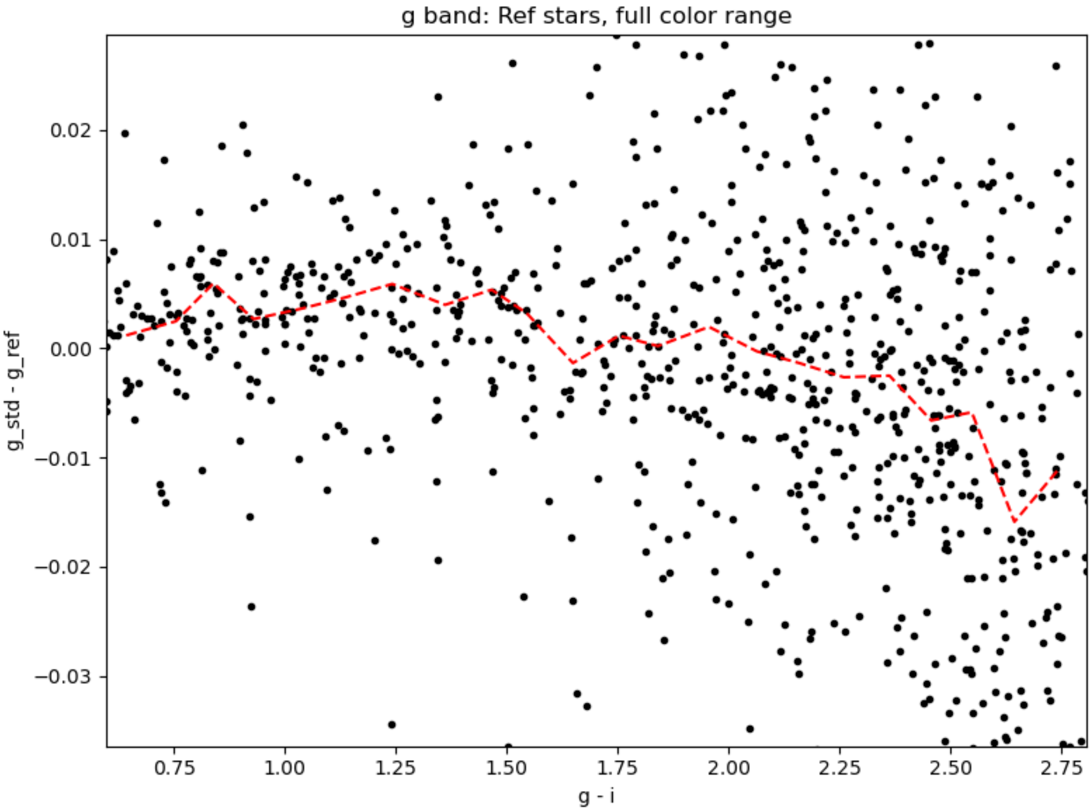

Figure 46: Residuals between FGCM standardized magnitudes and The Monster predicted LSST magnitudes for the g band as a function of $g - i$, assuming The Monster has the correct absolute throughput.

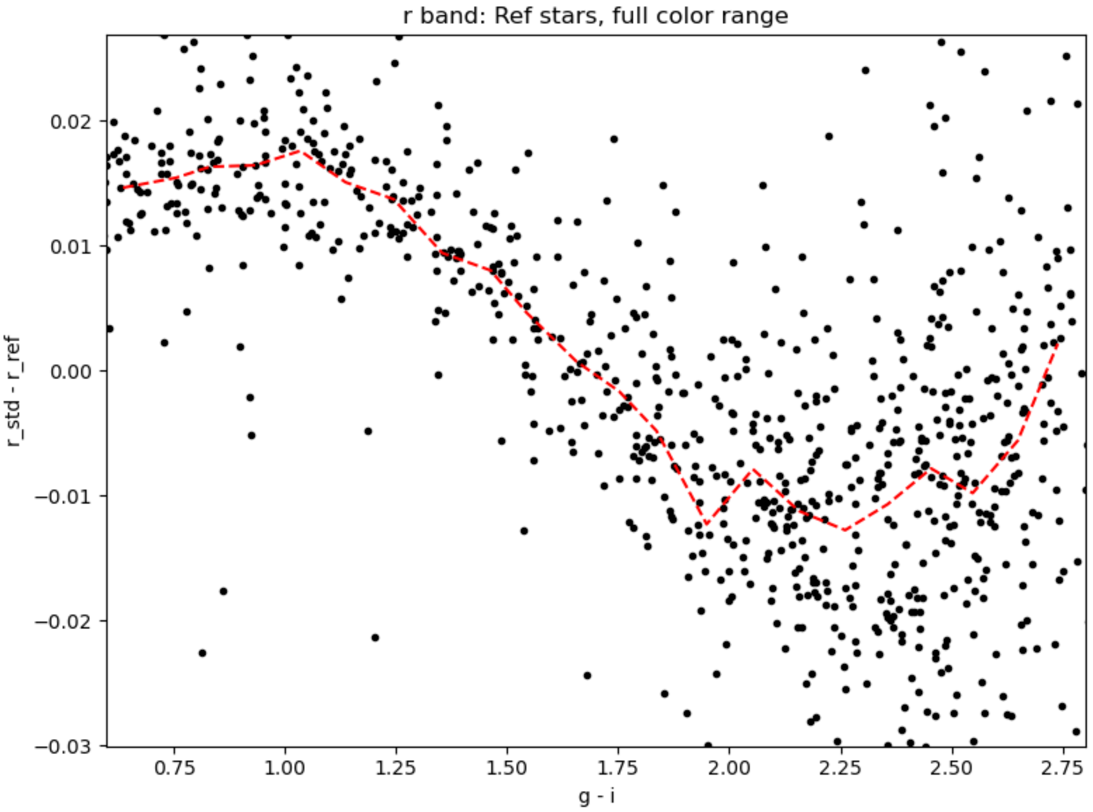

Figure 47: Residuals between FGCM standardized magnitudes and The Monster predicted LSST magnitudes for the r band as a function of $g - i$, assuming The Monster has the correct absolute throughput.

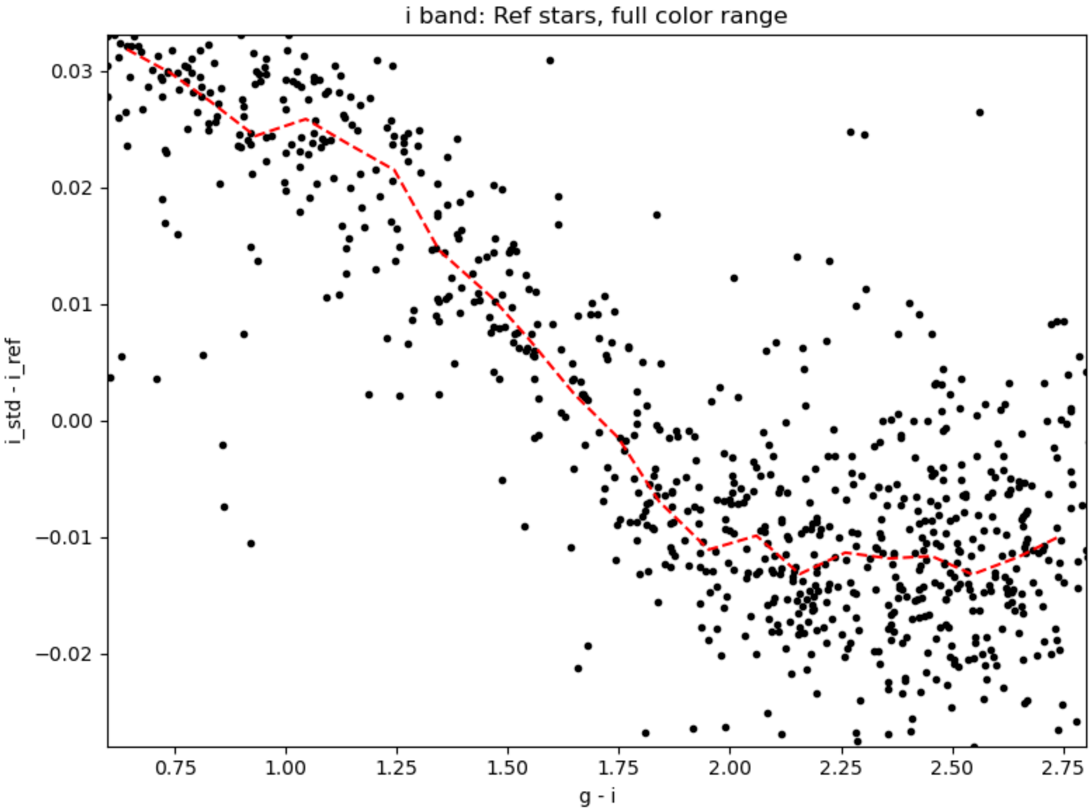

Figure 48: Residuals between FGCM standardized magnitudes and The Monster predicted LSST magnitudes for the i band as a function of $g - i$, assuming The Monster has the correct absolute throughput.

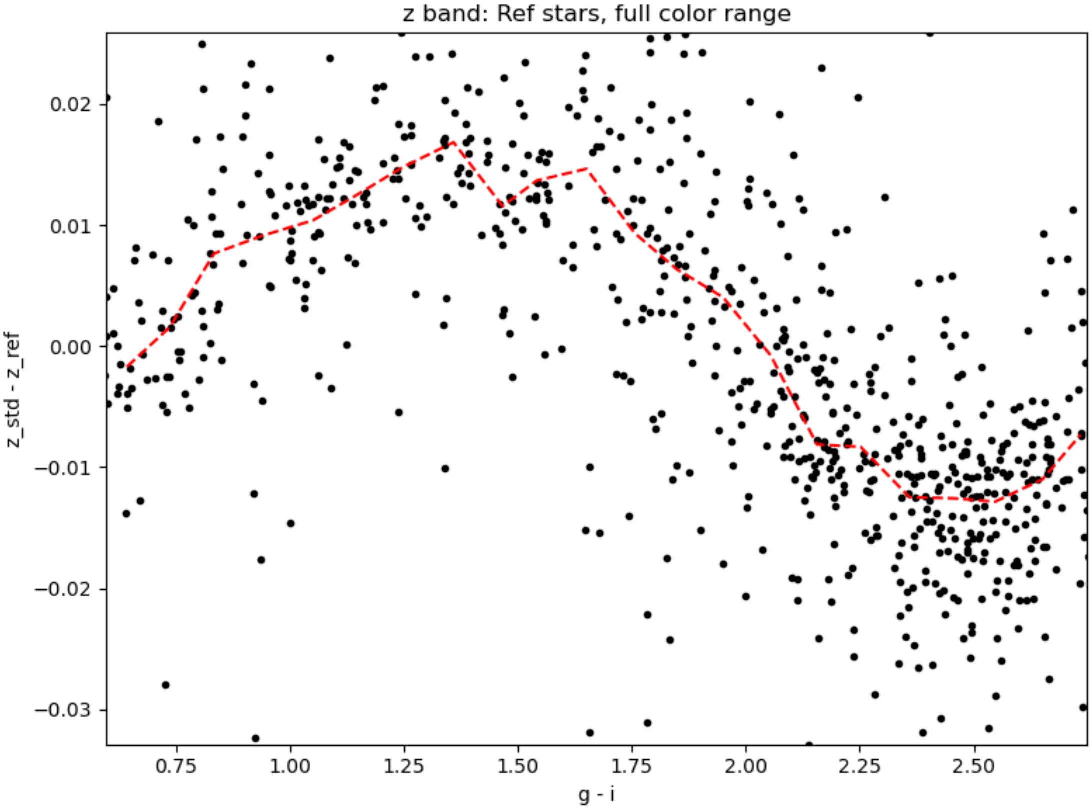

Figure 49: Residuals between FGCM standardized magnitudes and The Monster predicted LSST magnitudes for the z band as a function of $g - i$, assuming The Monster has the correct absolute throughput.

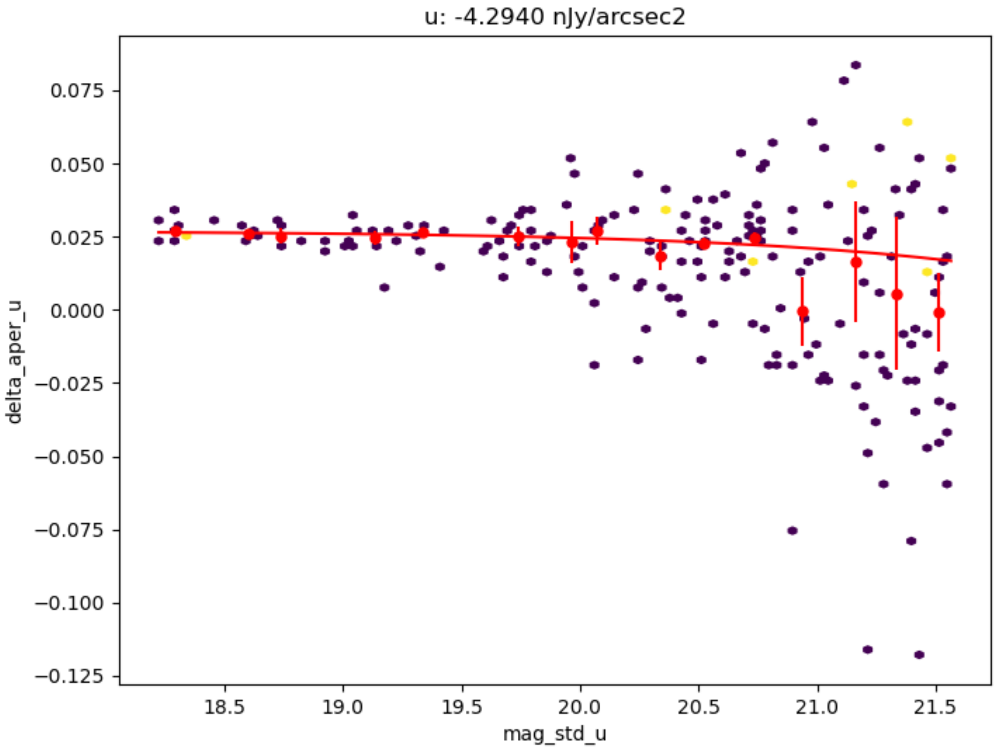

Figure 50: Estimate of the background oversubtraction using delta magnitudes from large apertures in the u band. The amount of curvature is a measure of the oversubtraction; this should be flat as a function of star magnitude if the background were measured correctly on average.

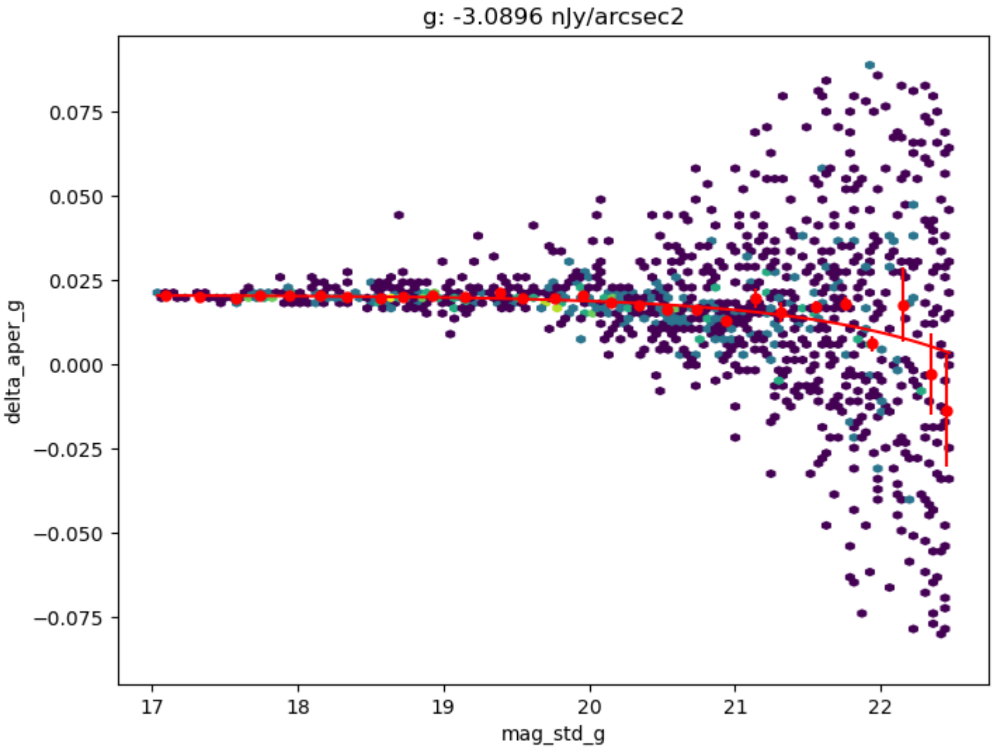

Figure 51: Estimate of the background oversubtraction using delta magnitudes from large apertures in the g band. The amount of curvature is a measure of the oversubtraction; this should be flat as a function of star magnitude if the background were measured correctly on average.

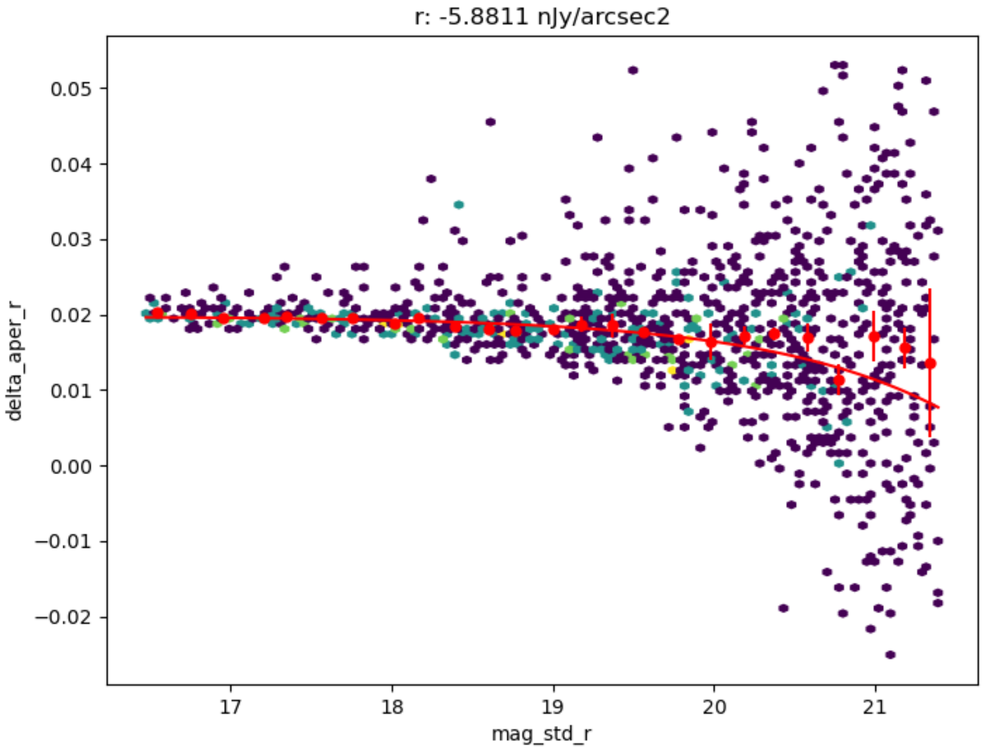

Figure 52: Estimate of the background oversubtraction using delta magnitudes from large apertures in the r band. The amount of curvature is a measure of the oversubtraction; this should be flat as a function of star magnitude if the background were measured correctly on average.

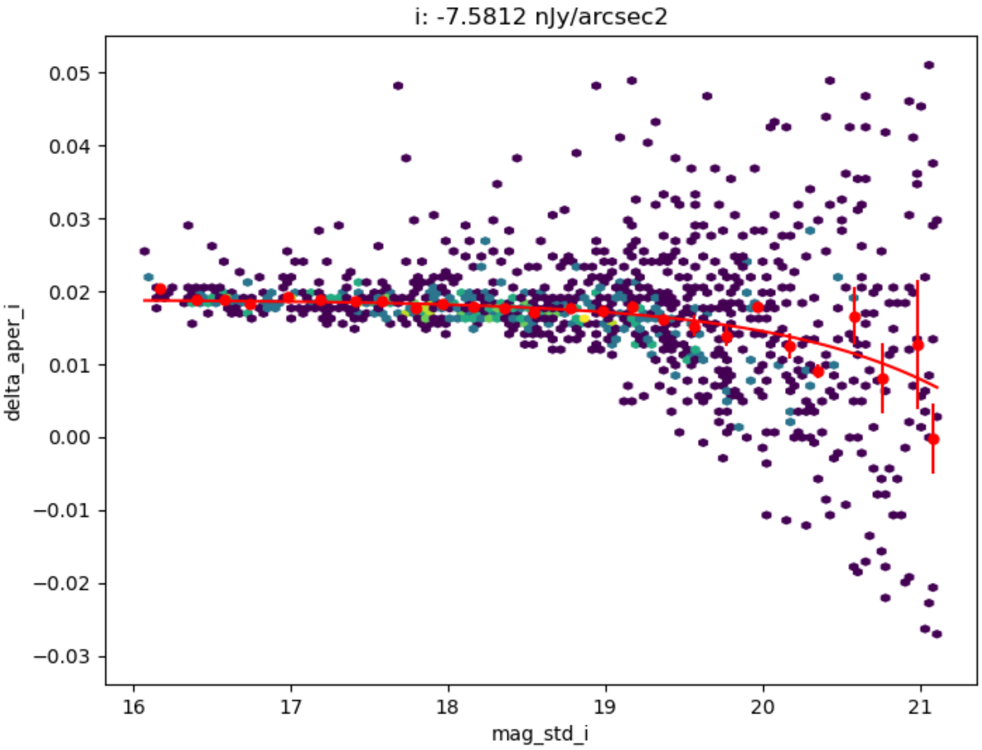

Figure 53: Estimate of the background oversubtraction using delta magnitudes from large apertures in the i band. The amount of curvature is a measure of the oversubtraction; this should be flat as a function of star magnitude if the background were measured correctly on average.

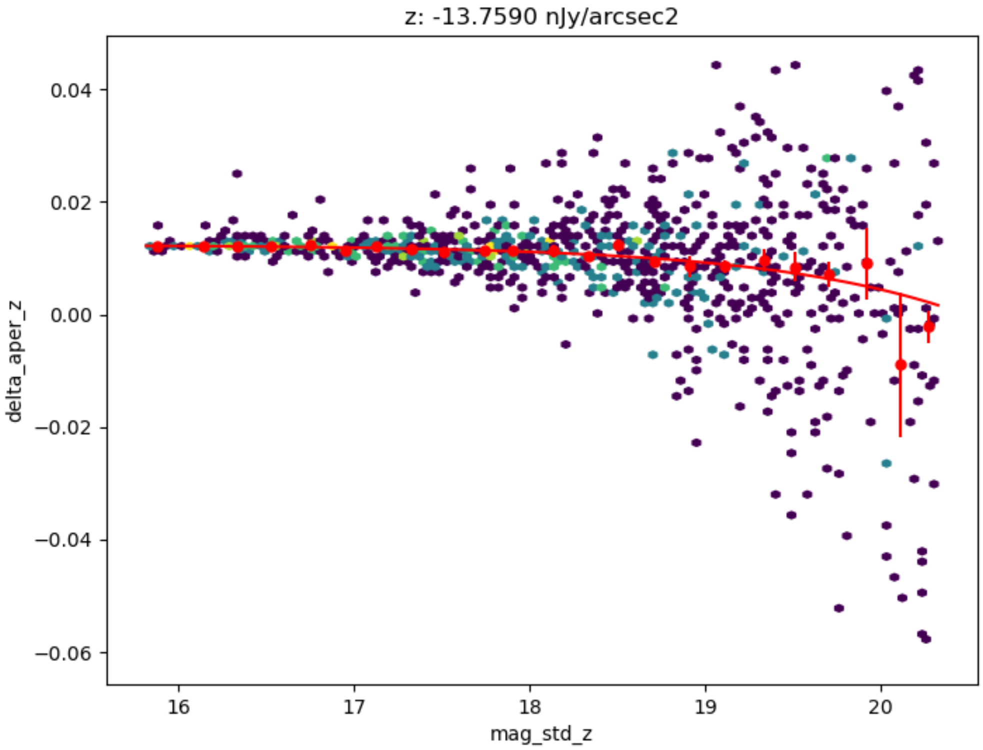

Figure 54: Estimate of the background oversubtraction using delta magnitudes from large apertures in the z band. The amount of curvature is a measure of the oversubtraction; this should be flat as a function of star magnitude if the background were measured correctly on average.

1. g band observations in the EDFS field, when the g filter is put back into ComCam for the upcoming dark time.
2. Dithered observations in as many bands as possible over a field with much larger stellar density for better illumination corrections.
3. More contiguous dithered survey data in (at least) gri.

The particular emphasis on g band in these requests is that by default FGCM will use the $g - i$ color for internal QA, which is a very useful color to split on. There are no facilities in the code for doing quality calibrations on multiple disconnected fields with different band coverage, as this is not the normal case for survey observations. We could run different fields separately with different configs, but this is not preferred. Thus, gri coverage over the fields of interest for DRP processing is the “easiest” path that will yield the best results and be most consistent with the LSST survey.

7.2 A Comparison with the HST CalSpec Standard C26202

It was fortuitous that ECDFS field observed by ComCom during commissioning contained an HST CalSpec standard that was faint enough not to saturate the ComCam science images. This HST CalSpec standard, C26202, had previously been used to perform the absolute AB calibration of the Dark Energy Survey (DES) Data Release 2 (DR2) (citation).

For the ComCam analysis, two separate (but related) analyses were performed using the ComCam observations of C26202: (1) a measurement of the absolute throughput of the ComCam $ugrizy$ bandpasses, and (2) a measurement of how far off the initial absolute photometric calibrations were from the AB magnitude system (“AB offsets”) for these same bandpasses.

These two analyses are discussed below.

7.2.1 Absolute Throughput Measurements

TBD

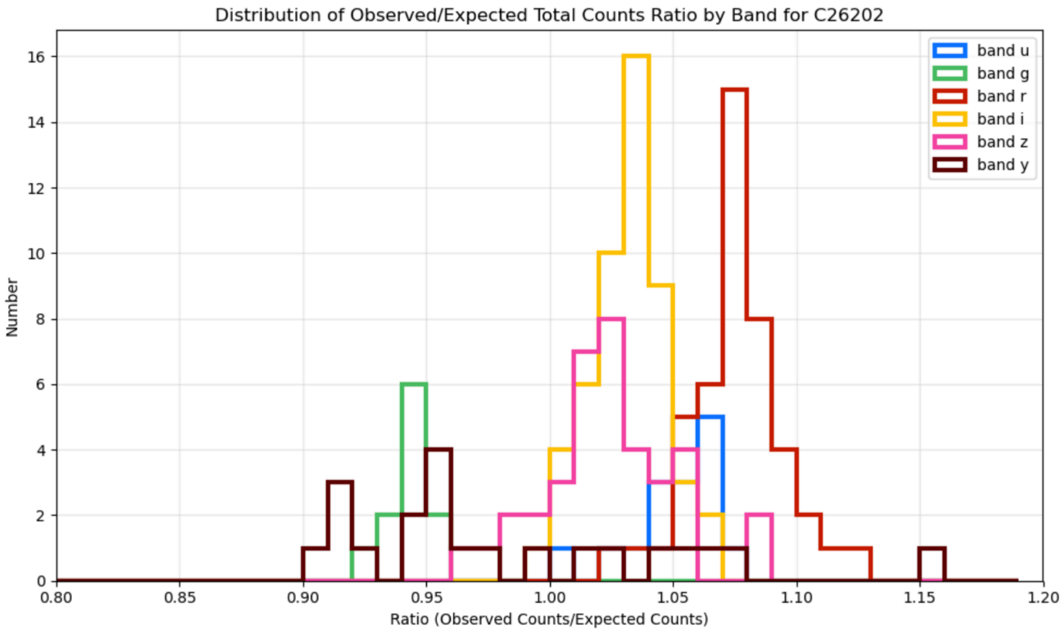

Figure 55: TBD.

7.2.2 AB Offsets

TBD

7.3 Galaxy Photometry

Galaxy photometry investigations so far have used the Extended Chandra Deep Field-South (ECDFS) due to the availability of public external reference data, including space-based imaging from the Hubble Space Telescope (HST). Broadly, we have done (or soon will be doing) comparisons to matches against external catalogs and from synthetic source injection (SSI) in coadds. Some preliminary investigations were done with visual inspection of external images.

7.3.1 Comparison to External Imaging

We downloaded a subset of the Hubble Legacy Fields (HLF, `https://archive.stsci.edu/prepds/hlf/`) imaging for the GOODS-South field, which included programs covering the original Chandra Deep Field-South and parallel fields now part of ECDFS. Significantly overlapping coverage is available in F435W, F606W, F775W and F814W, as well as four redder bands. F775W is of

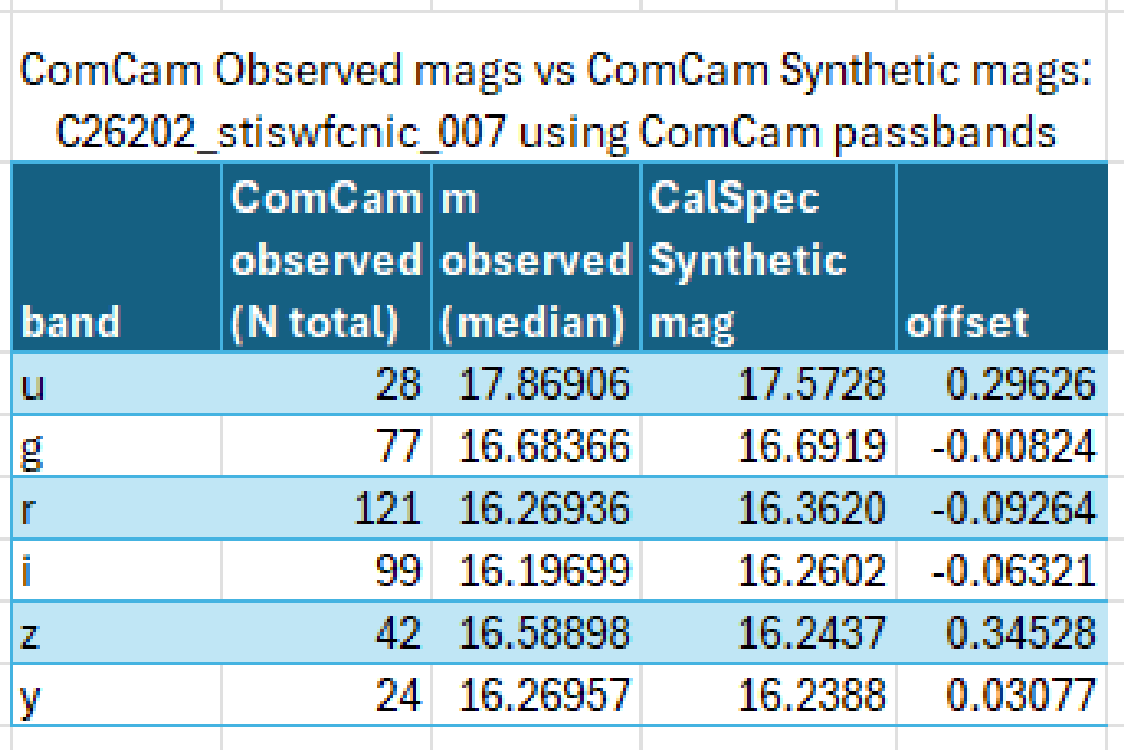

ComCam Observed mags vs ComCam Synthetic mags: C26202_stiswfcnic_007 using ComCam passbands

band	ComCam observed (N total)	m observed (median)	CalSpec Synthetic mag	offset
u	28	17.86906	17.5728	0.29626
g	77	16.68366	16.6919	-0.00824
r	121	16.26936	16.3620	-0.09264
i	99	16.19699	16.2602	-0.06321
z	42	16.58898	16.2437	0.34528
y	24	16.26957	16.2388	0.03077

Figure 56: TBD.

particular interest for galaxy photometry since it was designed to match the SDSS i-band filter.

Visual inspection of a particular group of photogenic galaxies in the HST imaging revealed an excess point source in the ComCam imaging from Nov. 8, which was subsequently found to match the position of an alert issued by several ZTF brokers in early September. We experimented with using the HST image as a template for difference imaging by PSF matching and resampling to ComCam resolution. This can be done relatively successfully on a per-object basis, but unfortunately, the image registration/warping for the HST images is too inconsistent to make it worthwhile on patch scales without re-warping one image or the other.

Besides visual inspection, no other uses of or comparisons to external imaging have yet been demonstrated. DM-47576 (`https://rubinobs.atlassian.net/browse/DM-47576`) has been informally assigned to an in-kind contributor to make loading and displaying HST images more convenient should a need arise.

Joint modelling of space and ground imaging has been demonstrated with MultiProFit in COSMOS with the Subaru Hyper Suprime-Cam (HSC) and HST data on DM-46497 (`https://rubinobs.atlassian.net/browse/DM-46497`) but has not been attempted with ComCam data and is not considered a high priority, in part due to the aforementioned astrometry/warping issues.

7.3.2 Comparison to External Catalogs

DM-47234 (`https://rubinobs.atlassian.net/browse/DM-47234`) compared the tract 5063 20241120 DRP object table galaxy photometry with the latest HLF and Dark Energy Camera Legacy Survey DECaLS (DECaLS, `https://www.legacysurvey.org/decamls/`) catalogs.

Figure 57 shows difference between i-band CModel magnitudes and the HLF HST F775W SourceExtractor magnitudes for both stars and galaxies, using the HST star-galaxy classification. The median difference in both stellar and galaxy photometry is fairly flat across 19<i<25, but also quite large at about 175 mmag for galaxies and 75 mmag for stars. Presuming that the difference in stellar photometry is mainly a calibration issue, the differential between galaxies and stars is still more than a factor of 2 (and still more in quadrature). This could be due to differences in methodology; the HST SourceExtractor-derived magnitudes are more like aperture photometry than a model fit.

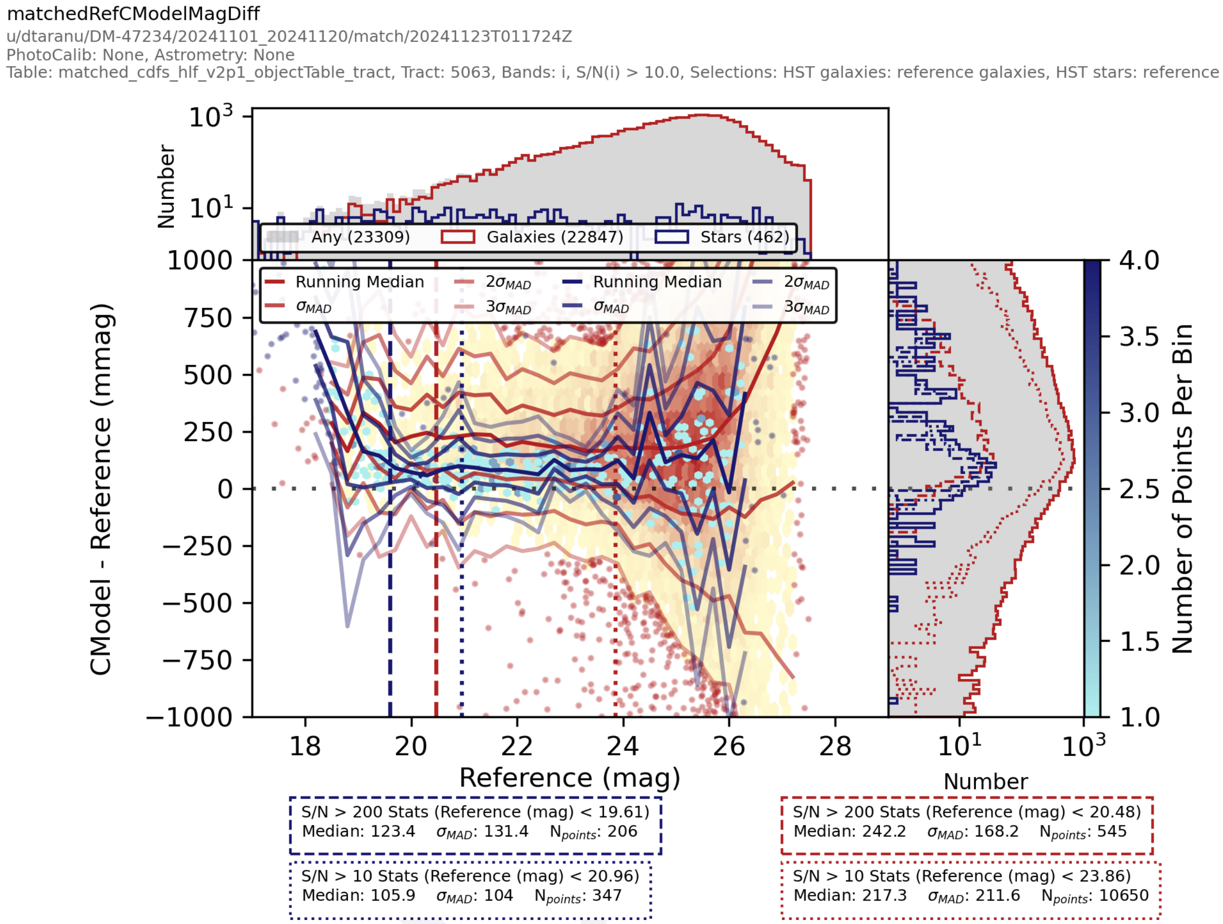

Figure 57: Difference between i-band CModel magnitudes and HST F775W magnitudes in ECDFS.

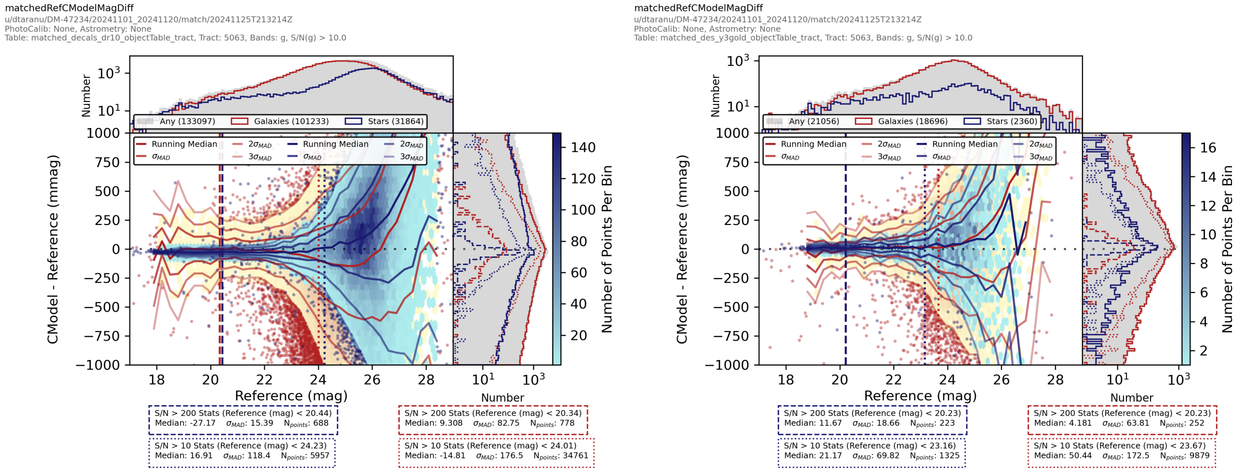

Figure 58: Difference between g-band CModel magnitudes and DECaLS/DES-Y3G catalog values in ECDFS.

Figure 58 shows the difference between g-band CModel magnitudes and measurements from two Dark Energy Survey (DES) DECam (Dark Energy Camera)-based catalogs. The DECaLS (Dark Energy Camera Legacy Survey) DR10 processing is more recent and includes model photometry, selecting the least complicated model required to provide a good fit from a PSF to a single free Sersic fit. The Dark Energy Survey Year 3 Gold (DES-Y3G) sample is an older, shallower dataset, albeit using pipelines more similar to the ComCam/DRP pipelines. The median difference between stellar magnitudes is relatively small but varies with magnitude and between the two catalogs. However, given the difference between filters and that no color term corrections have been applied, both the medians offset and scatter of 10 to 30 mmag are acceptable. Bright ($g < 20.3$) galaxies have median offsets smaller than 10 mmag and scatter of 82 and 64 mmag in DECaLS and DES-Y3G, respectively.

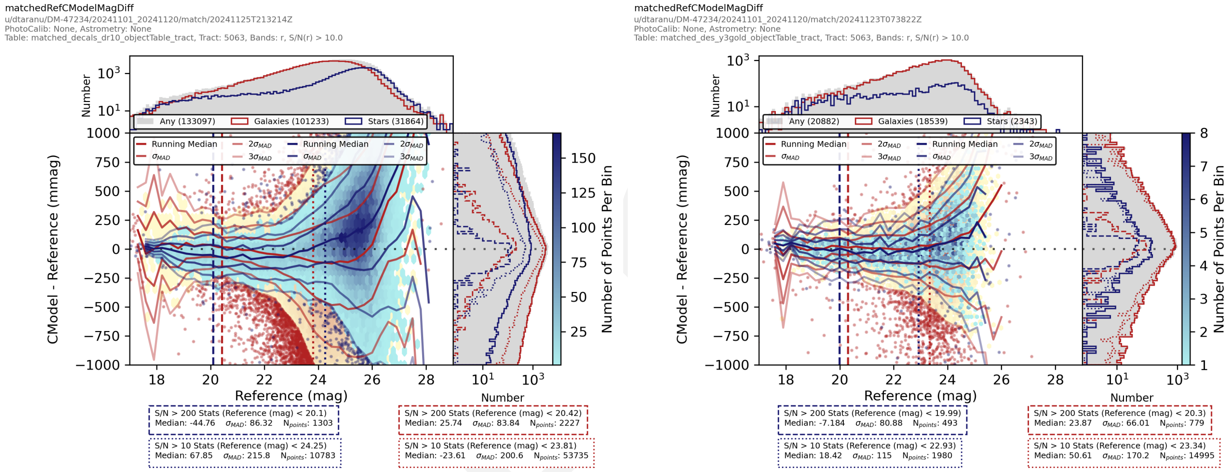

Figure 59: Difference between r-band CModel magnitudes and DECaLS/DES-Y3G catalog values in ECDFS.

Figure 59 shows r-band magnitude difference plots. Here, the median difference for stars are magnitude-dependent in both catalogs, suggesting that color terms are more important. Similarly, the scatter is much larger, at about 80mmag for $r < 20$. However, the magnitude dependence in the median difference is stronger in DECaLS, both for stars and galaxies. Inspection of the $g-r$ versus $r-i$ stellar locus plot (not shown) reveals that DECaLS photometry has a substantial fraction (about 10%) of outliers, some even a full magnitude off the stellar locus. At any rate, the scatter in galaxy magnitudes is not much larger than that for stars (in fact, it is noticeably smaller in DES-Y3G). Additionally, in DES-Y3G, the median magnitude difference is fairly flat for $19 < r < 23$, so despite the numerous differences in hardware and software, the two catalogs are not inconsistent. The i-band photometry in DECaLS shows qualitatively similar but quantitatively worse pathologies and is omitted for brevity.

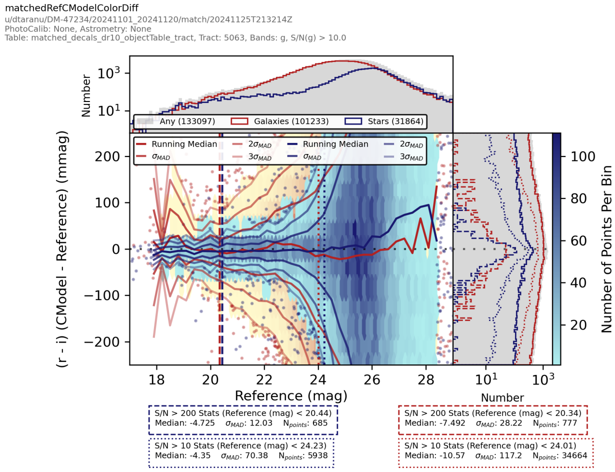

Figure 60: Difference between $r - i$ CModel colors and DECaLS/DES-Y3G catalog values in ECDFS.

The $r - i$ color differences shown in Figure 60 are similar between all three catalogs. The median differences are very small, albeit different in sign between the two pairs of catalogs. The scatter in star color differences is nearly constant to about 22nd magnitude, whereas for galaxies it scales with signal-to-noise to a minimum of about 25mmag at 20th mag (photometry for brighter galaxies is limited by model inadequacy and irregular structure). In short, galaxy colors appear quite consistent between all three catalogs, although how the small differences impact derived quantities like photometric redshifts remains to be seen.

7.3.3 Additional Investigations

Analysis of the accuracy of magnitude and color errors await the implementation of synthetic galaxy injection in DM-47185 (`https://rubinobs.atlassian.net/browse/DM-47185`). Some analysis is possible with matching to reference catalogs; however, besides the problems with the DECaLS photometry, we are not yet taking into account reported errors on reference fluxes (which may themselves be underestimated).

Besides single-band/forced CModel photometry, MultiProFit multi-band (gri) single Sersic fits have been run on a single patch in tract 5063 on DM-47526 (`https://rubinobs.atlassian.net/browse/DM-47526`) but have yet to be analyzed. Other algorithms like aperture, GaAP and Kron magnitudes/colors have yet to be compared.

7.3.4 Conclusions

Galaxy photometry in ECDFS appears consistent with at least two different catalogs covering the same field (one space based) and the differences identified in a third (DECaLS) appear to be peculiar to that catalog, not our own processing. This is not to say that the galaxy photometry is optimal, as hardware and software differences make it difficult to quantify expected differences. Comparisons to external data should be more illuminating once we have coadds in the COSMOS field and can compare to HSC imaging with the same pipeline versions.

8 Low Surface Brightness Sources and Scattered Light

The low-surface-brightness science team has been actively involved in investigating the ComCam imaging. Efforts in this area have largely broken down along two avenues.

Visual Inspection: Several members of the team have been actively engaged in image inspection with a specific eye on low-surface-brightness features. Several items that have arisen during this inspection.

- **Ghosts:** Ghosting, internal reflections of the light from astronomical objects off of multiple reflecting surfaces within the camera (e.g., the detectors, lenses, and filter), is a well known contaminant for low-surface-brightness science. Ghosts were first identified in images taken on the first night of ComCam observing. Ghost patterns were associated to stars both on, and slightly off, the ComCam field-of-view. Analysis from the batoid ray tracing code could qualitatively reproduce the ghost patterns (see below for more details).
- **Baffling:** A prominent stray light feature was noticed as concentric circles of varying intensity often situated in the corner of the ComCam field of view. Initial incidences of this stray light were traced back to a light on the dome crane (see below); however, this pattern continues to be seen on subsequent nights. Members of the camera crew note that there is no baffle system installed upstream of the ComCam optics, and we expect stray light to be much reduced with LSSTCam.
- **Dome Lights:** Several lights inside and around the dome have been identified and mitigated (one particularly impactful light source was on . Pinhole images are a valuable tool

for identifying these light sources, and several were identified in recent pinhole imaging. As operations becomes more routine, it is expected that the incidence of artificial light in the dome will decrease.

- **Sky over-subtraction:** Correct subtraction of the sky background around large, bright astronomical objects (e.g., nearby galaxies, nebulae, galaxy clusters, etc.) while making accurate measurements for faint objects in the frame is a challenging task. The LSB group has been tracking instances of astronomical objects that have been observed by ComCam and are likely to suffer from background subtraction issues.
- **Artificial Satellites:** The low-surface-brightness, out-of-focus tails of bright artificial satellites may contribute structured low-surface-brightness features in stacks and coadds. While the topic of artificial satellites is largely covered in Section 9.1, the LSB group is interested in tracking particularly prominent examples.

The group is tracking visually identified instances of many of these features in ComCam imaging.

Quantitative Ghost Investigation: The 'batoid' ray tracing toolkit has the ability to predict the locations and relative intensities of these ghosts. Based on early qualitative comparisons, batoid appears to be doing a good job at predicting the patterns of ghosts observed in ComCam imaging for stars located both on and slightly off the focal plane. A more quantitative evaluation between batoid and the ComCam imaging is now being developed to assess the precision and accuracy of the batoid model when it comes to predicting the location, morphology, and intensity of ghosts. Gaia is being used to identify bright stars that should contribute prominent ghosts. These stars are fed into batoid and the output ghost patterns are scaled by the flux of each input star as measured by Gaia. Circular templates for the ghosts are being generated by running batoid on each scattering surface individually and applying Canny edge detection and a circular Hough transform to determine to position and size of each ghost. These circular ghost templates will be compared to the observed data, and eventually fit to the intensity of the observed ghosts to verify/refine the reflectivity coefficients that batoid uses for each camera surface. While the ghosting in LSSTCam will be different from that in ComCam, the tools developed for this analysis should be generalizable.

Future Endeavors

The team hopes to have the chance to collect and investigated on- and off-axis dithered bright star exposures to further quantify ghosting and scattered light. The team is actively investigating metrics to characterize the variance in the sky background modeling. The team is investigating sky background fitting techniques developed on DECam. DECam calibrations have been acquired and testing of these algorithms on DECam data processed with the LSST Science Pipelines is being developed. We hope to apply the quantitative LSB tools being developed on precursor data to the ComCam data.

8.1 Crowded Stellar Fields

8.1.1 Observations taken to date

Five visits of the globular cluster 47 Tuc were taken during AOS testing:

- 2024111600136
- 2024111600139
- 2024111600142
- 2024111600145
- 2024111600148

Links are to focal plane images of each visit.

This field is a good target for testing the crowded field pipeline, though these observations do not have a sufficiently good PSF for analysis. Zoomed in, the PSF of the stars in the cluster are a variety of out-of-focus donuts.

Deblending failed on these images, and we are waiting on new data under better conditions to test deblending and image differencing.

Other fields observed so far have not exceeded $25\,000$ sources per square degree, which is insufficient for testing the crowded field pipelines.

8.1.2 Commissioning data needed

The ideal test data would be observations with densities in the $75\,000 - 100\,000$ sources per square degree range. Several fields have been proposed:

1. **Extragalactic Deep Field:** Extended Chandra Deep Field-South @ (ra, dec) = (53.125, -28.1)
2. **Extragalactic Deep Field:** Euclid Deep Field South @ (ra, dec) = (59.1004, -48.73)
3. **Ecliptic Field:** Rubin_SV_38_7 @ (ra, dec) = (37.9, 7.0)
4. **High Stellar Density:** Fornax Dwarf Spheroidal Galaxy @ (ra, dec) = (40.00, -34.45)
5. **High Stellar Density:** Rubin_SV_095_-25 @ (ra, dec) = (95.0, -25.0)

8.1.3 Development work needed

While difference images can usually rely on having isolated diaSources, we expect to have many blended footprints in sufficiently crowded fields.

We have implemented deblending of blends of purely positive or purely negative peaks (DM-44319), but blends of mixed peaks require new development. This work is ticketed on DM-44416, but not yet started or planned.

9 The Variable Sky

9.1 Difference Image Analysis: Transience and Variable Objects

9.1.1 DIA Status

As we have started to obtain repeated science-quality images of some fields, we have begun to build coadded templates as part of the regular weekly cumulative Data Release Processings. These mini-DRPs also include difference image analysis (DIA) of their constituent exposures. Using the DRP-produced templates, we have also obtained near-real-time difference images in Prompt Processing for a few exposures. We have not yet had the opportunity to begin tuning template generation, difference imaging, or Real/Bogus characterization of these data, so the report below provides an initial rough characterization of DIA performance.

9.1.2 ML Reliability and Artifact Rates

We ran a convolutional neural network on 51×51 difference, science, and template cutouts for 912k DIASources identified in the `w_2024_47` data release processing. This processing primarily includes data from extragalactic deep fields. These DiaSources were obtained from 4252 detector-visit images, implying an average of 21 DIASources per detector or about four thousand per equivalent full LSST focal plane. This is somewhat less than the ten thousand DIASources expected per visit and may reflect lower sensitivity due to ongoing image quality refinement and early templates.

The CNN was trained on simulated DC2 images with additional point source injection, so caution is needed when interpreting the values returned by this classifier on ComCam data. Nevertheless, Figure 61 shows a clear separation in reliability scores and would imply roughly a 3:1 bogus:real ratio if taken at face value. These values will be confirmed with manual inspection. We plan to train a purpose-built classifier on larger samples of labeled ComCam data.

9.2 Difference imaging QA

A difference imaging afterburner is run manually on Prompt Processing output to generate diagnostic plots, such as 62. From 62 we see the centroid of the PSF matching kernel sampled across one detector, which reveals a systematic offset between the science and template images. A similar offset is seen across the rest of the detectors for this visit, and in other visits. The images comprising the template used the same astrometric reference catalog as the science image in this case, but the template was constructed with the calibrate+characterizeImage pipeline while the science image was processed with calibrateImage. These are not included in the Prompt Processing payload to save critical time during observing.

The distribution of sources detected on the difference image reveals some detector-level effects that are not fully accounted for. Binning the locations of the diaSources in 1-D in 63 by their x- and y-values reveals systematic overdensities of detections at the amplifier bound-

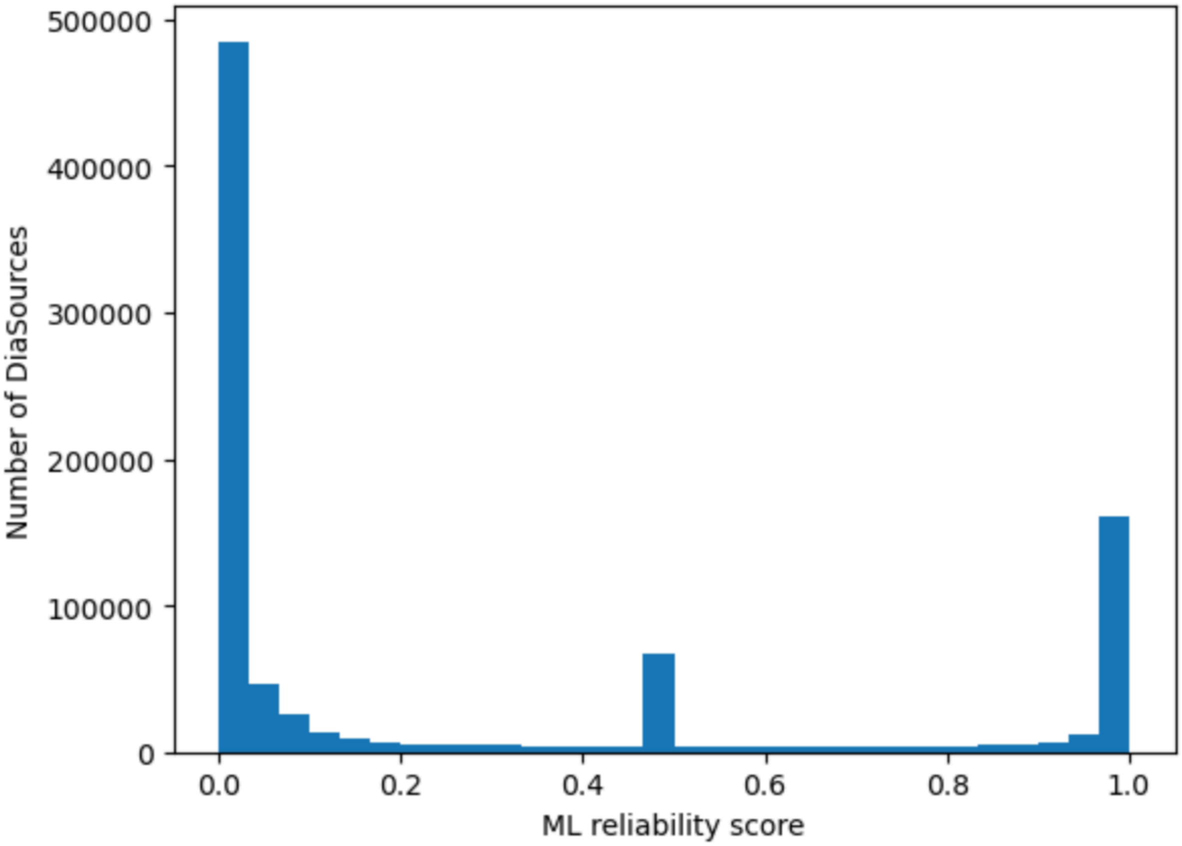

Figure 61: Histogram of machine-learned reliability scores computed on ComCam difference images.

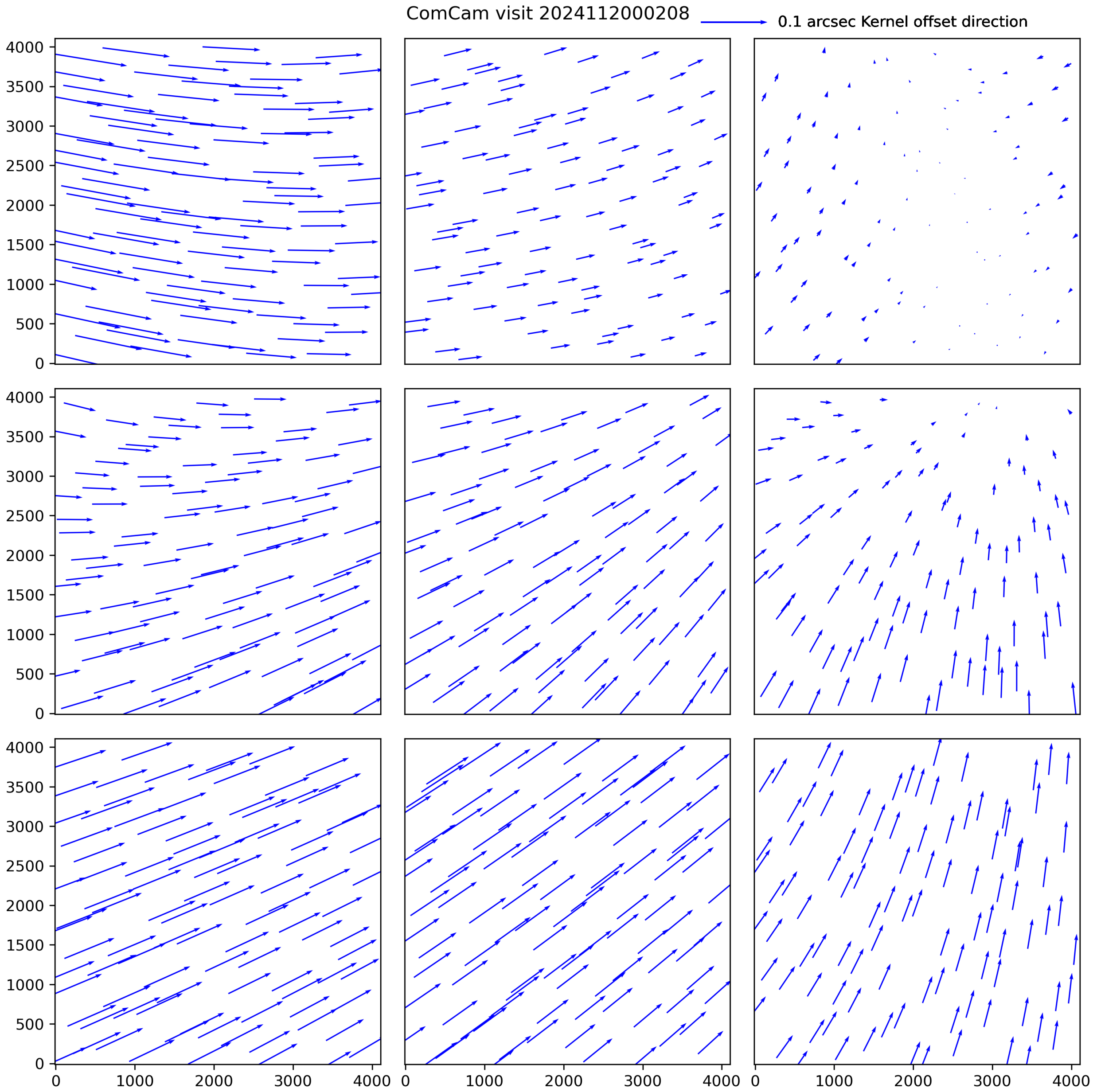

Figure 62: Quiver plot of the implied offset between the science and template images, calculated from the centroid of the PSF matching kernel. Note that the scale differs between the different panels, but that the overall pattern appears coherent over the focal plane, although each CCD was solved independently.

aries in x (but not in y). Additional overdensities seen in y-band may be from the residual phosphorescent wax reported to be left on some chips beneath the AR coating.

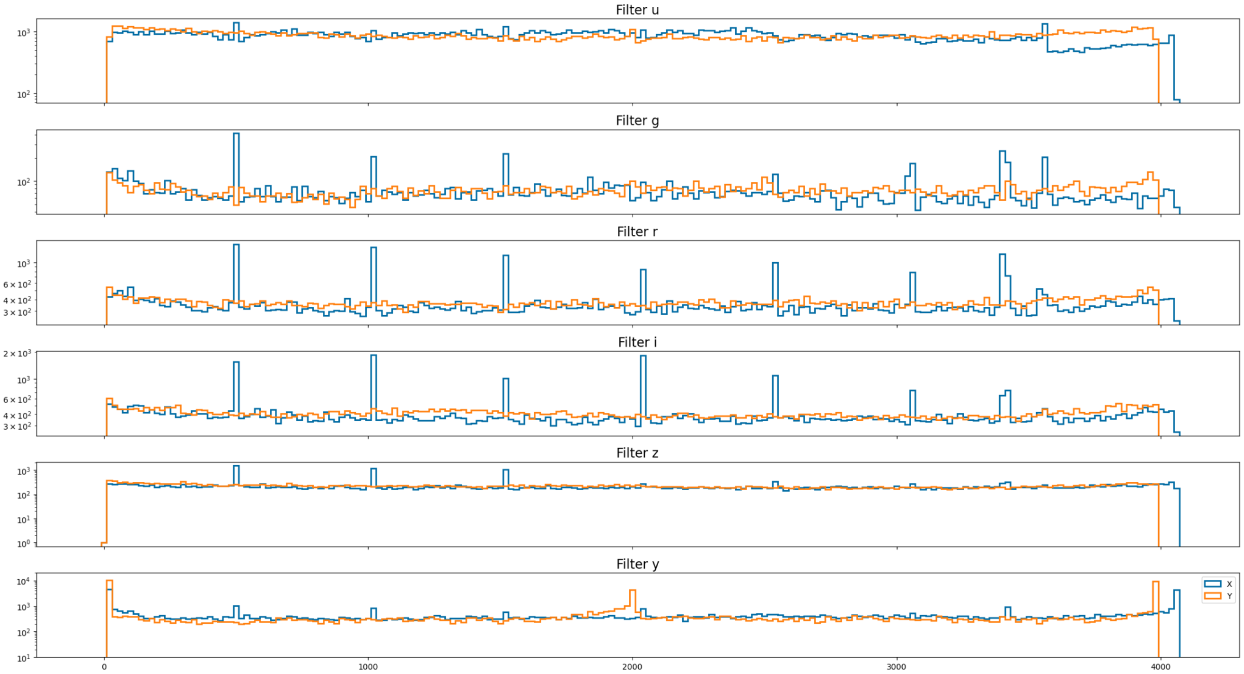

Figure 63: Binning the locations of the diaSources in 1-D by their x- and y-values reveals systematic overdensities of detections at the amplifier boundaries in x (but not in y).

9.3 Satellite Streaks

As orbital space becomes increasingly crowded, we expect to see many bright streaks, flares, and glints due to satellites and other reflective human-made objects orbiting the Earth. The majority of the population is in low-Earth orbit (LEO). For a review of the current status and likely impacts to LSST, please see `ls.st/satcon`.

As expected, many ComCam detector-visit images clearly show streaks. Visual inspection of nearly all ComCam images to date are being recorded on a best-effort basis in a Confluence Database dubbed “ComCam Satellite Spotter,” and as of 2024 Nov 25 there are over 500 rows. The simple schema has one row per visit (if a streak crosses multiple detectors — which it often does — this is indicated in the “detector” column). In general, the morphology of streaks falls into one of these categories:

- Straight bright linear feature, typically at least 20 pixels wide, that crosses one or more detectors and goes off the edge (typical of most LEO satellites, such as Starlink)

- Shorter version of the above, with clear start and/or endpoints, which usually indicates the object imaged is located at a higher-than-LEO orbital altitude (and/or the exposure integration time was unusually short)
- Intermittent linear feature, i.e., a dashed line, due to different parts of the satellite having different reflective properties
- A flare or glint brightening event that fades in and out along a linear trajectory, either isolated or as part of a longer streak
- Actually a bright star diffraction spike
- Actually a cosmic ray that was not repaired
- Variation of any of the above but in out-of-focus donut form (interestingly, depending on altitude, certain streaks may appear either in- or out-of-focus when stars appear as donuts)

Thanks to ComCam's relatively small field of view and the satellite population being as small as it ever will be during Rubin Commissioning and Operations, we have not yet seen an overwhelmingly bright satellite (e.g., BlueWalker 3 or one of the BlueBirds, all operated by AST SpaceMobile). Only a couple instances have streaks bright enough to induce visually-obvious crosstalk "secondary streaks;" the majority of streaks are relatively faint and the only portion of the image impacted are regions overlapping with the streak itself on the sky. Reliably determining streak width is an ongoing challenge, as it is not a delta function, and some of the brighter streaks do have notably extended stray light profile wings.

We note the Science Pipelines' algorithmic approach to identifying linear streak features (see `https://dmtn-197.lsst.io`) uses the detected mask plane and not the image array (pixel values) for efficiency. To more effectively detect faint streaks in difference images we have recently implemented a binning scheme designed to be sensitive to linear features that fall below the detection threshold.

9.3.1 Mitigating streaks in DRP

In most situations, the usual outlier clipping done during coadd assembly with the CompareWarp algorithm excludes streaks from coadds. The coadds where streaks remain all tend to have very few input images, so the streak was not able to be flagged and excluded as an outlier. Work is underway to assess the performance of detecting streaks via the kernel Hough transform in ComCam on top of the standard outlier clipping.

9.3.2 Mitigating streaks in AP

Work is underway to detect and masking streaks and glints in difference images. ComCam observations are an important data set for testing how well this works in various situations. A more detailed report will be available in the coming weeks. The efforts described here are distinct from work to identify long trailed sources and cross-check with an external satellite catalog.

9.4 Fake Source Injection for DIA

9.4.1 Selection of a data subset

In this subsection we select a portion of the observations processed by the DRP pipelines that include DIA, and run some simple analysis checks on the data contents. There are many fields being observed with LSSTComCam that span a large portion of the southern hemisphere accessible sky at this time of year (fall 2024).

From these, we make a selection, choosing a very well covered field in all bandpasses. In Fig.64 we show the full coverage of LSSTComCam up to current date.

In Fig 65 we apply a first cut on the observations, to narrow our visit list to a total of 24 visits. This cut involves a zenith distance of less than 45 degrees, as well as some technical parameters, derived from the nominal DRP DIA performance (ratio of PSF between template and science, as well as Kernel basis condition number).

We create a catalog of fakes for this sample of visits, by creating position and magnitudes of the synthetic sources to be injected. In Fig 66 we show the fake distribution per chip in our selection. We use sources that are possibly extended, and choose the fake location in its sourroundings. The magnitudes are chosen so they are within 1.5 magnitudes of the selected source host.

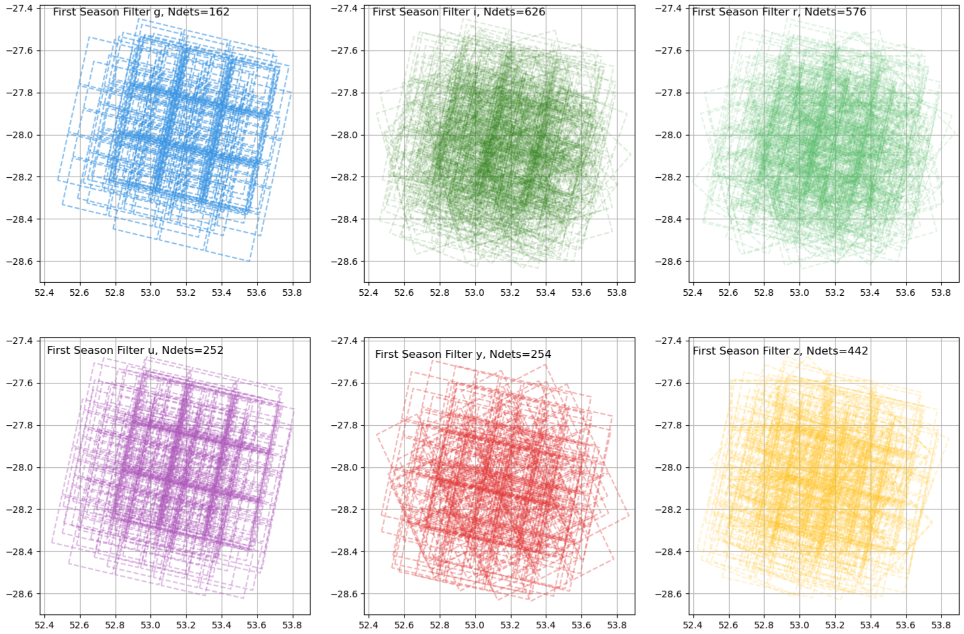

Figure 64: The full LSSTComCam set of observations overlapping the chosen field and with elevation > 45 above the horizon.

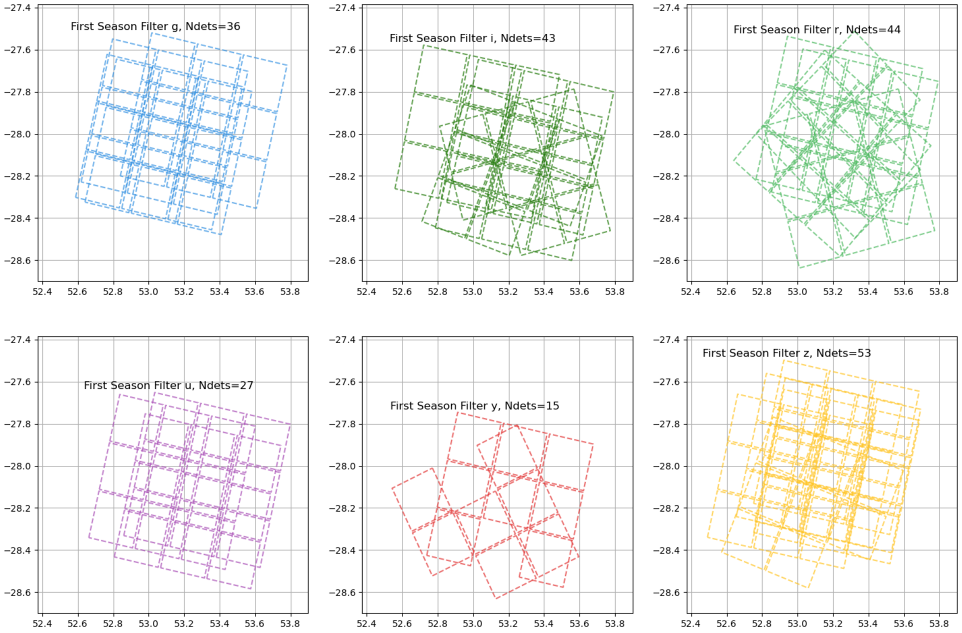

Figure 65: The selection of CCDs for fake injection processing.

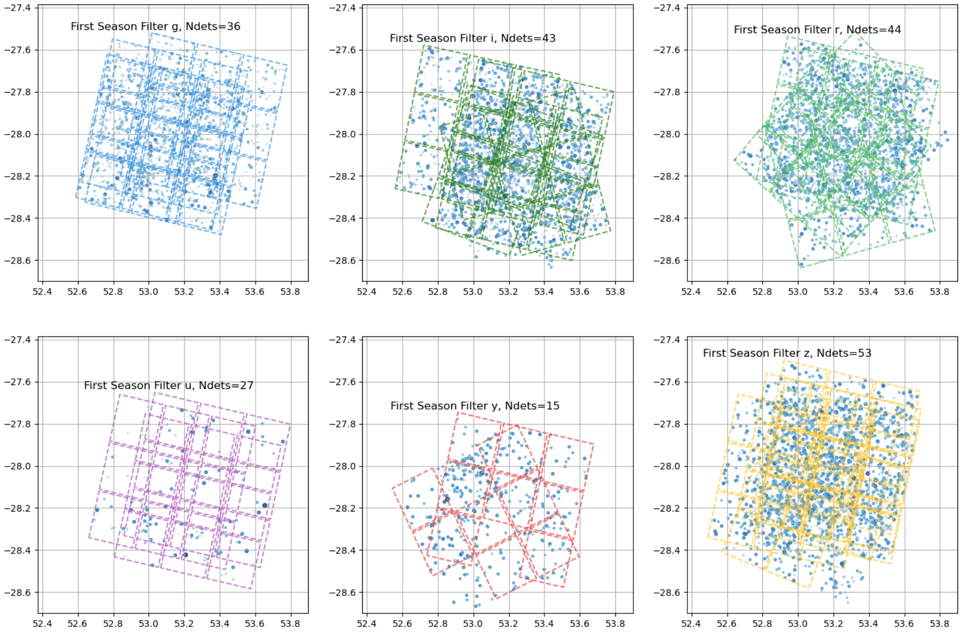

Figure 66: The fake position distribution in sky and in the CCDs footprint per bandpass.

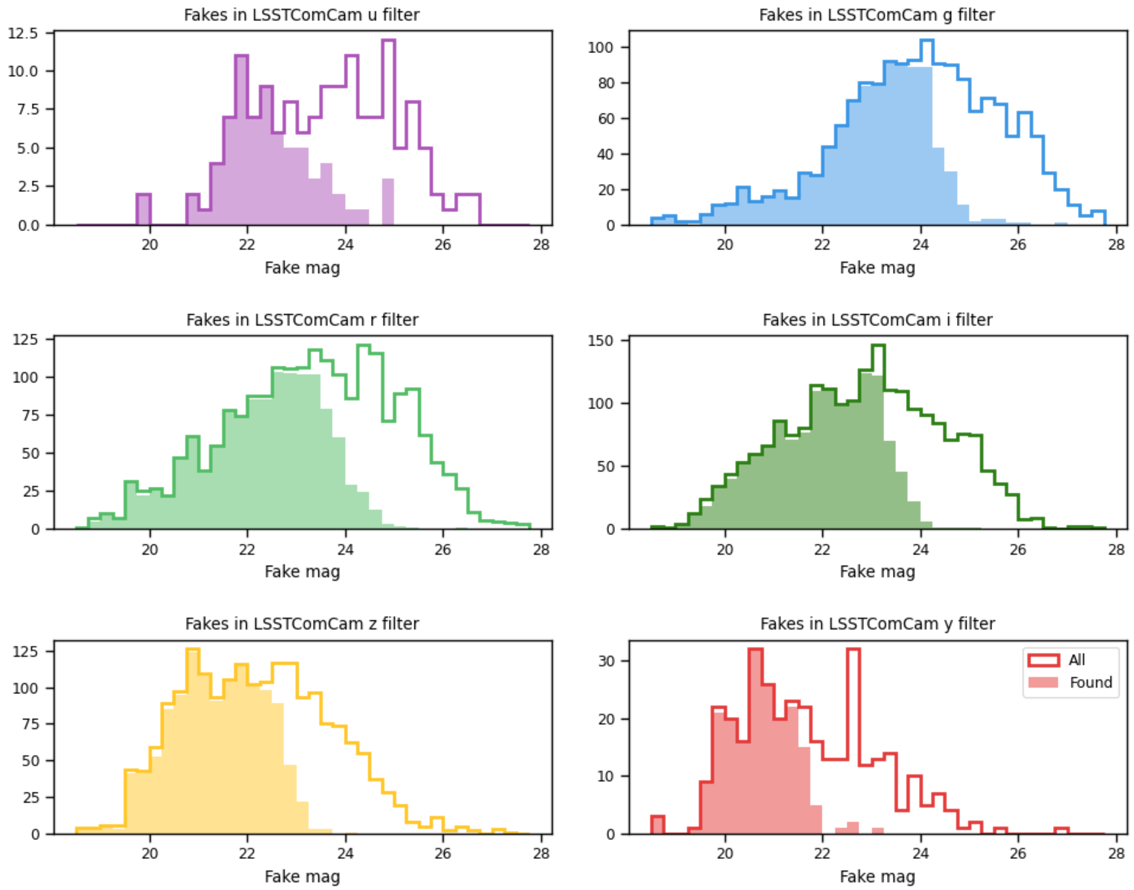

Figure 67: The distribution of magnitudes per bandpass for all the injected fakes (solid lines), and in shaded region the distribution of magnitudes of the fakes detected by the AP pipeline.

We run Alert Production pipeline with a set of additional tasks that handle fake injection on the *initial_pvi* images, and then the book-keeping tasks of fake catalog matching to diaSources as well as forced photometry for SNR estimation.

We then, can compile useful statistics about the fake source recovery, that informs us about DIA algorithm performance, as well as detection and measurement algorithm performance.

For this, we cross-match the position of our candidate detections, or *diaSources* with the positions of the synthetic sources, using a tolerance of $0.5''$ (roughly 2.5px).

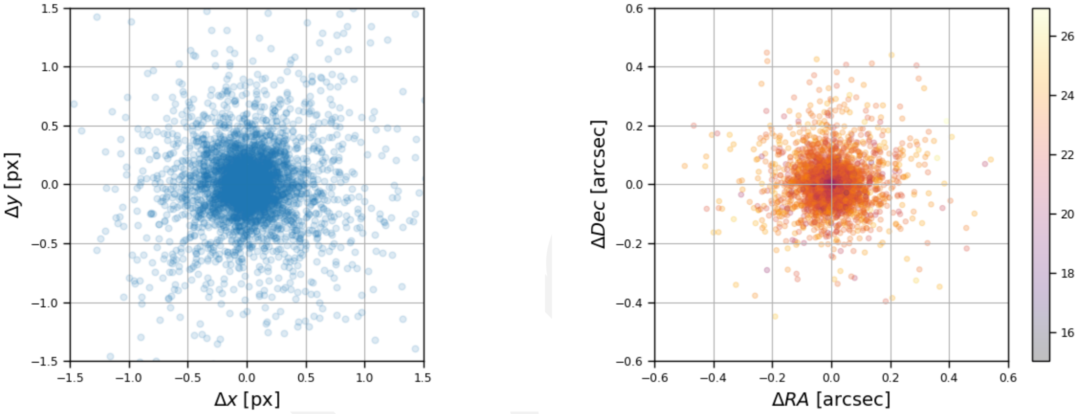

Figure 68: The scatter of the coordinate centroid recovery of the fakes. In the left we have the scatter around the true centroid in pixel coordinates, and in the right the scatter around the true center of fakes in sky coordinates (and in units of arc-seconds), wit the grid matching the pixel grid by means of the platescale. Also, we include the brightness in colormap.

Those fakes that found a match are called ”found fake” and objects that had no match we refer as ”lost” or ”missed” fakes. The rate of found to existing fakes is our recovery rate, Recall or Efficiency of detection.

9.5 Difference Image Analysis: Solar System Objects

9.5.1 Difference Image Association

So far, difference images have been made only of two fields very far from the ecliptic, where solar system objects are very rare. Known-object association ran, but (correctly) associated no difference image sources to known objects.

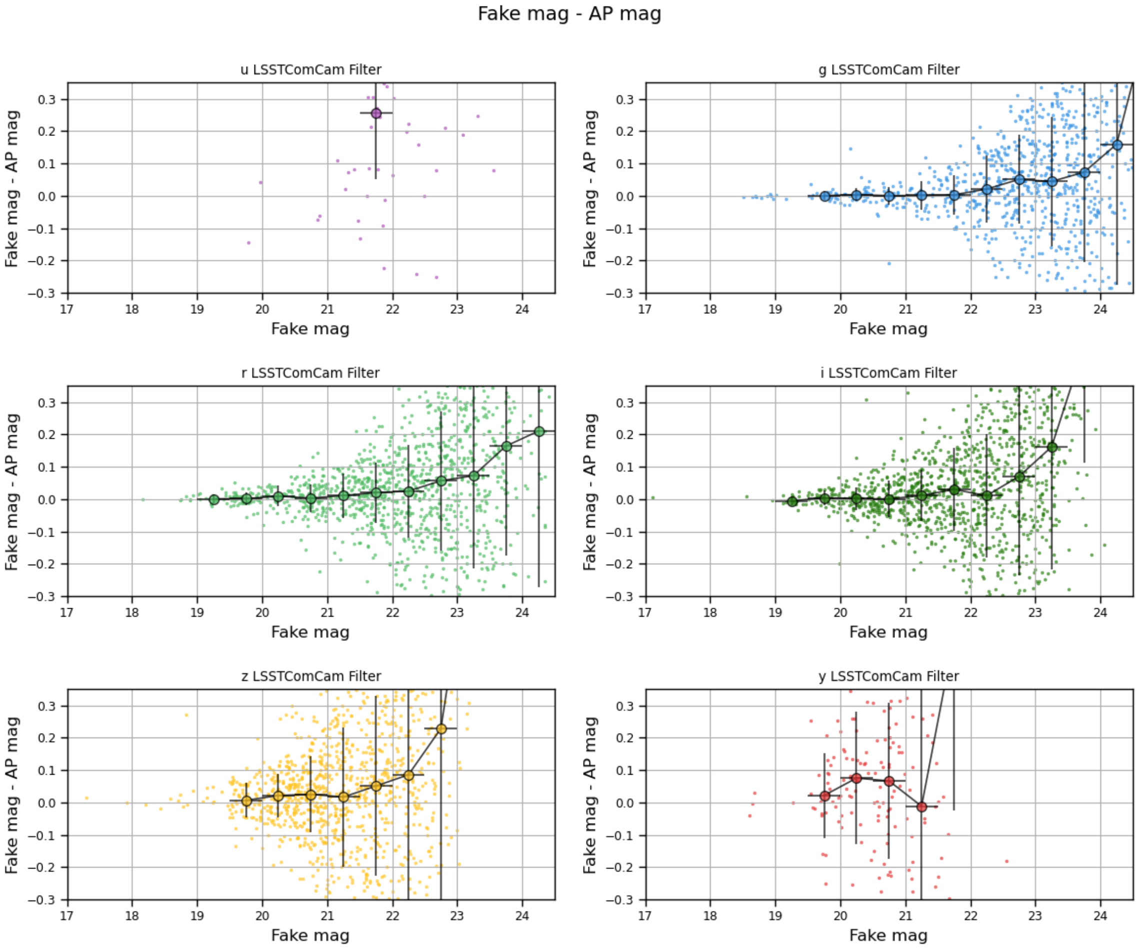

Figure 69: The recovered Aperture magnitude residual per filter for all the found fake sample, as a function of their true magnitude.

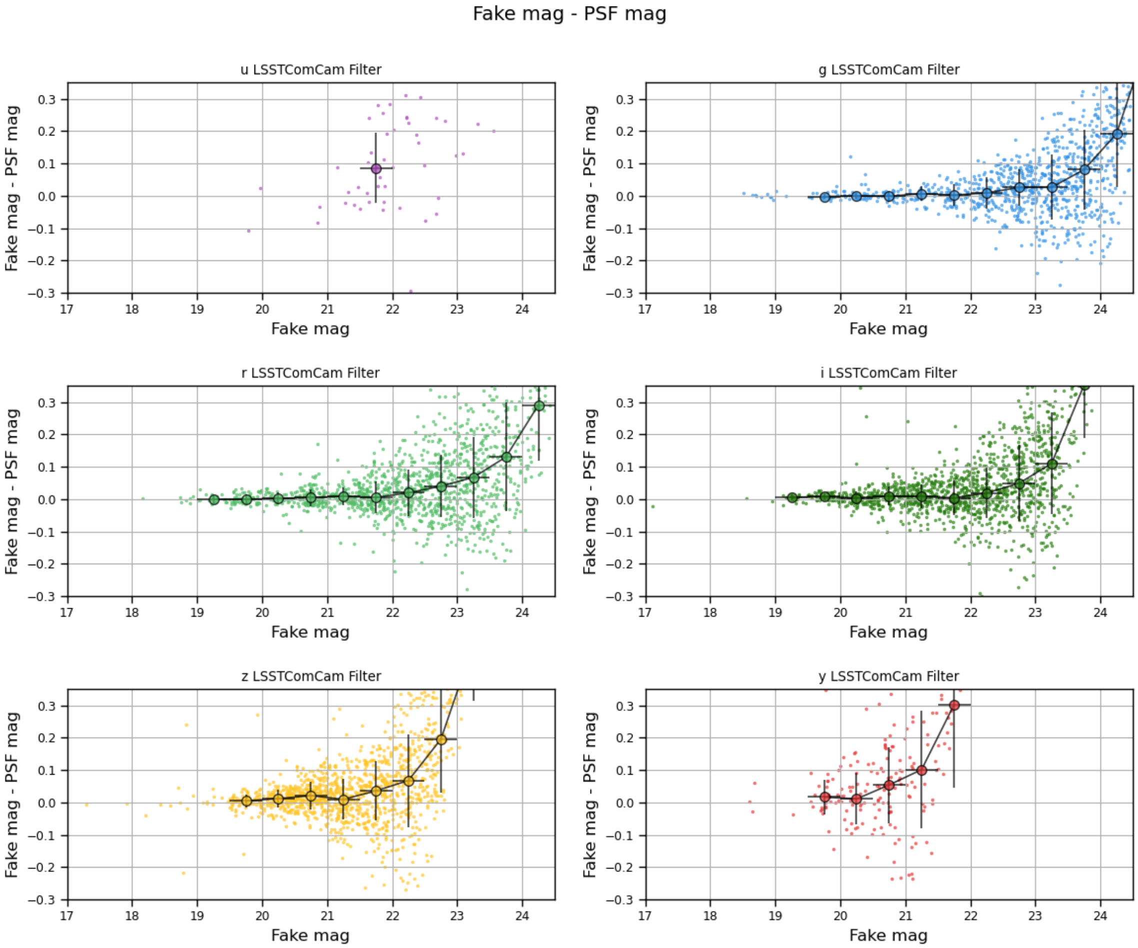

Figure 70: The residual of PSF magnitude measurement for found fakes, as function of their true magnitude.

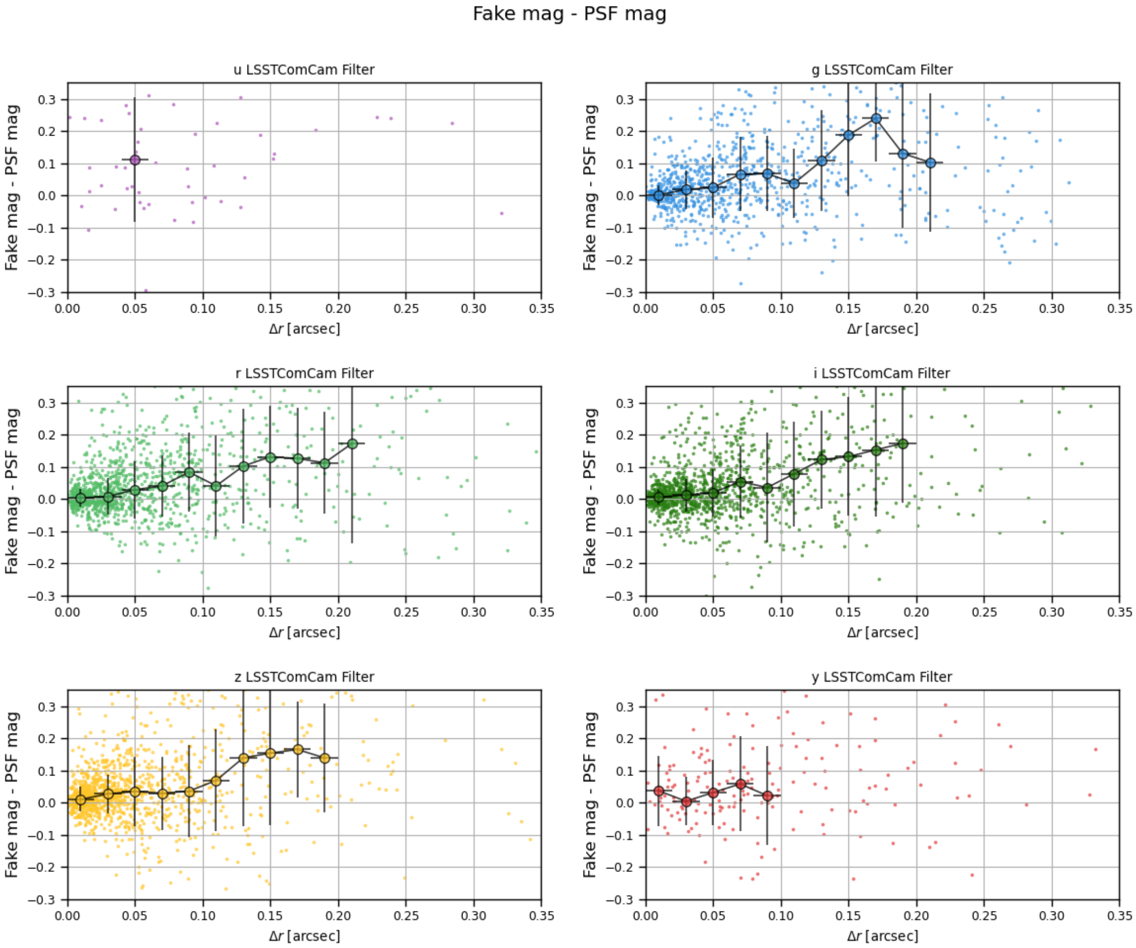

Figure 71: The PSF magnitude residual for the found fakes as function of their matching distance (in [arcsec]).

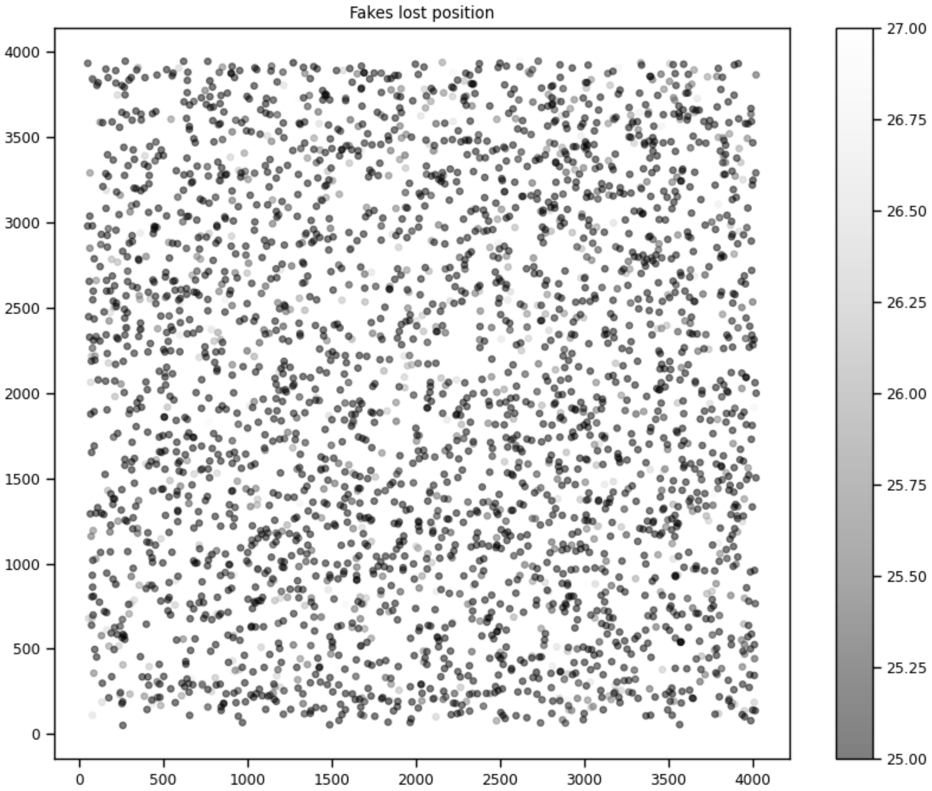

Figure 72: The scatter map of the lost sources in the detector coordinates. In gray scale in the colorbar we show the object magnitudes.

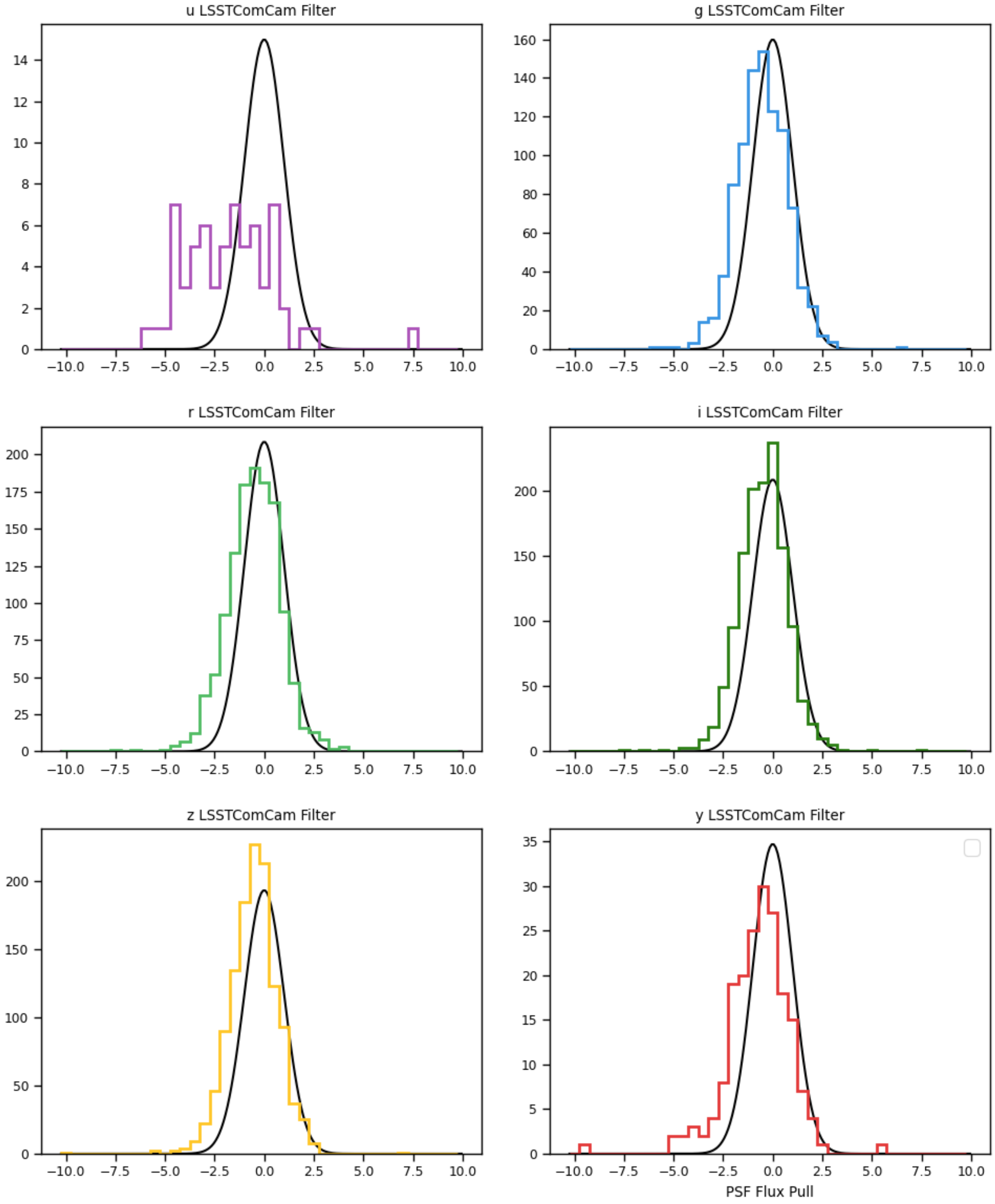

Figure 73: The flux pull distribution for all the found fakes, in each filter bandpass. A zero mean, unit dispersion Gaussian distribution function is also included for reference.

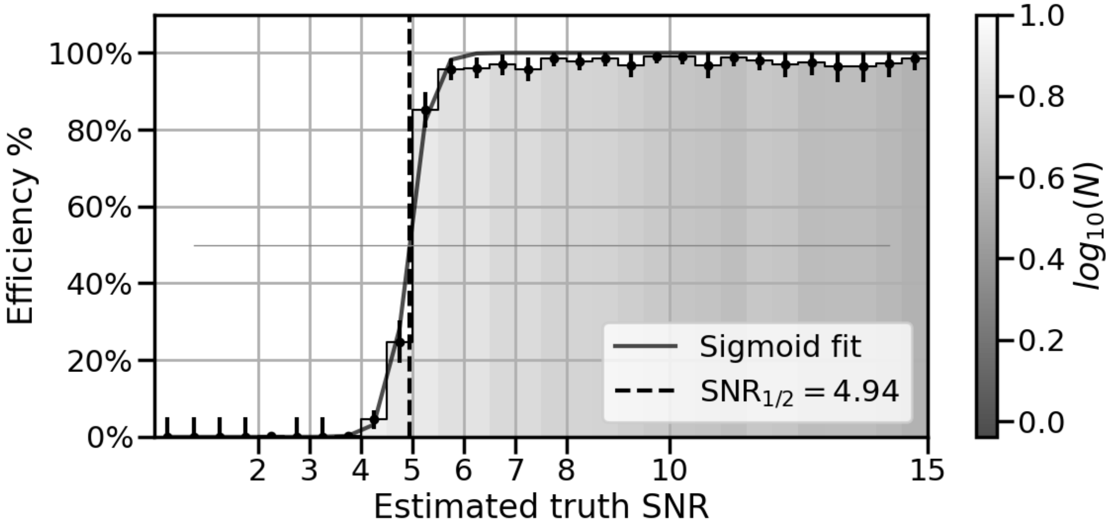

Figure 74: The detection efficiency as function of the PSF estimated S/N ratio of the fake sources. The SNR 1/2 parameter is also included in dashed lines, and represents the 50% efficiency S/N threshold value (lower is better).

9.5.2 Difference Image Linking

We tested tracklet creation with `make_tracklets`, the first stage of *unknown* asteroid discovery for LSST, on the two available sets of difference images, though asteroids were unlikely to be found in these regions of the sky. The first field included 10 visits with on average 840 sources per visit, while the second had 12 visits with on average 430 sources. These numbers are encouragingly low, indicating that Rubin difference images are fairly clean. For this test case, we set `make_tracklets` to require a minimum of 5 sources per tracklet, but it produced only 9 total tracklets, all with fewer than 5 detections, inconsistent photometry, and relatively high Great Circle residual (GCR)[2]. Manual examination of image cutouts confirmed that the tracklets were entirely composed of spurious sources.

More interesting is the nature of the spurious sources that made up the tracklets. All were associated with bright stars, including diffraction rays, incompletely subtracted scattered light halos, and subtraction residuals near the PSF core. This is very good news, as all of these types of spurious detections can be eliminated through pre-screening of the source catalogs.

---

[2] Defined only for tracklets with more than two points, the GCR is the RMS residual relative to the best-fit trajectory that follows a Great Circle on the sky at constant angular velocity. Real asteroids, unless they are very near the Earth, produce tracklets with very low intrinsic GCR: hence, elevated GCR usually indicates a spurious tracklet.

Early data suggests that LSST will produce fairly clean difference image source catalogs for the asteroid discovery pipeline and that pre-screening can make them even cleaner. This is important, because simulations indicate the LSST specifications for the minimum discoverable asteroid (six detections, making up three two-point tracklets, within a two-week time span) are on the edge of what is statistically possible without an unacceptable false positive rate. Hence, it is vitally important for the difference image source catalogs to be as clean as possible. There's a lot of work to do, but the early indications have us cautiously optimistic.

9.6 Single-epoch Image Analysis: Solar System Objects

9.6.1 Single-epoch Association

Ten images taken in one field on 2024-11-06 and ten each in four fields on 2024-11-23 were close enough to the ecliptic for possible asteroid association. Across the five fields, we associated 828 sources with known asteroids, including 128 unique objects. The 24 objects associated on 2024-11-06 are shown in Figure 75. We compared the sources' astrometry to our ephemerides, as shown in Figure 76. We find very low bias: the median unsigned error is 13 mas, indicating that there are no major errors in either timing or astrometry. We also find low variance, with standard deviationsin RA and Dec of 41 and 44 mas respectively, though in an especially bright and therefore low-variance sample of known objects. Evaluating the precision of asteroid association tests the whole software chain, including the astrometry pipeline, ephemerides computation, and image timing. In sum, the total error contributed by these different systems appears to be low enough for high-confidence association of known asteroids.

9.6.2 Single-epoch Linking

We attempted to link asteroids in single-epoch source catalogs including the fields in section 9.6.1 relatively near the ecliptic. In contrast to the difference images averaging 430-840 sources per visit, single-epoch images contained 11,000-23,000 sources per visit, mostly stars. The first reasonable test involved ten images taken on November 6. From an average of 16,000 sources per visit, `make_tracklets` found 3,068 tracklets with at least five points. While most of these were unquestionably spurious, nine of them were ten-point tracklets (i.e. detected in *every one* of the ten visits), showed excellent photometric consistency, and relatively low GCR: very likely real asteroids.

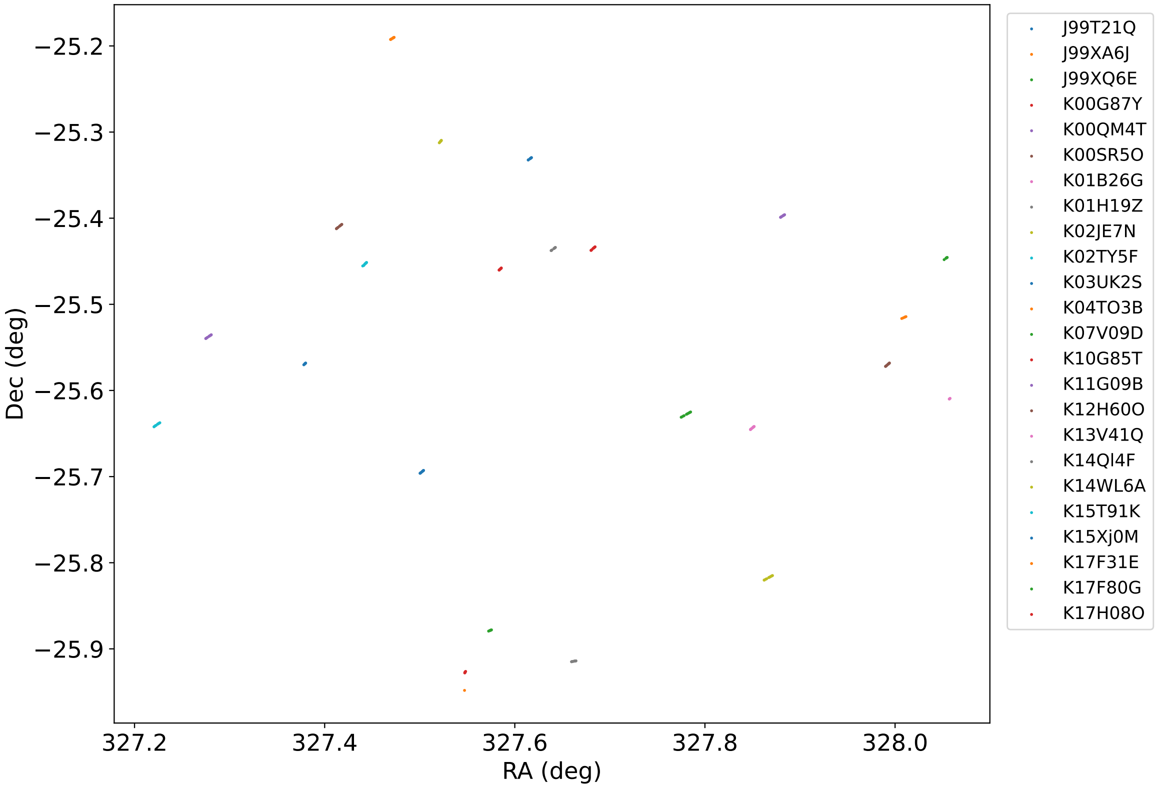

Figure 75: Positions of the 24 asteroids associated in images from 2024-11-06.

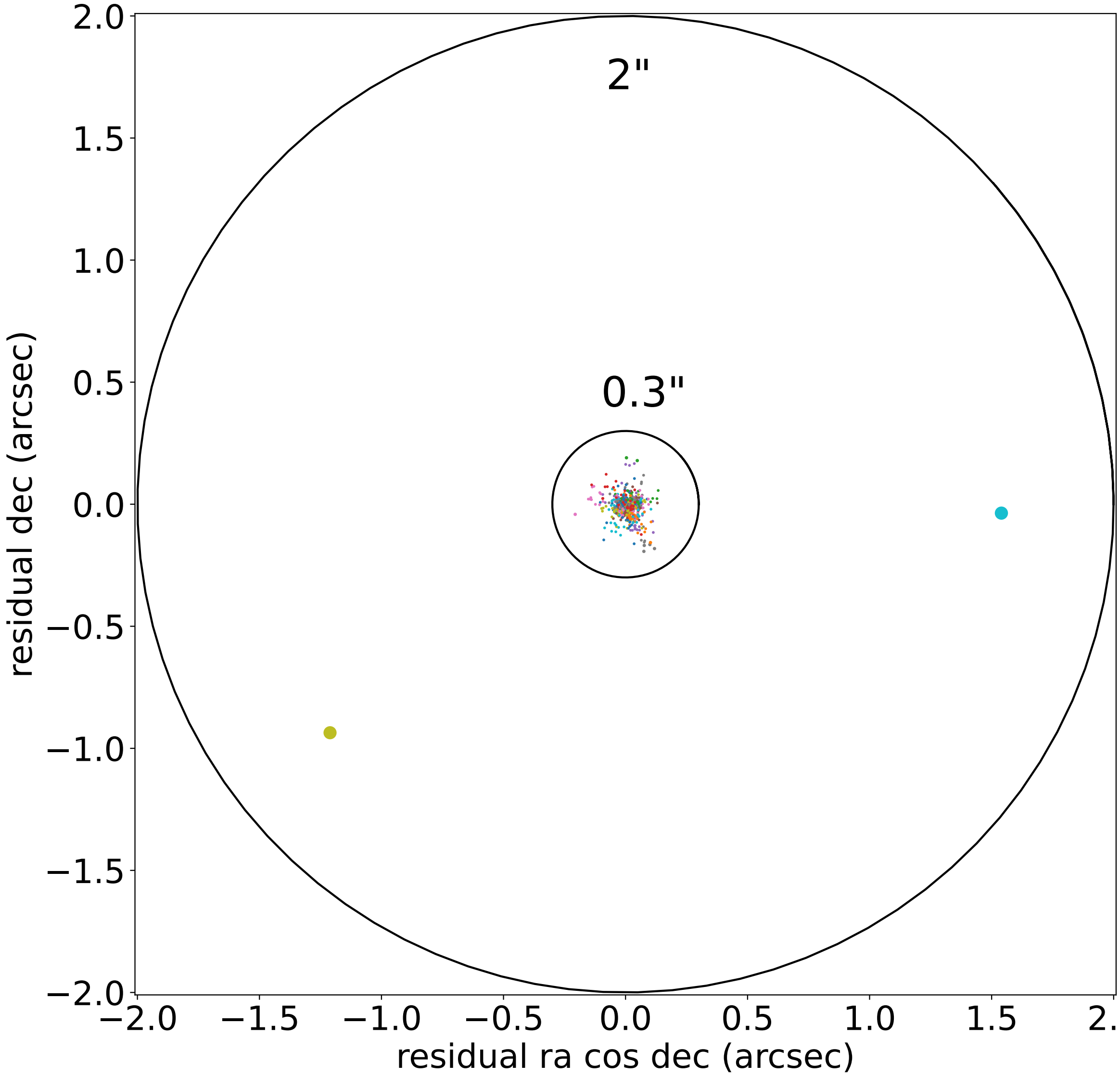

Figure 76: Astrometric residuals of the 633 sources associated to 104 asteroids on 2024-11-23. All but two sources have residuals under 0.3 arcseconds, while the two outliers have been identified by visual inspection as mis-associations of undetected asteroids.

We selected the ten-point tracklet with the very lowest GCR (0.046 arcsec) and checked it against known asteroid ephemerides, obtaining a match to the main belt asteroid **(193300) 2000 SO275**, a 20th magnitude object with a very well-constrained orbit. **(193300) 2000 SO275** was the *very first asteroid confirmed to have been detected with the Simonyi Survey Telescope.* We evaluated LSST's astrometric precision by comparing these detections to predicted positions from JPL. The RMS astrometric offset was found to be 29 milli-arcseconds (mas), with a systematic bias (the median observed-calculated residual) of only 14 mas in RA and 3 mas in Dec. These errors are statistically consistent with zero, as expected. We also probed for timing errors, which would produce a positional offset in the direction of motion. Dividing the along-track component of the astrometric offsets by the measured angular velocity, we found a median time offset of 0.3 seconds — consistent with zero at the 0.5σ level.

All of the other ten-point tracklets were found to correspond to known asteroids, as did 12 additional tracklets with 7–9 points, consistent photometry, and relatively low GCR. In total, 21 real asteroids were found by `make_tracklets` in this single field, demonstrating its ability to discover asteroids in LSST catalogs.

10 Data Production

11 Survey Performance

Understanding and predicting survey performance includes modeling the likely input telemetry, the expected performance of the telescope and observatory, as well as understanding the survey strategy and its interaction with science outcomes.

At this point in commissioning, the operations of the observatory are focused on obtaining specific observations, with very different strategies than will be employed during operations. This includes very different configurations of the Feature Based Scheduler. Thus, we are not testing the Feature Based Scheduler as it would be used in operations yet, and have no comment about issues that may be related specifically to survey strategy implementation.

We can however begin to evaluate how our models may be validated or not by the currently acquired observations. We focus on the observations acquired for the science program, BLOCK-320.

First, clearly bad visits (where stars were clearly trailed in the images, as visible in rubintv) were removed from the set of science visits. Two additional visits had zeropoints which were clearly outliers compared to expected values (more than 1 magnitude away) are were associated with messages in the logs indicating hexapod issues. These visits were also removed. This left 320 ”good” science visits out of 335 between dayObs 2024-11-14 to 2024-11-24.

The throughput curves available in `syseng_throughputs`, the repository that tracks current system engineering summaries of full-focal-plane throughputs, can be used to predict zeropoints for average ITL CCDs. See `https://github.com/lsst-pst/syseng_throughputs/blob/main/notebooks/InterpolateZeropoint.ipynb`, where a simple interpolation function for filter and airmass is defined for the current throughputs (v1.9). The returned zeropoint includes the exposure time, as zeropoints in DM pipelines outputs are for a given exposure with the given exposure time (they are not 1-second zeropoints). A comparison of these predicted zeropoints to the reported median visit zeropoints in the ConsDB (the column `visit1_quicklook.zero_point_medi` is shown in Figure 77. The mean of these zeropoint variations averages 0.13 magnitudes across all bands, being slightly smaller in r (0.09 mag) and slightly larger in y band (0.18); the RMS scatter in these measurements is < 0.02 magnitudes.

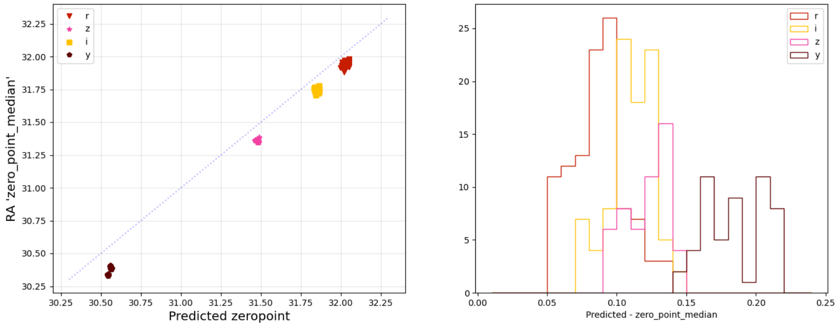

Figure 77: Predicted zeropoints from syseng_throughputs (accounting for airmass) compared to measured zeropoints from `cdb_lsst.comcam.visits1_quicklook`.

Likewise, the survey simulations use a skybackground model as part of the model to determine five sigma visit depths and to choose observation pointings. The outputs available in the ConsDb include a `sky_bg_median` value, which is in counts per pixel. Together with an estimate of the platescale (0.2”/pixel) and a zeropoint, we can convert this into magnitudes per square arcsecond, to compare to the predicted values from the rubin_scheduler skybrightness model. The results are shown in Figure 78. The values are also remarkably consistent, with a scatter of less than 0.15 magnitudes in all bands, and offsets within 0.1 magnitude except in y band, where the measured sky is 0.5 magnitudes brighter than expected. This is within our expected errors in the skybackground model, particularly in y band where the sky is quite variable and harder to model.

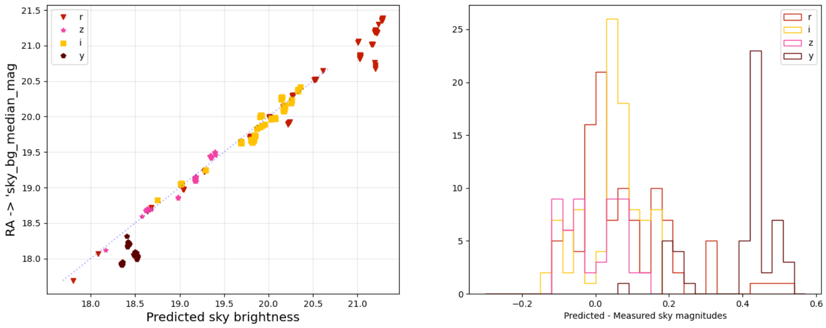

Figure 78: Predicted skybrightness values from `rubin_sim.skybrightness` compared to `sky_bg_median` converted to mags per sq arcsecond from from `visits1_quicklook`.

We look forward to comparing seeing performance to survey predictions. Initial estimates indicate that the mean seeing for these visits was around 1.12 arcseconds, which isn't out of line with longer term survey expectations, especially given that we remain in the early stages of commissioning.

Remaining questions include the efficiency of observations, and in particular the likelihood of whether a single snap will be sufficient.

11.1 Synthetic Source Injection

We used synthetic source injection of stars and galaxies to measure catalog completness and reliability. Figure 80 shows an example figure showing i-band completness and purity as a function of magnitude for ECDFS (tract=5603).

We also confirmed a strategy to use twilight observations to verify the system can accurately observe bright starts (1 mag brighter than 15 saturation lim).

A References

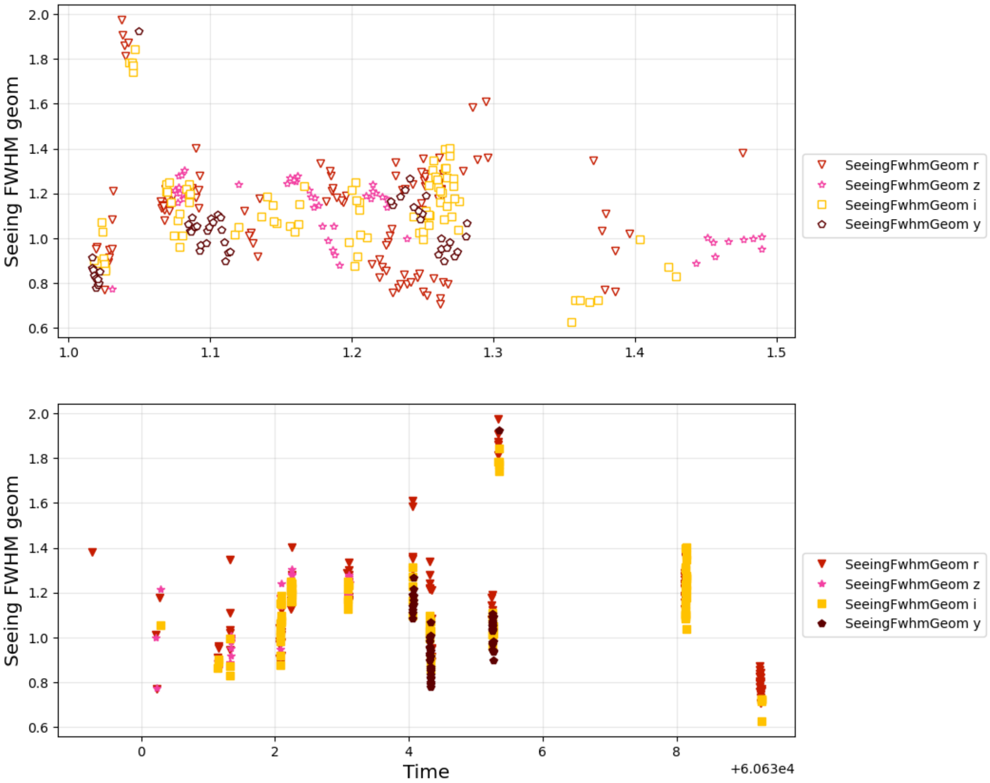

Figure 79: Converting `psf_sigma_median` into the single-gaussian effective seeing PSF values.

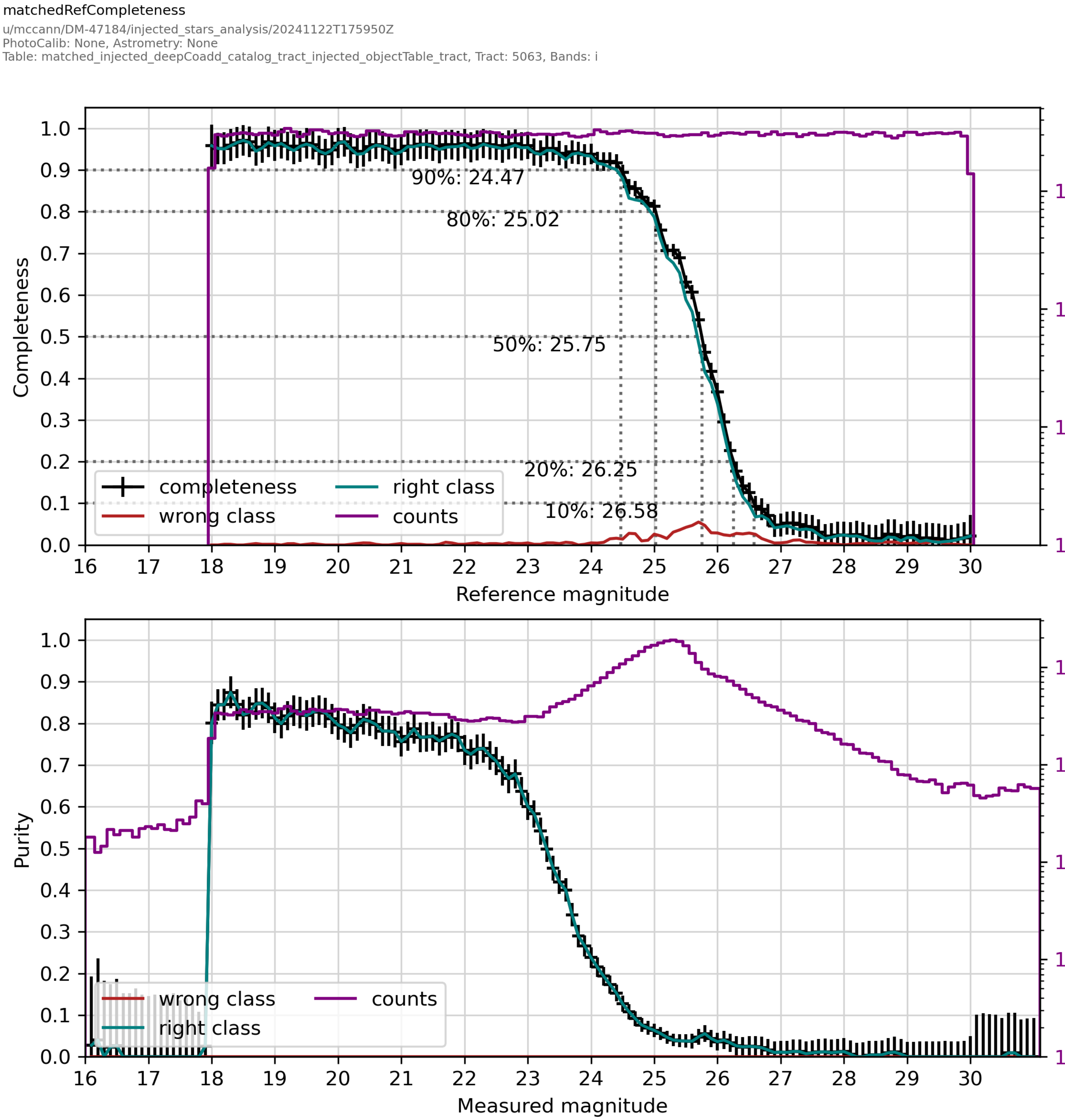

Figure 80: SSI based measurements of completeness and purity in the i-band.

[SITCOMTN-076], Bechtol, K., on behalf of the Rubin Observatory Project Science Team, S.R., 2024, Information Sharing during Commissioning, URL `https://sitcomtn-076.lsst.io/`, Vera C. Rubin Observatory Commissioning Technical Note SITCOMTN-076

[LSE-29], Claver, C.F., The LSST Systems Engineering Integrated Project Team, 2017, LSST System Requirements (LSR), URL `https://ls.st/LSE-29`,
Vera C. Rubin Observatory LSE-29

[LSE-30], Claver, C.F., The LSST Systems Engineering Integrated Project Team, 2018, Observatory System Specifications (OSS), URL `https://ls.st/LSE-30`,
Vera C. Rubin Observatory LSE-30

[RTN-011], Guy, L.P., Bechtol, K., Bellm, E., et al., 2024, Rubin Observatory Plans for an Early Science Program, URL `https://rtn-011.lsst.io/`,
Vera C. Rubin Observatory Technical Note RTN-011

LSST Dark Energy Science Collaboration (LSST DESC), Abolfathi, B., Alonso, D., et al., 2021, ApJS, 253, 31 (`arXiv:2010.05926`), doi:10.3847/1538-4365/abd62c, ADS Link

Melchior, P., Sheldon, E., Drlica-Wagner, A., et al., 2016, Astronomy and Computing, 16, 99 (`arXiv:1511.03391`), doi:10.1016/j.ascom.2016.04.003, ADS Link

B Acronyms

Acronym	Description
2D	Two-dimensional
3D	Three-dimensional
ADU	Analogue-to-Digital Unit
AI	Artificial Intelligence
AOS	Active Optics System
CBP	Collimated Beam Projector
CCD	Charge-Coupled Device
CNN	Convolutional Neural Network
COSMOS	Cosmic Evolution Survey
DC2	Data Challenge 2 (DESC)

DECaLS	The Dark Energy Camera Legacy Survey
DECam	Dark Energy Camera
DES	Dark Energy Survey
DESC	Dark Energy Science Collaboration
DIA	Difference Image Analysis
DIMM	Differential Image Motion Monitor
DM	Data Management
DR10	Data Release 10
DR2	Data Release 2
DRP	Data Release Production
EDFS	Euclid Deep Field South
FGCM	Forward Global Calibration Model
FOV	field of view
FRACAS	Failure Reporting Analysis and Corrective Action System
FWHM	Full Width at Half-Maximum
G6	Group/Gang of 6 SIT-Com leads
GBDES	Gary Bernstein Dark Energy Survey
HIPS	Hierarchical Progressive Survey (IVOA standard)
HSC	Hyper Suprime-Cam
HST	Hubble Space Telescope
ISR	Instrument Signal Removal
ITL	Imaging Technology Laboratory (UA)
JPL	Jet Propulsion Laboratory (DE ephemerides)
LATISS	LSST Atmospheric Transmission Imager and Slitless Spectrograph
LSB	Low Surface Brightness
LSST	Legacy Survey of Space and Time (formerly Large Synoptic Survey Telescope)
LUT	Look-Up Table
M1M3	Primary Mirror Tertiary Mirror
M2	Secondary Mirror
ML	Machine Learning
MODTRAN	MODerate resolution TRANsmission model
NGC	New General Catalogue
PNG	Portable Network Graphics

PSF	Point Spread Function
QA	Quality Assurance
QE	quantum efficiency
RA	Risk Assessment
RMS	Root-Mean-Square
RTN	Rubin Technical Note
SDSS	Sloan Digital Sky Survey
SE	System Engineering
SED	Spectral Energy Distribution
SITCOM	System Integration, Test and Commissioning
SLAC	SLAC National Accelerator Laboratory
SOAR	Southern Astrophysical Research Telescope
SSI	Synthetic Source Injection
SSP	Solar System Processing
TBD	To Be Defined (Determined)
TMA	Telescope Mount Assembly
ZTF	Zwicky Transient Facility